Mechanically-induced Structural Rejuvenation in Zr-Cu-Al-based Amorphous Alloys

Mechanically-induced Structural Rejuvenation in Zr-Cu-Al-based Amorphous Alloys

Jian Qiang

August 2017

Mechanically-induced Structural Rejuvenation in Zr-Cu-Al-based Amorphous Alloys

Jian Qiang
Doctoral Program in Materials Science and Engineering

Submitted to the Graduate School of
Pure and Applied Sciences
in Partial Fulfillment of the Requirements
for the Degree of Doctor of Philosophy in
Engineering

at the
University of Tsukuba

Abstract

Amorphous alloys are non-crystalline materials without any long-range atomic orders. Unlike oxide glasses or polymers, the constituent atoms in amorphous alloys are interacting mainly via the metallic bonds. "Metallic glass" (MG) is a phrase that is almost interchangeable with "amorphous alloy", except that the former specifically refers to the specimen made from melt quenching (MQ). Speaking of which, a high cooling rate in the quenching process is crucial as crystallization should be avoided. Because there are no lattice defects such as dislocations or grain boundaries to mediate plastic strain, most MGs fail catastrophically under uniaxial tension or compression; and the plastic strain is often localized in a major shear band in the width of tens of nanometers. On the other hand, the absence of lattice defects gives rise to a lot of outstanding properties such as a high strength, a large elastic limit, and good resistance to corrosion.

Similar to crystalline alloys whose microstructure and properties can be tailored by appropriate annealing or metal-forming processes, an MG of a specific composition can exist in many structural states depending on its thermal history and/or mechanical treatments. Upon annealing, an MG experiences structural relaxation into a lower energy state with a more ordered structure. When it comes to applications, structural relaxation should be avoided as it leads to embrittlement. Contrarily, tuning the atomic structure to a higher energy state with greater disorder (*i.e*. structural rejuvenation) is of great interest. Structural rejuvenation can be defined as the excitation of atomic configuration towards a higher energy level, and can be quantified by measuring the increase in relaxation enthalpy (ΔH_{rel}). Recently, structural rejuvenation has been studied extensively in the hope of improving plasticity and gaining a better understanding of the structure of MGs at an atomic level. Structural rejuvenation can be achieved by mechanical means such as elastostatic compression, cold-rolling, etc. Compared to these methods, severe plastic deformation techniques can drastically increase the strain level, therefore achieving a much higher level of rejuvenation. For instance, Meng *et al*. demonstrated that deformation of $Zr_{50}Cu_{40}Al_{10}$ MG by high-pressure torsion (HPT) can lead to an increase in ΔH_{rel} as large as 1500 J/mol (Appl. Phys. Lett. 101 (2012) 121914). Despite the intense research effort devoted to studying the structural rejuvenation, some issues remain unsolved.

First, the level of structural rejuvenation not only depends on processing conditions such as the strain level and the temperature of plastic deformation, but is also related to the nature of the processed MG. Greer and Sun (Philos. Mag. 96 (2016) 1644) have proposed that the dynamics of a composition with a higher liquid

fragility are more heterogeneous, and thus could lead to an easier rejuvenation. However, insight on this issue is still lacking, because most studies on rejuvenation primarily focus on exploring new rejuvenation methods, or the microstructural or property changes in one particular composition. With the aim of finding a correlation between the chemical composition and structural rejuvenation, the level of rejuvenation of different HPT-deformed Zr-Cu-Al-based MGs was compared with other compositions reported in the literature.

Second, as mentioned earlier, amorphous alloys are usually fabricated by rapid-quenching of the melt. On the other hand, solid-state amorphization (SSA) offers another way to produce amorphous alloys, for example by severe plastic deformation using HPT. The mechanisms of the amorphous phase formation by MQ and by HPT deformation are quite different since there is no liquid-to-glass transition in the SSA. Thus, different structures and properties can be expected in the amorphous alloys fabricated by different methods. However, most reports about HPT-induced amorphization focused on its dependence on chemical composition; and less attention has been paid to the properties of the HPT-amorphized alloys, especially in comparison to the MG made by MQ. Recently, Yang *et al*. suggested by atomistic simulation that amorphous alloy obtained by SSA is slightly more disordered (*i.e.,* rejuvenated) than the one obtained by MQ (Sci. Rep. 6 (2016) 29722). Specifically, the SSA produces amorphous phase with a lower atomic packing density and a higher energy state than the MQ amorphous phase. However, the confirmation of such rejuvenated amorphous alloy by solid experimental results, and the study of the microstructure-property relationships remain unexplored.

This thesis focuses on i) studying the composition dependence of mechanically-induced structural rejuvenation in MGs and ii) comparing the properties of different amorphous alloys obtained from different fabrication methods all the while providing evidence for concurrent rejuvenation accompanying SSA.

Keywords: amorphous alloy; high-pressure torsion; structural rejuvenation

Contents

Chapter 1 Introduction

1.1 Amorphous alloys

Amorphous alloys are non-crystalline materials without long-range atomic order. Unlike in oxide glasses or polymers, the constituent atoms in amorphous alloys are interacting mainly via the metallic bonds. Conventionally, amorphous alloys can be fabricated by melt-quenching, whereby the microstructure of the metallic liquid can be largely preserved in the solid form. And amorphous alloys obtained from such methods are also called metallic glasses. Fig. 1.1 schematically shows the relation between the enthalpy/volume and the temperature of a glass-forming liquid upon cooling. The characteristic glass transition temperature refers to the inflection point of the cooling curve (the glass transition temperature can also be defined as the temperature at which the viscosity becomes 10^{13}Pa s [1]), which is specific to the composition as well as the thermal history. In general, a higher cooling rate leads to a higher glass transition temperature. Fig. 1.1 also indicates that there should exist a lower limit for the glass transition temperature (Kauzmann temperature), otherwise the enthalpy of the amorphous alloy might fall below the level of its crystalline counterpart [1]. Besides melt-quenching, solid-state amorphization provides a different pathway to the amorphous phase through the accumulation of lattice defects. Possible methods to achieve solid-state amorphization include irradiation [2], mechanical alloying [3, 4], cold rolling [5, 6] and high-pressure torsion [7-9].

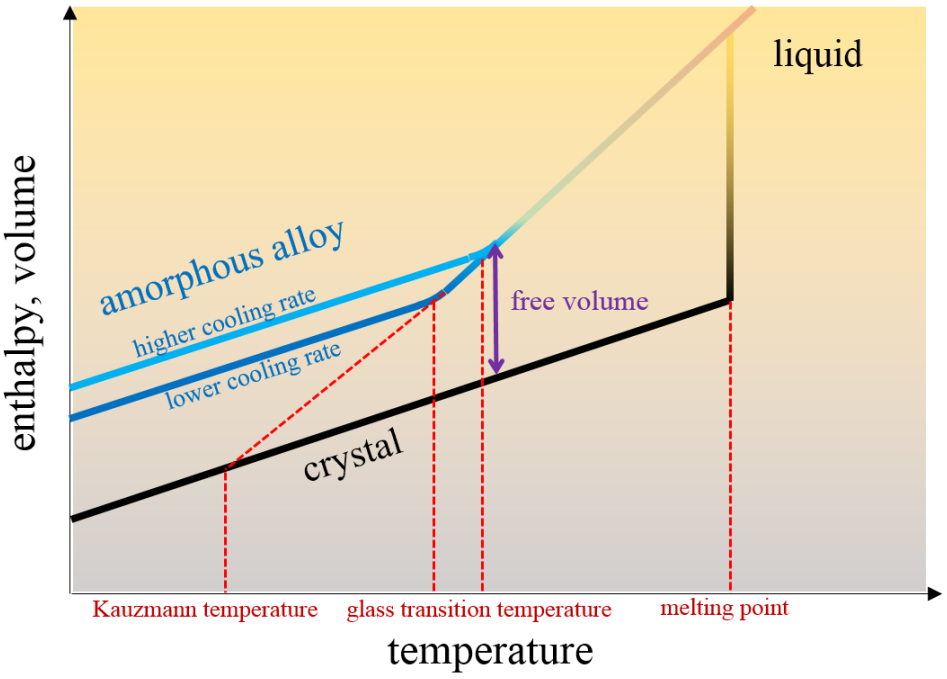

Fig. 1.1. The temperature dependence of the volume or enthalpy of a liquid upon cooling.

Because there are no lattice defects such as dislocation or grain boundary in amorphous alloys, they usually possess many unique properties such as a large elastic limit (~2%), high strength, good resistance to corrosion, thermo-plasticity, and for the Fe(Co)-based amorphous alloys, good soft magnetic properties [10, 11]. However, the lack of lattice defects also implies that there is no effective mechanism to mediate the plastic deformation at room temperature. Alternatively, deformation in amorphous alloys is realized by a process call shear transformation which is a cooperative rearrangement of atom clusters to accommodate the shear strain [12]. And the atoms that undergo such transformation make up a shear transformation zone (STZ), which is schematically shown in Fig. 1.2. It should be noted that STZ is not a natural existence like vacancies in crystalline alloys; STZ is merely a response to the external stimuli with an ill-defined boundary.

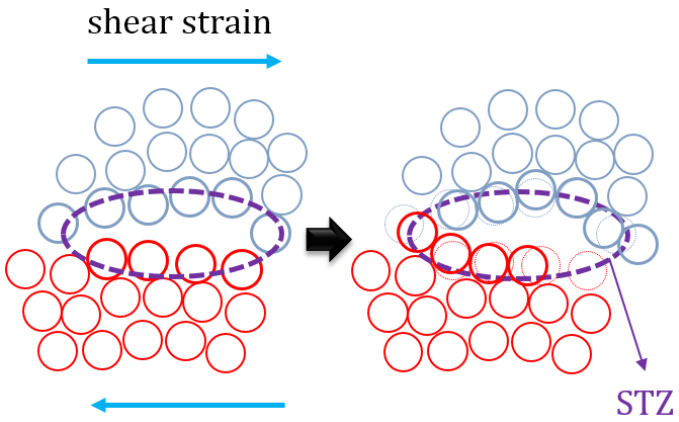

Fig. 1.2. Schematic illustration of a shear transformation zone in amorphous alloys subjected to shear strain.

The activation and propagation of STZs are autocatalytic in the sense that shear transformation is accompanied by the increase in the local level of disordering (such as generation of free volume or liquid-like clusters) [12], thus rendering the sheared regions less shear-resistant. As a result, the subsequent shear strain tends to happen near the already sheared region, *i.e.*, the plastic flow would be highly localized in regions called shear bands. Studies have shown that STZs are more likely to be found in areas with certain atomic-level features [12], which can be interpreted from different perspectives introduced below.

1.1.1 Free volume

First of all, free volume has been a long standing concept that describes the microstructure and level of disordering of an amorphous material. By definition, free volume means the part of the thermal expansion, or excess volume that can be redistributed without energy change [13]. The mobility of the local atoms is dependent on the regional level of free volume in a manner that the diffusivity D scales with $\exp(-\gamma v^*/v_f)$, where

γ is a constant of the order of unity, v^* is the minimum excess volume needed for an atom jump, v_f is the free volume [14]. Thereby, a microstructure-property relationship can be established. The free volume concept was later developed by Spaepen [15]. He suggested that the competition between creation and annihilation of free volume was the dominating factor of the deformation behavior. If the stress is higher than a critical value, free volume annihilation will not keep up with the rate of free volume creation, leading to strain softening and localization. Theoretically, the amount of free volume of an amorphous alloy depends on its thermal history. For example, a faster cooling rate during melt quenching can result in a higher level of free volume (Fig. 1.1). As one of the most adopted concepts describing the microstructure of amorphous alloys, free volume can be easily quantified by measuring the difference in density or volume between the amorphous phase and the corresponding crystalline phase. However, the "free volume" concept itself is flawed in that it is built upon random packed hard sphere model that neglects the flexibility of the metallic bonds. Besides, experimental [16] and simulation [17] results have shown that the amount of free volume is actually not very sensitive to the cooling rate. Specifically, raising the cooling rate by approximately two orders of magnitude (rod sample vs. ribbon sample) would only lead to an increase in the free volume of about 0.1%.

1.1.2 Short-range order and medium-range order

Secondly, the atomic structure of amorphous alloys can be depicted better from the perspective of short-range order. Studied on atomic simulation over the years have concluded that although amorphous alloys are macroscopically uniform, they are not really homogenous. As a matter of fact, atoms in amorphous alloys exist in distinctively different atomic configurations at the length scale of nearest neighbor coordination, *i.e.*, (topological) short-range order (SRO) [18]. Different types of SROs can be well described using the Voronoi index $<n_3, n_4, n_5, n_6>$ with n_i being the number of the i-edged polygons. Fig. 1.3 shows some of the common SROs (purple) and corresponding Voronoi polyhedrons (yellow).

For example, in Zr-Cu binary amorphous alloys, the icosahedral SRO with the Voronoi index being <0, 0, 12, 0> is one of the most numerous. This SRO has a five-fold rotational symmetry and is most shear-resistant. This being said, a higher relative proportion of the icosahedral SRO can lead to a higher shear modulus, which offers a different microstructure-property relationship. The number of icosahedral SRO is also dependent on the thermal history of the amorphous alloy, similar to the free volume. Specifically, a high cooling rate can lead to a decrease of such SRO (Fig. 1.4) [19].

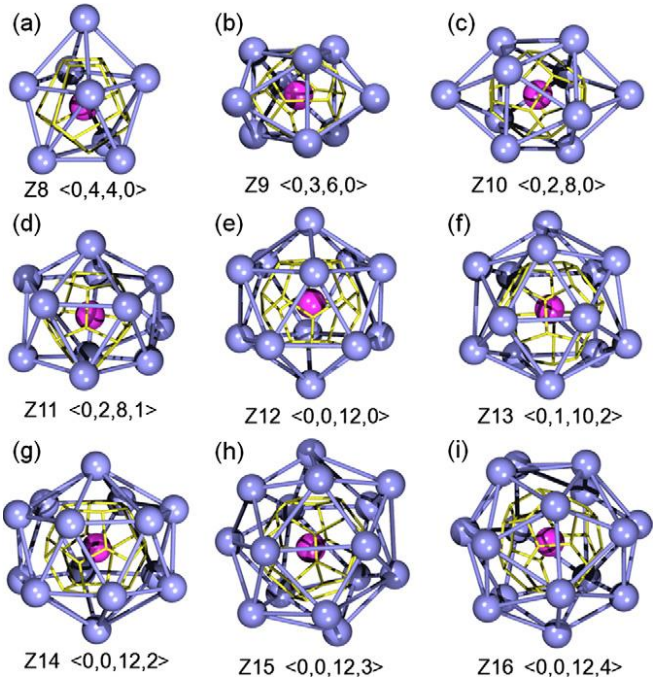

Fig. 1.3. Typical short-range orders (purple) and corresponding Voronoi polyhedrons (yellow) for amorphous alloys. *Z* is the coordination number [14].

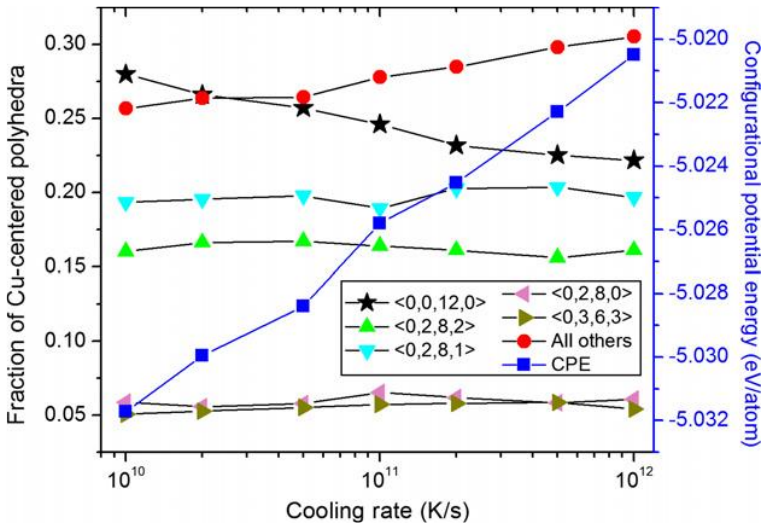

Fig. 1.4. Cooling rate dependence of the fraction of Cu-centered short-range order, and the configurational potential energy (CPE) of the $Cu_{64}Zr_{36}$ amorphous alloy at room temperature [19].

In an actual MG that contains more than one element, there usually exist preferential atomic bonds between the solute and solvent elements (also known as "unlike bonds" in contrast to the solvent-solvent and solute-solute bonds), which generate certain degree of chemical ordering. These unlike bonds are more prevalent for atomic pairs between two elements with a larger difference in electronegativity [20]. Upon shearing, the proportion of the unlike bonds in the shear bands will be reduced [21]. In particular, simulated

results suggest that the Cu-Cu and Zr-Zr interatomic bonds for $Cu_{64}Zr_{36}$ and $Cu_{36}Zr_{64}$ amorphous alloys increased after shear straining at the expense of the Cu-Zr interatomic bonds [21].

Beyond SRO, a relevant concept called medium-range order (MRO) has also been introduced that defines how different SROs are connected, such connection includes (with a descending level of disordering) vertex bonding, vertex sharing, edge sharing and face sharing [22]. A simulation study on binary Zr-Cu amorphous alloys has shown that the level of inter-connectivity is disrupted by shear straining, but the reduction in the size of MROs is more pronounced for the Cu-richer composition [21].

1.1.3 Potential energy landscape

Thirdly, amorphous alloys are thermally metastable with a higher potential energy than their crystalline counterparts, and such energy difference can be used as another structural indicator for amorphous alloys. The potential energy landscape is considered to be capable of providing a relatively simple theoretical framework that can be easily compared with experimental results (*e.g.* using differential scanning calorimetry) [23]. Specifically, the configurational potential energy is the energy level at which the corresponding configuration is frozen [14]. Therefore, the lower the configurational potential energy, the more extensive structural relaxation the metallic liquid has experienced before freezing, and the higher degree of structural ordering is developed in the amorphous alloys (Fig. 1.5). A given potential energy landscape consists of many saddle points (local energy minima), therefore amorphous alloys are not truly homogenous as they are composed of local structures with different energy states. Furthermore, each saddle point is separated from its neighbor by an energy barrier called activation energy, the height of which decides the shear modulus. This being said, a link between the microstructure and property becomes clear. A recent studying shows that the magnitude of energy barriers is also dependent on the cooling rate (similar to the amount of free volume and SROs) such that the higher the cooling rate, the lower the energy barrier for atomic hopping (also known as β-relaxation) [23]. Considering that the activation energy for β-relaxation and for the generation of STZs are closely related [24], the reduced energy barrier could also mean easier generation of STZs.

Although the potential energy landscape provides a rather straightforward description of an MG with a given composition and its structural heritage from the liquid state. The drawing of a specific landscape is oftentimes quite arbitrary without knowing anything about the curvature of each saddle point or the height of the energy barrier.

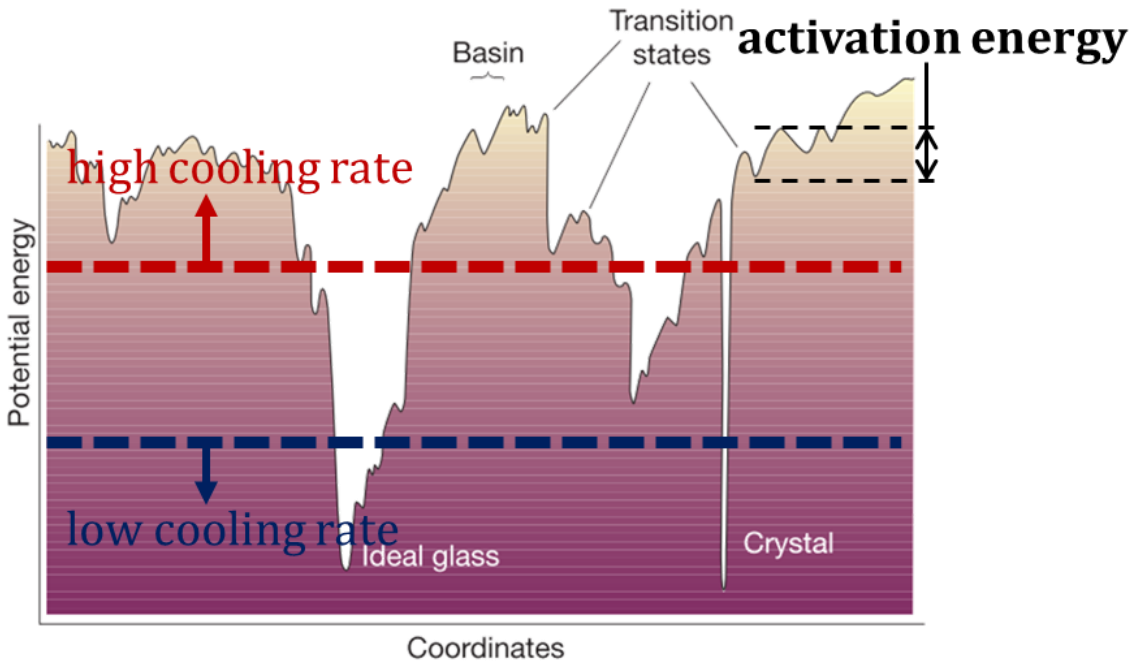

Fig. 1.5. Schematic illustration of an energy landscape. The horizontal axis represents all configurational coordinates [1].

1.1.4 Flexible volume

Very recently, Ding *et al.* proposed a new structural indicator "flexible volume" that incorporates the vibrational degree of freedom [17]. Their proposal was based on the argument that the free volume alone is not sufficient to describe the properties of an MG. The properties are also related to how much free volume is available to accommodate thermal and mechanical changes. Inspired by the Lindemann melting criterion, the flexible volume (v_{flex}) is set to be:

$$v_{flex} = a < \mu_{vib}^2 > \tag{1.1}$$

where a is the interatomic distance, and $<\mu^2_{vib}>$ is the vibration mean square displacement (termed as $<r^2>$ in the original paper). Their simulation also suggested that v_{flex} scales well the shear modulus G such that:

$$G = C\frac{k_B T}{v_{flex}} \tag{1.2}$$

where k_B is the Boltzmann constant, T is the temperature and C is a constant for all MGs (~0.47).

They also claimed that the v_{flex} shows a strong correlation with the commonly-used SRO polyhedrons in the sense that the icosahedral <0, 0, 12, 0> SRO has an obviously larger v_{flex} than the <0, 4, 4, 4> SRO despite the very similar interatomic distances. Moreover, they argued that the activation energy for the atoms with the

highest 10% v_{flex} is 0.9 eV (equates to ~96 kJ/mol if multiplied by the Avogadro constant) higher than those with the lowest 10% v_{flex}.

1.2 Structural relaxation and rejuvenation

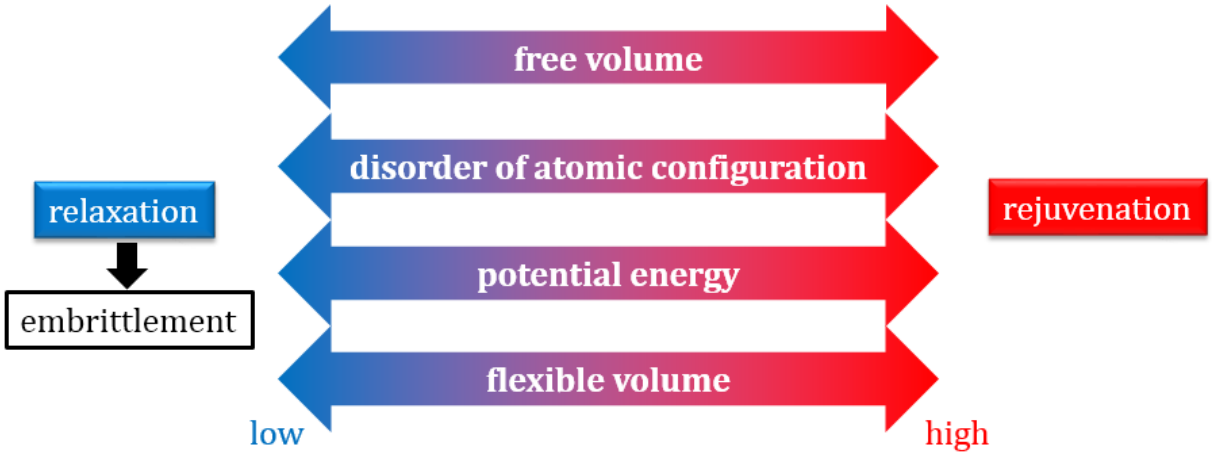

Fig. 1.6. Changes of microstructure in structural relaxation and rejuvenation of amorphous alloys from different perspectives.

When it comes to establishing a microstructure-property correlation, several parallel structural indicators are available. Each of them has their own merits and shortcomings. The free volume can be relatively easily quantified by measuring the difference in density, but it does not provide a clear picture from the atomic level. The concept of SRO may provide the information regarding how atoms are packed at the level of nearest coordination shell, but a direct evidence from experimental observation is still lacking. Although there is no structural indicator that can provide a holistic description of the microstructure, it is certain that an amorphous alloy of a specific composition can exist in many structural states depends on the thermal history and mechanical treatment. As mentioned before, amorphous alloys are thermodynamically metastable. Upon heating to the glass transition temperature (T_g), they are expected to experience structural relaxation where a lower energy state closer to the equilibrium will be attained. Generally, structural relaxation of MGs can be characterized by differential scanning calorimetry (DSC) or dynamic mechanical analysis (DMA). In the sub-T_g region, structural relaxation manifests itself as a broad exothermic DSC pattern, which is considered to comprise at least two distinct relaxation mechanisms [25, 26]. The lower-temperature of this spectra can be attributed to the β-relaxation (Johari-Goldstein relaxation) [27]. Liu *et al.* suggested that the β-relaxation of $Zr_{55}Cu_{30}Al_{10}Ni_5$ can be attributed to the rearrangement of the solvent Zr atoms with large atomic radius [27].

On the other hand, in the sub-T_g region of a typical DMA scan, the β-relaxation appears as an independent peak or a tail of primary α-relaxation (the glass transition). It has also been proposed that a pronounced β-relaxation is likely to be observed in an MG where the atomic pairs have similar negative enthalpies of mixing [28]. When it comes to application, structural relaxation should be avoided as it could lead to further embrittlement with the reduction of the possible activation sites for STZs. Meanwhile, structural relaxation usually results in heat release and densification. Structural relaxation can be interpreted from different viewpoints (Fig. 1.6), which can either mean a reduction of the free volume, an increase of the level of ordering, a decrease of the potential energy or flexible volume. Among these viewpoints, an explanation in the framework of free volume is the most adopted as it facilitates a rather easy description of atomic motion. However, it was built upon hard sphere model. In amorphous alloys, because of the harmonic nature of metallic bonds, atoms can squeeze through tight space without free volume when sufficient shear stress is applied [29]. It was demonstrated that diffusivity in metallic liquids is insensitive to pressure, whereas in the free volume theory diffusivity is expected to be suppressed by pressure. Nevertheless, free volume theory is the most adopted viewpoint as it permits a relatively easily quantification by establishing a linear relationship between the annihilated volume and enthalpy [30]. Structural relaxation has also been interpreted from other perspectives as well. For example, Kohda *et al*. suggested that structural relaxation is accompanied by an increasing level of chemical and topological short-range orders [31]. Moreover, Kahl *et al*. interpreted structural relaxation from the perspective of potential energy landscape where the β-relaxation associated with atomic hopping between each sub-basin was thought to be the underlying mechanism [32].

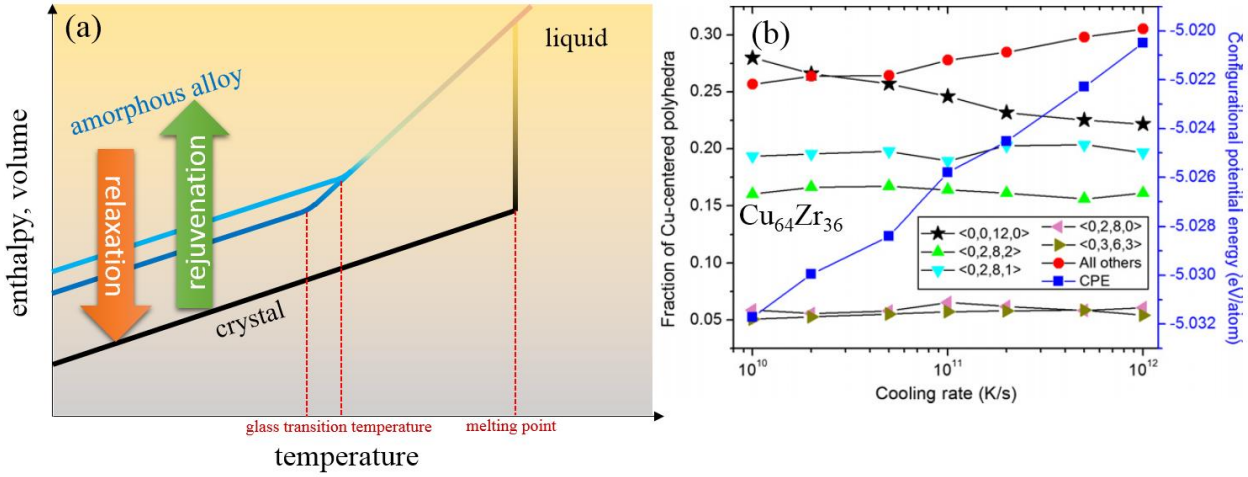

Fig. 1.7. Structural rejuvenation of amorphous alloys interpreted as (a) an increase of the volume or (b) ordered short-range order (specifically in the $Cu_{64}Zr_{36}$ amorphous alloys) [19].

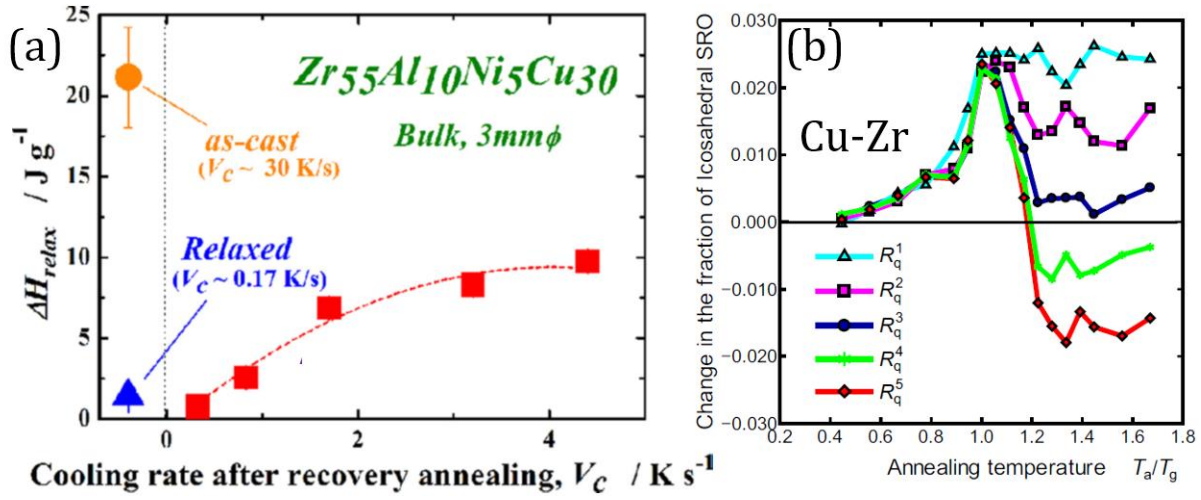

Fig. 1.8. (a) Changes of relaxation enthalpy (ΔH_{relax}) as a function of cooling rate for $Zr_{55}Al_{10}Ni_5Cu_{30}$ MG pre-heated to 735 K (1.07 T_g) [33]. (b) Changes of the number of icosahedral SRO in a Cu-Zr MG as a function of annealing (recovery) temperature at different cooling rates (R_q^i) at (R_q^1 is the slowest and R_q^5 is the fastest.) [34].

A reverse process of structural relaxation is the structural rejuvenation, which corresponds to an increase in free volume (Fig. 1.7(a)), or level of disordering or atomic configuration (Fig. 1.7(b)), or a higher potential energy. In general, structural rejuvenation can be achieved by two types of methods. The first one mainly involves thermal processes. For example, a pre-relaxed $Zr_{55}Cu_{30}Ni_5Al_{10}$ amorphous alloys can be rejuvenated by first heated it to its supercooled liquid region, followed by fast cooling [33]. And the extent of rejuvenation (evaluated by the relaxation enthalpy) is positively related to the cooling rate (Fig. 1.8(a)). It was later found out by atomic simulation that structural rejuvenation in this case can be attributed to the increase of the icosahedral SRO and MRO (how the SROs are connected, Fig. 1.8(b)) [34]. More importantly, it is pointed out that heating the MG to its supercooled liquid region is required for the rejuvenation to happen. And the cooling rate from the supercooled liquid region must be higher than the initial cooling rate by which the metallic liquid was frozen. To certain degrees, rejuvenation by this thermal process resembles that of re-melting the MG and then quench at a higher cooling rate. Thermally induced rejuvenation can also be achieved in the cryogenic region by thermal-cycling the sample between the liquid nitrogen and room temperatures (Fig. 1.9) [35]. However, the mechanism for this phenomenon is still unclear. Ketov *et al*. themselves ascribed this phenomenon to a non-uniform coefficient of thermal expansion [35], whereas Greer and Sun later suggested that rejuvenation in this case was caused by an endothermic process which allows the sample to absorb energy

from the surrounding [36]. It is also interesting to notice that the relaxation enthalpy does not saturate or monotonously increase with increasing number of cycles. After 25 cycles, the relaxation enthalpy returns to the as-cast level.

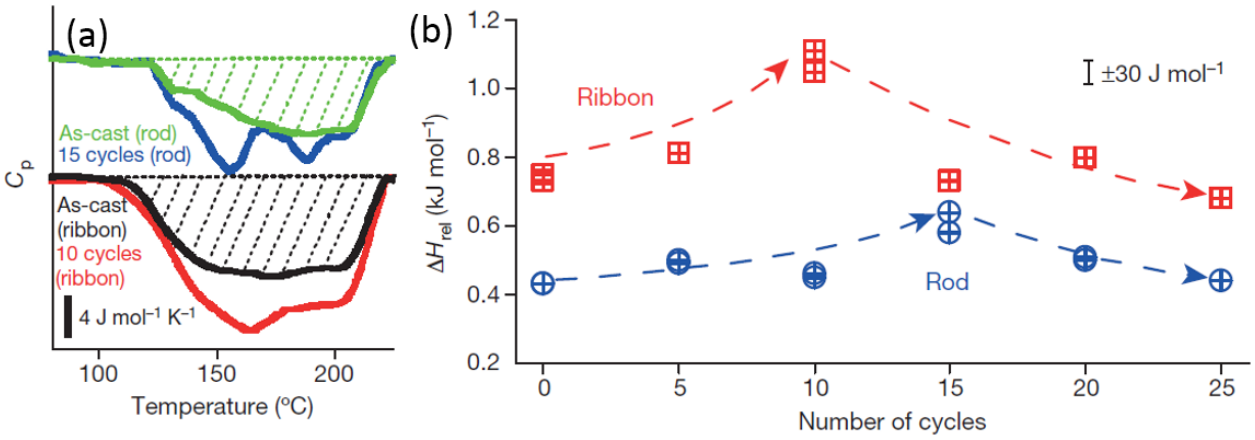

Fig. 1.9. (a) Specific heat curves of $La_{55}Ni_{10}Al_{35}$ MG rod and melt-spun $La_{55}Ni_{20}Al_{25}$ MG ribbon after 15 and 10 thermal cycling between the liquid nitrogen and room temperatures, respectively. (b) Changes of relaxation enthalpy (ΔH_{rel}) of La-based MG ribbon and rod as a function of number of cycles [35].

On the other hand, structural rejuvenation can also be realized by mechanical means. This part will be discussed in detail in chapter 3. Here, the rejuvenation of a $Zr_{50}Cu_{40}Al_{10}$ amorphous alloy by high-pressure torsion (HPT) is introduced as an example [37]. First of all, mechanically-induced rejuvenation is believed to be closely related to the generation of multiple STZs. Therefore, HPT can drastically increase the level of disordering as it can introduce a large amount of shear strain. As a matter of fact, the $Zr_{50}Cu_{40}Al_{10}$ amorphous alloys deformed by 50 rotations of HPT exhibited the largest relaxation enthalpy ever reported. Besides, structural rejuvenation in this amorphous alloy is accompanied by obvious strain-softening and a transition of the deformation mode from localized deformation with pronounced pop-in behavior in the nanoindentation loading curve to a more homogenous one. The restoration of elastic modulus and hardness, and more localized deformation with obvious shear banding by sub-glass-transition annealing also confirmed that the homogeneous plastic flow should be related to structural rejuvenation (Fig. 1.10). It was demonstrated by pair density function that rejuvenation in this case is caused by a net increase of the free volume, which is the result of the simultaneous generation of both shorter and longer interatomic bonds near the first coordination number (Fig. 1.11). Although thermally and mechanically induced rejuvenation are usually interpreted from different perspectives (as will be shown later in chapter 3, the relaxation spectra have different shapes for samples

rejuvenated by different methods), there is no doubt that rejuvenation leads to a higher energy state (Fig. 1.12). Furthermore, from the viewpoint of the potential energy landscape, a natural question arises that whether such energy increase can be realized starting directly from the crystalline state. To rephrase, is the amorphous phase made from crystalline-to-amorphous transition (solid-state amorphization) different from the amorphous phase from the one made by melt quenching? For the purpose of solid-state amorphization, HPT is an effective method. Simply speaking, it is necessary to introduce a large amount of lattice defects such that the Gibbs free energy of the defected crystal surpasses that of the corresponding amorphous phase. This part will be explained in a greater length in chapter 4.

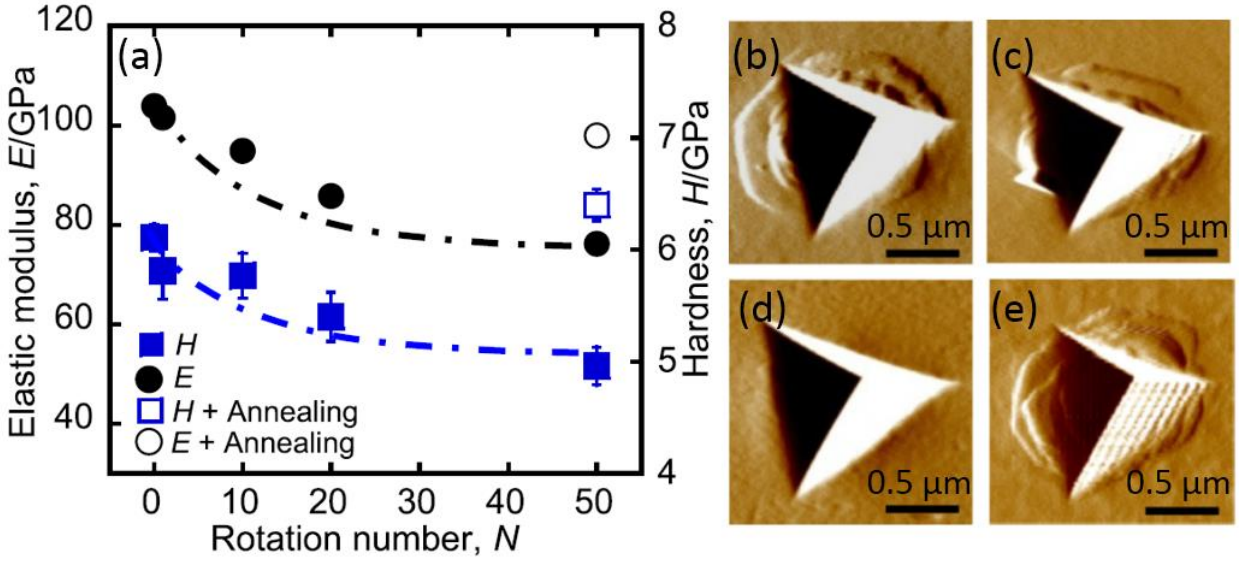

Fig. 1.10. (a) Changes of elastic modulus and nanoindentation hardness of $Zr_{50}Cu_{40}Al_{10}$ MG as a function of different rotation numbers (N) of HPT. The open symbols represent the HPT-deformed N = 50 sample after annealing at 673 K (T_g-70 K) for 1 hour. Scanning probe microscope (SPM) images of indents in the as-cast (b) and HPT deformed state with N = 10 (c) and N = 50 (d). (e) Indent of the HPT-deformed N = 50 sample after annealing at 673 K (T_g-70 K) for 1 hour [37].

It should also be mentioned that HPT is a severe plastic deformation technique where the processed sample is deformed in a quasi-hydrostatic condition. This confined setup is suitable to prevent even brittle materials like amorphous alloys from cracking. A more detailed introduction of HPT is provided in chapter 2.

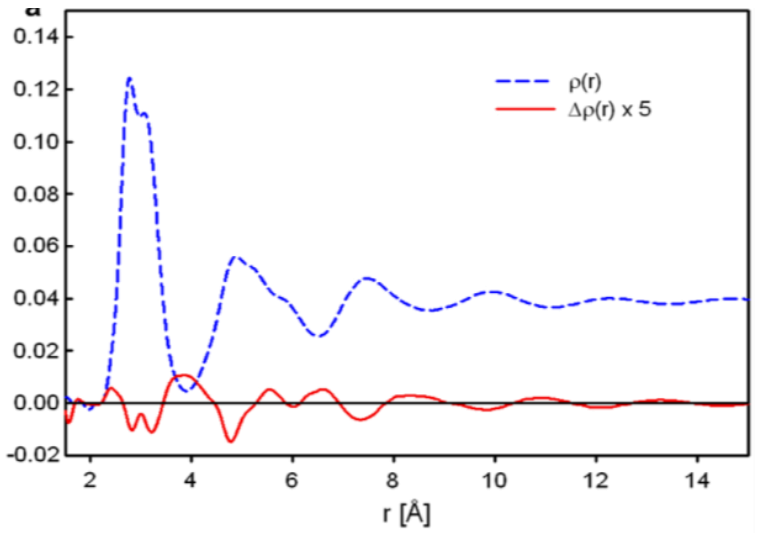

Fig. 1.11. Plot of the reference pair density function (PDF, ρ(r)) together with the PDF difference ($\Delta\rho$(r)) obtained for the $Zr_{50}Cu_{40}Al_{10}$ amorphous alloy deformed by 10 rotations of HPT at a position 3 mm from the center [38].

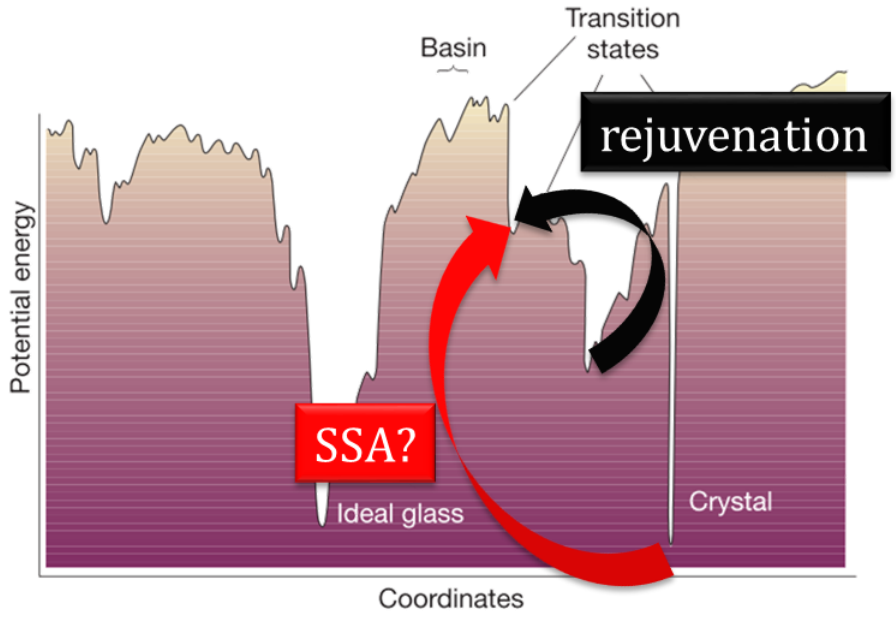

Fig. 1.12. Changes in the potential energy after structural rejuvenation of amorphous alloys and (possibly) solid-state amorphization (SSA) of crystalline alloys.

1.3 Materials in use

The starting materials for HPT are different in each chapter. Chapter 3 focuses on Zr-Cu-Al-based metallic glasses to study the mechanically-induced rejuvenation. In chapter 4, Zr-40at%Cu-10at%Al alloy composed

of multiple intermetallic phases is deformed by HPT to achieve solid-state amorphization.

1.3.1 Metallic glass

Glasses are solid materials whose atomic arrangements lack long-range order, and a metallic glass is such a solid in which the constituent elements are interacting via the metallic bonds. The term "metallic glass" is almost interchangeable with "amorphous alloy", except that the former specifically refers to the specimen made from liquid quenching. The absence of lattice defects gives rise to a lot of outstanding properties that are unique to metallic glasses such as a high strength, a large elastic limit, high magnetic permeability and low coercive force (for FeCo-based alloys). Therefore, metallic glass has been at the center of materials research since its birth in the 1960s [39]. Because of the poor deformability that defies machining, metallic glasses are mostly fabricated by net-shape forming procedures, which is largely dependent on the intrinsic glass forming ability (GFA, a large critical size t_{max} or a low critical cooling rate R_c). Many studies in the late 1990s and early this century have been devoted to discovering compositions with a large glass forming ability [40]. To date, several empirical rules can be referred to when exploring a good glass former. These rules include, a larger supercooled liquid region (ΔT_x), a large T_g/T_m ratio (T_g: glass transition temperature; T_m: melting point) and so forth. Fig. 1.13 summarizes some of the common metallic glass systems listing their R_c and ΔT_x. It can be understood from this figure that the Zr-Cu-Al metallic glasses are good candidates for scientific research because i) they usually possess good GFA which may even be on the order of 1 cm; ii) the usage of noble metals is not necessary to obtain good GFA; iii) the absence of metalloid elements (usually volatile during melting) could guarantee the repeatability of the experimental results and iv) as will be shown later, Zr-Cu metallic glasses are affluent in icosahedral short-range order (SRO) which is the most shear-resistant and ordered, and at the same time most discussed SRO. In this thesis (chapter 3), $Zr_{50}Cu_{40}Al_{10}$, $Zr_{55}Cu_{30}Ni_5Al_{10}$ and $Zr_{65}Cu_{18}Ni_7Al_{10}$ metallic glasses are used to study the effect of mechanically-induced rejuvenation and the consequential property changes. These compositions are chosen for the following reasons: i) good GFAs exceeding 1 cm, which is a prerequisite for HPT using the pre-designed anvils; ii) different Zr/Cu ratios representing different proportions of icosahedral SRO; iii) different room temperature ductility ($Zr_{50}Cu_{40}Al_{10}$ < $Zr_{55}Cu_{30}Ni_5Al_{10}$ < $Zr_{65}Cu_{18}Ni_7Al_{10}$) [41, 42] indicating different shear band stability (note that mechanically-induced rejuvenation is facilitated by the generation of multiple shear bands).

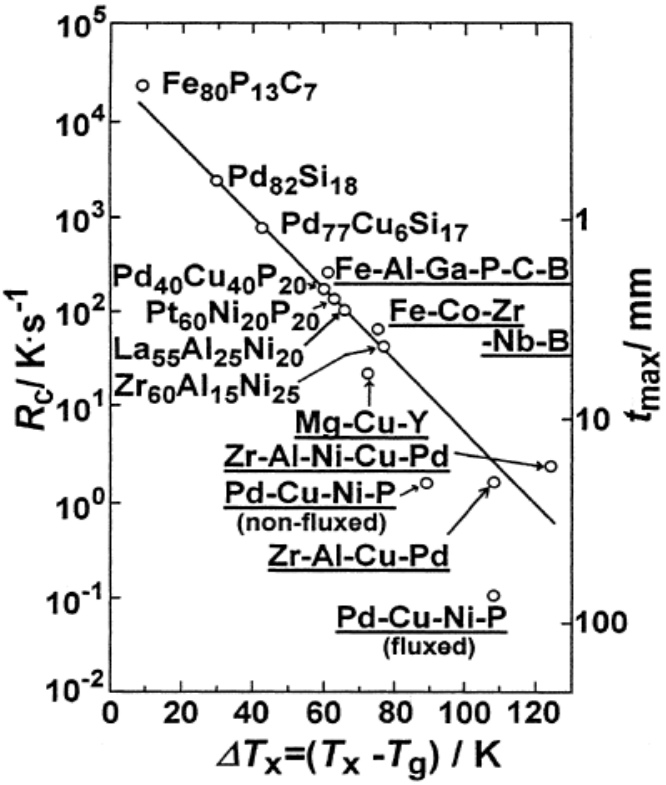

Fig. 1.13. The relationship between critical cooling rate (R_c), critical size (t_{max}) and the supercooled liquid region (ΔT_x) for various bulk amorphous alloys [43].

1.3.2 Intermetallic compound

Compared to solid solutions, intermetallic compounds should be more easily amorphized as a fixed stoichiometry ratio is usually mandatory. And a slight deviation from such ratio would lead to drastic increase in the Gibbs free energy and eventually the collapse of the lattice structure.

To facilitate a comparative study between the amorphous phases made by solid-state amorphization and melt quenching, the starting material was obtained by annealing an as-cast $Zr_{50}Cu_{40}Al_{10}$ alloy in an argon-filled tube at 1073 K for 72 hours. As will be shown in chapter 4, the annealed sample consists of multiple intermetallic compounds: ZrCu (one with a B2 structure and two martensites), Zr_2Cu and τ_5 ($Zr(CuAl)_2$). The affluent grain boundaries acting as sinks of lattice defects can significantly facilitate HPT-induced solid-state amorphization. The equiatomic ZrCu intermetallic compound goes through martensitic transformation (MT) from the cubic B2 structure to two monoclinic martensite phases at 443 K [44], one with a base structure (B19') with $P2_1/m$ symmetry and the other with a superstructure Cm symmetry. Seo and Schryvers suggested a possible crystallographic relationship between the parent B2 phase and the product martensite phases [45]. That is, the basic martensite phase (B19') can be obtained from the cubic B2 by shearing the $(011)_{B2}$ planes in

the $[100]_{B2}$ direction, thus forming the monoclinic angle. The $[011]_{B2}$ $[01\bar{1}]_{B2}$ directions will be elongated and shortened, respectively. Besides these lattice distortions, the atoms are shuffled within each unit cell. In essence, the superstructure consists of four unit of the basic cell and some additional shuffling. The schematic diagram illustrating the crystallography relation between the B2, B19' and Cm is shown in Figure 1.14.

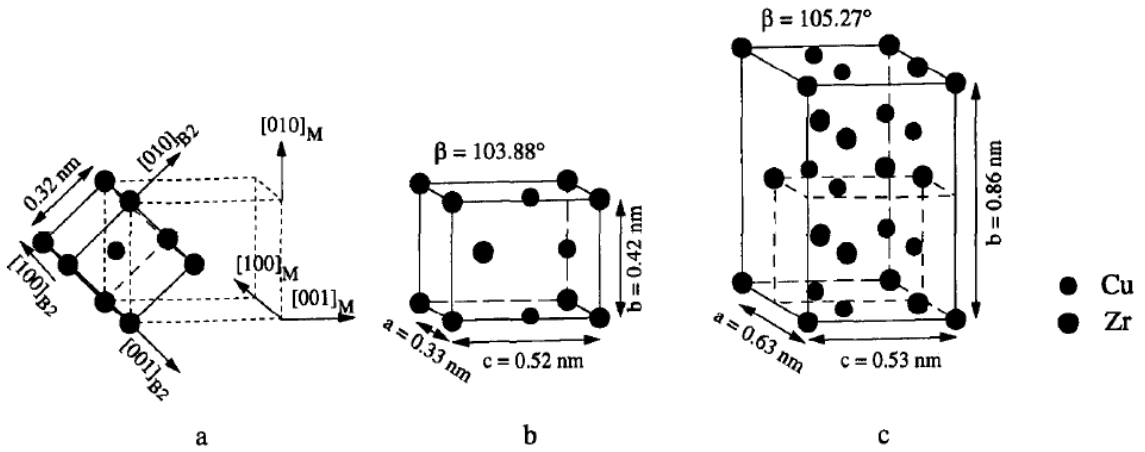

Fig. 1.14. Schematic diagram illustrating the crystallography relation between (a) the austenite B2, (b) B19' and (c) Cm [45].

1.4 Research aim and scope

Previous research has shown that severe plastic deformation induced by HPT can increase the level of disordering in bulk metallic glass samples. This phenomenon is termed "structural rejuvenation" in contrast to "structural relaxation" where a metallic glass enters a lower energy state when heated to a temperature prior to the onset temperature of crystallization [38]. Specifically in $Zr_{50}Cu_{40}Al_{10}$ metallic glass, the structural rejuvenation is accompanied by a reduction in the elastic modulus and hardness and more importantly a transition of the deformation mode from the localized deformation to a more homogeneous deformation without shear banding [37]. However, a systematic study of the influence of rejuvenation on the mechanical and thermal properties still remain unreported. Besides, if structural rejuvenation is a universal phenomenon, what does it depend on? What kind of metallic glass is more susceptible to structural rejuvenation? In chapter 3, these questions will be discussed.

In 2001, Valiev and Mukherjee first reported the formation of an amorphous phase in their attempt to grain-refine a NiTi intermetallic compound using HPT [46]. Since then, more focus has been paid on solid-state amorphization by HPT. In 2009, Sun *et al*. fabricated Cu-Zr metallic glasses using alternatively stacked pure metal sheets. However, the glass transition cannot be observed in thermal analysis [47]. In 2013, Meng *et*

al. fabricated almost fully amorphous samples using tilt-cast ingots of $Zr_{50}Cu_{50-x}Al_x$ (x = 4, 6, 10) alloys. Glass transition was observed in all compositions and the glass transition temperatures agreed with those for rapidly quenched bulk metallic glass samples [7]. Nonetheless, the mechanical and thermal properties of the samples amorphized by HPT are still unknown, especially in comparison to the metallic glass sample made from liquid quenching. Chapter 4 will address these issues.

Before investigating any specific experimental results, chapter 2 will briefly introduce the general experimental procedures. The chapter 5 will summarize and conclude the thesis.

Chapter 2 Experimental procedures

2.1 Experimental process

The master ingots were prepared by casting. Before HPT, the as-cast cylindrical samples were sliced into disks and ground to a thickness of ~0.85 mm. After HPT, the mechanical and thermal properties, as well as the microstructure of the severely deformed samples were examined. The experimental process adopted in this thesis in shown in Fig. 2.1. Note that the diameter of the disk sample and the rotation speed shown in this picture only represent the most commonly-used case.

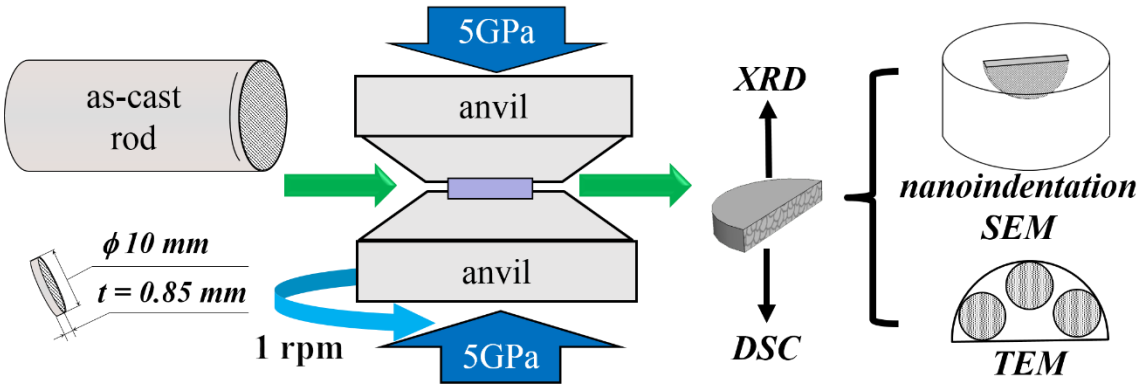

Fig. 2.1. Schematic illustration of the experimental process.

As introduced in the previous chapter, the shear strain of the HPT-deformed sample is larger at the rim of the disk and theoretically zero at the center. Therefore, it is necessary to clarify the position used for property characterization. For the phase identification using XRD, the HPT-deformed samples were ground to the median plane along the thickness direction, and polished by 1000 grid sand paper. For the thermal analysis, a sector of the disk (fan-shaped) was cut from the circular sample using a refine saw. The nanoindentation tests were performed at a position about 4 mm from the center of the disk at the cross section. For transmission microscope observation, the HPT-deformed sample was first ground to its median plane with a thickness of ~100 μm, from which Φ3 mm disks were then punched out. The thin area for the microscope observation was prepared by twin-jet. In order to remove the influence of heating, samples need polishing were mounted in epoxy resin (Struers EpoFix).

2.2 Sample preparation and characterization

2.2.1 Tilt-casting

The metallic glass samples used for HPT were prepared by the tilt-casting method. As shown in Fig. 2.2,

the master alloy was completely re-melted several times to ensure that the elemental distribution is homogeneous in the melt. The metallic melt was then cast into a rod shape mold by tilting the hearth.

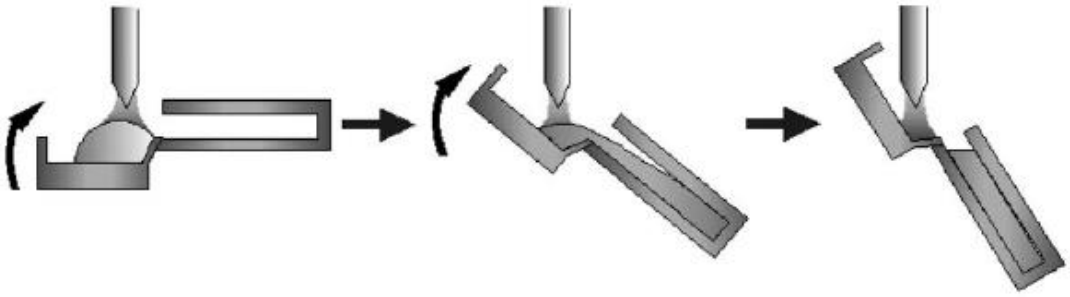

Fig. 2.2. Schematic illustration of the tilt-casting method [48].

2.2.2 High-pressure torsion

The idea of deforming a sample using a combination of high hydrostatic pressure and large shear strain was put forth in 1935 by P. W. Bridgman to study the polymorphic phase transformation [49]. Later on, he found out that the large hydrostatic pressure could drastically increase the ductility of the deformed sample [50]. This finding indicates the feasibility of applying HPT to even brittle samples. In the 1980s, people started to use HPT to fabricate materials with refined structures. The first of such reports is conducted by Valiev, in which he obtained superplastic Al with submicron grains [51]. Since then, most people seemed to use HPT as a tool to study the evolution of microstructure and properties as a function of strain level [52].

2.2.2.1 General principles for high-pressure torsion

Nowadays, the large hydrostatic pressure is usually realized by compressing a sample (typically in the shape of a thin disk) between two anvils (Fig. 2.3). The maximum pressure achievable during HPT depends on what the anvils are made of. For example, it is suggested that 8.5 GPa is the upper limit for anvils made of steel, 30 GPa for WC, 120 GPa for sintered-diamond and 320 GPa for single-crystal diamond [53]. Under the application of the hydrostatic pressure, a controllable shear strain can be exerted to the sample by simply rotating one of the anvils (commonly the bottom one) without incurring fracture. The anvil surfaces in contact with the sample are usually roughened to prevent slippage. If the sample material is free to flow in the radial direction between the two anvils, the setup is considered unconstrained (Fig. 2.3(a)). In order to achieve pressures higher than 2 GPa it is generally preferable to use constrained geometry, in which case a cavity will be machined in one or both the anvils to fit the sample (Fig. 2.3(b) and (c)).

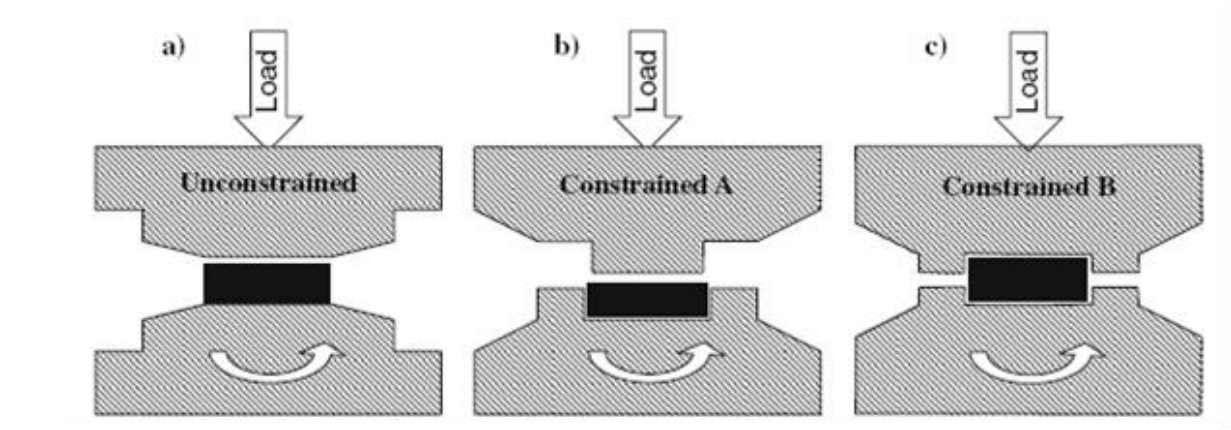

Fig. 2.3. Schematic illustrations of HPT in unconstrained a) and constrained b), c) conditions [54].

2.2.2.2 Shear strain during high-pressure torsion

To start with, the strain (dl) of a disk sample in a radius of R deformed by a small rotation angle dθ is taken from the following equation:

$$\mathrm{d}l = R\mathrm{d}\theta \tag{2.1}$$

And then the incremental strain dγ can be calculated as follow [55]:

$$\mathrm{d}\gamma = \frac{\mathrm{d}l}{h} = \frac{R\mathrm{d}\theta}{h} \tag{2.2}$$

where h is the thickness of the disk sample. If the thickness of the sample is taken to be constant during the deformation, the shear strain, γ, can then be calculated using the following equation in which N stands for the numbers of rotation. A simple illustration for this calculation is presented in Fig. 2.4.

$$\gamma = \frac{\theta R}{h} = \frac{2\pi NR}{h} \tag{2.3}$$

In practice, the equivalent shear strain (ε) is used more often. Generally, the equivalent strain can be evaluated by several methods. The most common one is the von Mises shear strain which can be taken from the following [54]:

$$\varepsilon = \gamma/\sqrt{3} \tag{2.4}$$

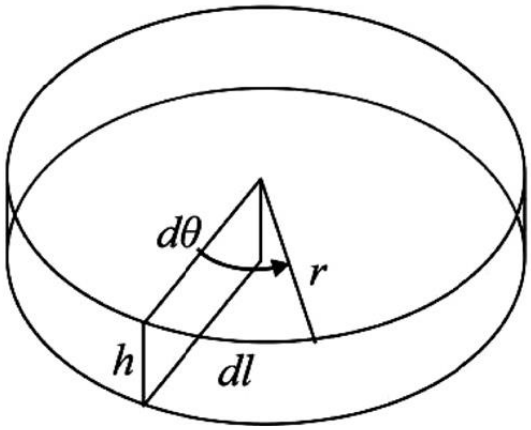

Fig. 2.4. Schematic illustration for the calculation of strain during HPT.

However, the equation 2.4 in not valid for a strain larger than 0.8 [54], in which case the ε should be expressed using another way [52]:

$$\varepsilon = \ln(\gamma) \tag{2.5}$$

It is apparent from equation 2.2 that the edge of a sample would be subjected to a larger strain compared to the part at the center. The shear strain γ calculated using this equation is presented in Fig. 2.5 as a function of rotation number [54].

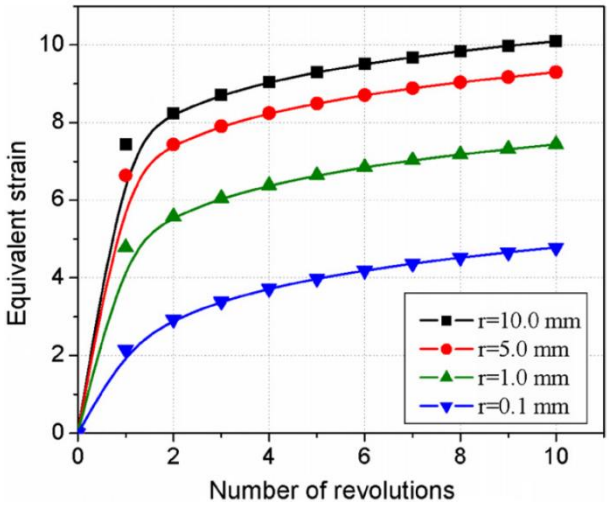

Fig. 2.5. Equivalent shear strain as a function of the number of rotations for positions with different distances from the center of the sample [54].

As a matter of fact, the thickness of the sample will be slightly reduced after HPT. In this case, taking into consideration of the change in thickness (Δh), the ε can be calculated as described in ref. [56]:

$$\varepsilon = \ln[1+(\frac{\theta R}{h})^2]^{1/2} + \ln(\frac{h_0}{h}) \tag{2.6}$$

where h_0 and h are the thickness before and after HPT, respectively. This expression can be further

simplified when $\theta R >> h$, which reveals the following equation:

$$\varepsilon = \ln(\frac{\theta R}{h}) + \ln(\frac{h_0}{h}) = \ln(\frac{\theta R h_0}{h^2}) = \ln(\frac{2\pi N R h_0}{h^2}) \quad (2.7)$$

It is clear from equation 2.3 that theoretically speaking, the strain at the center of the sample is not zero. It is just that this strain from compression is often neglected when the number of rotation is large. As different researchers may choose different calculating methods for the equivalent strain, it would be much straightforward to simply use the number of rotation without specifying the actual strain.

2.2.2.3 Application of high-pressure torsion

As mentioned earlier, Bridgman conducted a series of experiments on metallic and non-metallic elements [49]. He has observed grain refinement and increase in the shear stress in his samples, but his main interest was in the polymorphic phase formation under high pressure [49]. He has observed a number of interesting phase transformations such as the α to ω transformation in zirconium [57] and the amorphous to metallic transformation in selenium [49]. After Bridgman, HPT has been used to study other topics such as changes in crystallographic structure and improvement of mechanical properties [52].

Till now, the interest in HPT deforming on alloys and intermetallic compounds still remains, mainly because the mechanical and functional properties can be largely improved due to grain refinement [52]. For instance, Pushin and his colleagues demonstrated that processing the $Ti_{49.4}Ni_{50.6}$ alloy by 10 turns of HPT rendered the sample partially amorphous with nanocrystalline embedded in the amorphous matrix. This microstructure resulted in a very high strength and good ductility [58]. Korznikov *et al*. also reported that processing TiAl intermetallic compound led to obvious cold-worked structure, and a transition from the ordered $L1_0$ structure to disorder HCP (A3) structure [59]. The disordering of the ordered phase is a well-expected phenomenon for intermetallic compounds subjected to HPT [60].

More recently, HPT has also been applied to more complex systems such as metallic glass and high entropy alloy. HPT on metallic glass was initially conducted on Al-RE-TM system (RE: rare earth, TM: transition metal) which shows primary crystallization behavior upon heating [61, 62]. The end material of this thermal treatment after primary crystallization is a composite in which the α-Al nanocrystals are embedded in the remaining amorphous matrix. It was concluded by these researchers that HPT can aid the nanocrystallization, and therefore is a promising technique to produce metallic glass composites with a good combination of mechanical properties [61, 62]. It should be pointed out that since the Al-RE-TM system does

not have a good glass forming ability, the starting materials in the aforementioned studies were in the shape of ribbons made by melt-spinning. In 2010, using a very good glass former $Zr_{50}Cu_{40}Al_{10}$, Dmowski *et al*. studied the microstructure changes induced by HPT at the atomic level using high energy X-ray diffraction [38]. They found that HPT could relocate the constituent atoms such that the peak intensity increased on both the right and left side of the first coordination peak and the expanse of the first coordination peak itself. This indicated that both longer and shorter range orders were created, which is opposite to structural relaxation when a metallic glass sample is heated. They thereby adopted the expression - "rejuvenation". The phenomenon of structural rejuvenation will be discussed later in depth. On the other hand, HPT on high entropy alloy is a rather new topic. Most studies so far were conducted on Al-Cr-Fe-Co-Ni or Co-Cr-Fe-Ni-Mn systems, which focused on grain refinement and improvement of mechanical properties [63-67]. It seems clear that nano-structured high entropy alloy with improved mechanical properties can be easily obtained, but subsequent annealing following HPT is necessary for obtaining an optimal combination of strength and ductility.

2.2.2.4 Advantages and disadvantages of high-pressure torsion

To begin with, HPT is a relatively simple and quick processing technique. The strain level can be easily evaluated by the above-mentioned equations. Besides, HPT calls for minimal supervision in that a large equivalent strain can be simply achieved by increasing the number of rotations without sample resetting. Second, HPT seems to be more effective in grain-refining compared to other SPD techniques. For example, HPT-deforming a pure Ni to an equivalent strain of ~6 reduced the grain size to ~170 nm, whereas deforming by equal-channel angular pressing (ECAP) to an equivalent strain of ~8 resulted in a larger grain size of ~350 nm [68]. Dutkiewicz *et al*. also observed a similar phenomenon in pure Ti that the grain sized refined by HPT was almost one order of magnitude smaller than that obtained by ECAP [69]. The results of their research are provided in Fig. 2.6. Todaka *et al*. attributed the more pronounced grain-refinement and the consequential larger increase in hardness to the strain gradient during HPT [70].

Compare to ECAP, which is the most developed SDP technique, a major shortcoming of HPT is the lack of capability to produce larger samples. Trials have been made to perform HPT on cylindrical samples as opposed to disk ones. Nonetheless, it often resulted in microstructure inhomogeneity along the vertical direction [60]. Meaningful attempts have also been made applying HPT to large disk samples [60] or ring samples [71]. It has been suggested that HPT-processed samples may have a better prospect of application as

mini-components (such as springs, mini-screws, staples) [60].

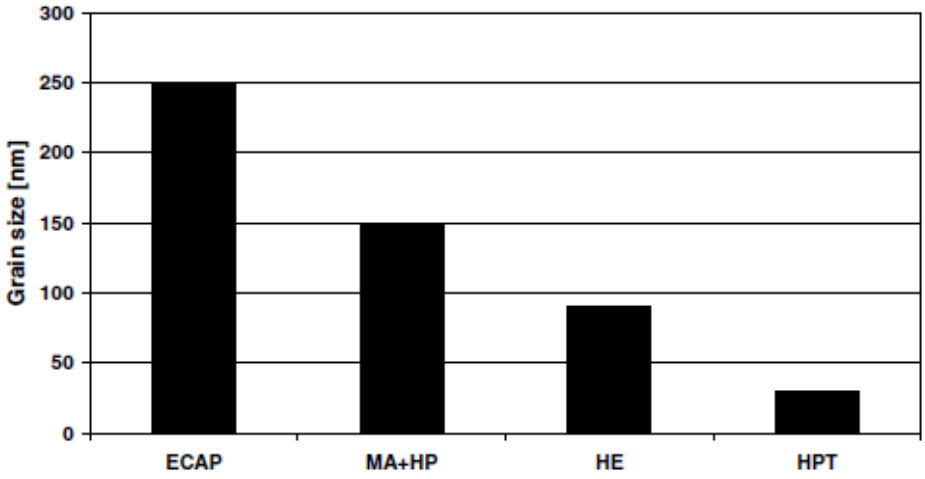

Fig. 2.6. The grain size of pure Ni subjected to different SPD techniques [69]. (ECAP: equal-channel angular pressing; MA: mechanical alloying; HP: hot pressing; HE: hot extrusion; HPT: high-pressure torsion)

2.2.2.5 Processing condition in use

Each anvil used for HPT has a circular sinking of 10 mm in diameter. The circular sinking is concentric with the HPT rotating axis (Fig. 2.7). The sinking has a depth of 0.25 mm, such that the combined depths of the recesses for both top and bottom anvils was 0.5 mm. This value is smaller than the thickness of the disk samples (~0.85 mm), so as to allow a limited outflow of material during processing, preventing the direct contact of the two anvils. Such an event is undesirable both for reasons of premature wear and possible failure of the anvils, and for a considerable reduction in the pressure applied to the sample itself. Moreover, the material outflow creates the backpressure necessary for achieving a pseudo-hydrostatic condition of HPT [72].

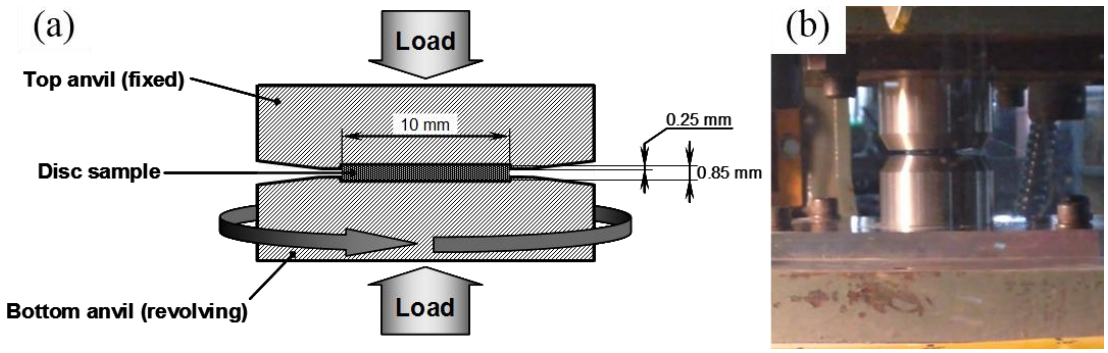

Fig 2.7. Schematic illustration (a) and the actual setup (b) used in HPT experiments.

The deformation took place under a pressure of 5 GPa. In order to improve the contact between the sample and the anvils, the contact area was roughened to create a ragged surface. Prior to each deformation, the sinking

is cleaned with acetone.

2.2.3 X-ray diffraction

The crystalline phases of annealed samples were identified using X-ray diffraction (XRD, Rigaku TTR III) with Cu-K_α radiation (40 kV, 150 mA). Scanning was performed within the range of 20 °- 100 °, in steps of 0.02 °with a speed of 5 °/min. All measurements were performed at room temperature. The analysis of the XRD pattern was conducted using PDXL and Maud software.

2.2.4 Differential scanning calorimetry

The thermal properties were examined using a Perkin-Elmer Diamond differential scanning calorimeter (DSC) in an argon atmosphere. Fig. 2.8 is the schematic illustration of the cell assembly of a DSC. The temperature difference (ΔT) between the sample and reference cells (S and R) is maintained at zero by a feedback mechanism as the temperature is increased or decreased at a constant scanning rate. The differential power that needs to be applied to the sample cell in order to maintain zero temperature difference is recorded continuously as a function of temperature.

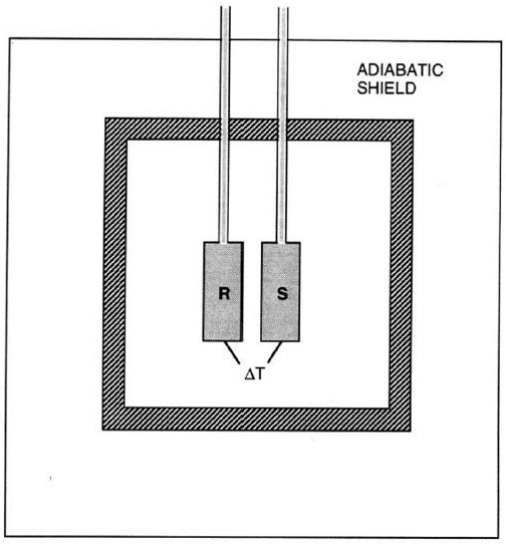

Fig. 2.8. Schematic illustration of the cell of a DSC [73].

2.2.5 Vickers hardness

Vickers microhardness was carried out using a Shimadzu HMV-2 hardness indenter. The indentation period was 15 seconds with a load of 200gf. The tested surface was on the mirror-polished cross-section of the disk. The tests were performed along the radial direction with a 1 mm interval. The detail of the indented position is shown in Fig. 2.9.

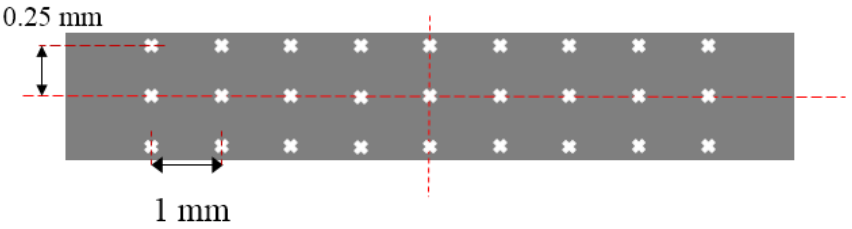

Fig. 2.9. Schematic illustration of microhardness testing on the cross-section.

2.2.6 Microstructure observation

2.2.6.1 Optical microscope

Optical microscopy observations were performed on a Nikon Eclipse LV150 microscope equipped with a high-resolution camera.

2.2.6.2 Scanning electron microscope

An FEI Quanta 250 FEG scanning electron microscope (SEM) was used to examine the microstructure and elemental distribution. The samples used in these observations were mechanically polished to a mirror-like surface.

2.2.6.3 Transmission electron microscope

Transmission electron microscopy (TEM) was performed on a JEOL JEM-2100 or JEM-2100F transmission electron microscope with an accelerating voltage of 200 kV. Energy-dispersive X-ray spectroscopy was performed using a JEOL JEM-2100F to analyze the elemental distribution. The TEM samples were prepared by a Struers Tenupol-3 twin-jet machine with an electrolyte consisting of 20 vol% nitric acid and 80 vol% methanol operated at ~253 K.

2.2.7 Tensile test

Tensile samples with a shape as in Fig. 2.10(a), with a gauge of 3 mm in length, 1 mm in width and ~0.5 mm in thickness were cut from selected samples by electric discharge machining (also known as wire-cutting), such that the center of the gauge was positioned at a radial distance of 2.5 mm. Before the tensile tests, the samples were electro-polished in a mixture of 20 vol% nitric acid and 80 vol% methanol at 253 K to remove the residual stress from wire-cutting (Fig 2.10(b)).

The specimens were strained under tension using a Shimadzu Servopulser EHV-LV020k1-010 servo-hydraulic tester at an initial rate of 1×10^{-3}/s (crosshead speed: 1×10^{-5} m/s) until failure. The elongation was

measured based on the distance between two markers stuck to the crossheads using a high-resolution video camera.

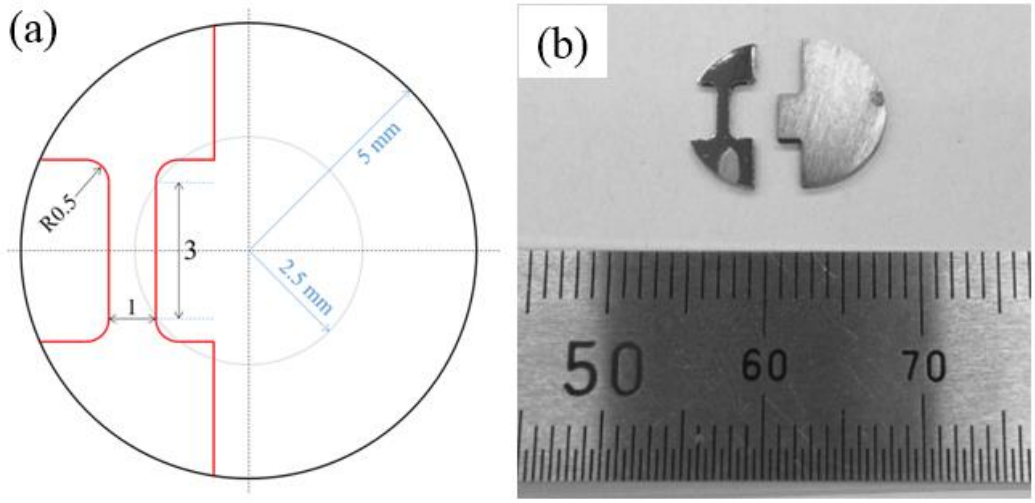

Fig. 2.10. (a) Schematic representation and (b) the actual shape of the tensile test sample (red line) and its original position in the HPT disk (black circle).

2.2.8 Nanoindentation

Nanoindentation was performed on mirror-polished samples on a Hysitron Triboindenter TI950 using a Berkovich indenter. The indentation was conducted in the following sequence: loading to the maximum load of 5000 μN, holding at the maximum load (20 s) and then unloading. Three different loading rates were adopted: 25 μN/s, 250 μN/s and 2500 μN/s. The indentation measurements were carried out on an area 4 mm from the center of the disk on the cross section. A typical load-displacement curve is presented in Fig. 2.11. The hardness (H) and reduced elastic modulus (E_r) were calculated by the Oliver and Pharr method [74].

$$H = \frac{P_{max}}{A_c} \tag{2.8}$$

$$E_r = \frac{\sqrt{\pi}}{2}\frac{S}{\sqrt{A_c}} \tag{2.9}$$

where P_{max} is the maximum load applied during nanoindentation, S is the initial slope of the unloading curve (i.e. stiffness), A_c is the contact area, which can be determined from the calibrated indenter area function.

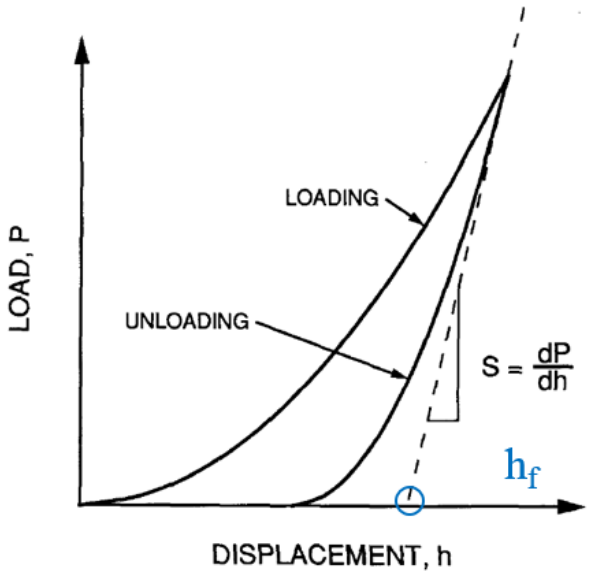

Fig. 2.11 A typical load-displacement curve for nanoindentation test [74].

The E_r is determined by the elastic modulus of the indenter (E_i) and the tested specimen (E) as:

$$\frac{1}{E_r} = \frac{1-\nu^2}{E} + \frac{1-\nu_i^2}{E_i} \tag{2.10}$$

where ν_i and ν represent the Poisson ratio of the indenter and the specimen, respectively. For a diamond indenter, ν_i and E_i are 0.07 and 1140 GPa, respectively. Therefore, using the equation 2.10, the E of the sample can be calculated. The plasticity of the specimen was evaluated using the plastic criterion:

$$R_w = h_{max}/h_f \tag{2.11}$$

where h_{max} is the maximum displacement, h_f is the residual displacement [75]. The morphology of the intent was examined by scanning probe microscopy.

2.2.9 Temperature during deformation

The temperature during HPT was monitored by a K-type thermocouple and a FLIR E40 infrared camera. The temperature measured by the camera is a few degrees higher than the reading from the thermal couple. This is caused by the fact that the thermal couple was embedded in the immovable anvil, not in direct contact with the sample.

Chapter 3 Structural rejuvenation in Zr-Cu-Ni-Al metallic glasses

3.1 Structural rejuvenation in metallic glass

Metallic glasses (MGs) possess many outstanding properties such as great strength, a high elastic limit and good resistance to corrosion that stem from their disordered atomic configuration. However, unlike crystalline alloys whose plastic deformation can be mediated by their intrinsic lattice defects, the mechanism of plastic deformation for MGs remains obscure. At present, "shear transformation" is one of the most accepted concepts explaining the plastic deformation behavior of MGs [12]. Argon proposed that shear transformation refers to a cooperative rearrangement of a cluster of atoms overcoming the saddle point of an energy barrier in the potential energy landscape [76]. This cooperative rearrangement can be regarded as an elemental event of plastic deformation, the accumulation of which eventually leads to the formation of a shear band. A concept that often travels with "shear transformation" is the "shear transformation zone", which refers to the bunch of atoms participating in the shear event [77]. It is noteworthy that a shear transformation zone may not have a well-defined boundary, and it is only a response to the external force instead of a natural existence [12].

Similar to crystalline alloys whose microstructure and properties can be tailored by appropriate annealing or metal-forming processes, an MG of a specific composition can exist in many structural states depending on its thermal history and/or mechanical treatments [78, 79]. Upon annealing, an MG experiences structural relaxation into a lower energy state with a more ordered structure [36]. When it comes to applications, structural relaxation should be avoided as it leads to further embrittlement [36, 80]. On contrary, it is of great interest to tune the atomic structure to a more disordered state with a high energy level. Such excitation of the atomic configuration towards a higher energy level can be called structural rejuvenation, which can be quantified by measuring the rise in relaxation enthalpy (ΔH_{rel}) [35, 36]. Recently, structural rejuvenation has been studied extensively as an attempt to obtain a better understanding of the microstructure of MGs at an atomic level [33-35, 37, 38, 79-87].

As mentioned in the first chapter, structural rejuvenation can be induced by thermal processes: by heating the $Zr_{55}Al_{10}Ni_5Cu_{30}$ MG to a temperature slightly above the glass transition temperature (T_g) followed by a rapid cooling [33] or thermal cycling $La_{55}Ni_{20}Al_{25}$ MG ribbon between room and liquid nitrogen temperatures [35]. Rejuvenation by re-entering the supercooled liquid region is somewhat straightforward as it is later attributed to the changes in icosahedral short-range order and medium range order [34]. In contrast,

rejuvenation by cryogenic cycling is not well understood.

Structural rejuvenation can also be achieved by mechanical means. Cyclic loading within the elastic limit, Louzguine-Luzgin *et al*. found an effect similar to structural rejuvenation at the center of a $Zr_{61}Cu_{27}Fe_2Al_{10}$ MG rod [79]. In addition, plastic straining can also cause rejuvenation as was observed in samples subjected to elastostatic compression [82], cold-rolling [83], laser peening [86] and even nano-scale forces exerted by atomic force microscopy [87]. Compared to these methods, high-pressure torsion (HPT) can drastically increase the strain, therefore drastically increases the level of rejuvenation. Very recently, Meng *et al*. demonstrated that deformation of $Zr_{50}Cu_{40}Al_{10}$ (Zr50) MG by HPT can lead to an increase in ΔH_{rel} as large as 1500 J/mol [37]. Structural rejuvenation induced by plastic deformation can generally be attributed to the topological and chemical disordering introduced by the massive formation of shear transformed zones.

The extent of rejuvenation should not only depend on the processing conditions (extrinsic factors) such as the strain level [37, 83] and the temperature [88], but is also related to the nature (intrinsic factors) of the processed MG. Ediger proposed that the dynamics of local regions of a glass forming liquid could vary by several orders of magnitude, especially for a fragile liquid [89]. This made Greer and Sun assume that a composition with a higher liquid fragility are more prone to rejuvenation [36]. However, insight on this issue is still lacking, because most studies on rejuvenation primarily focus on exploring new rejuvenation methods [35, 79, 86], or the changes in microstructure or property of one particular composition [33, 83, 90, 91]. The mechanically-induced structural rejuvenation is accompanied by multiple shear transformed zones [38].

In this chapter, structural rejuvenation was induced in $Zr_{55}Cu_{30}Ni_5Al_{10}$ (Zr55) and $Zr_{65}Cu_{18}Ni_7Al_{10}$ (Zr65) MGs by HPT. The selection of these compositions was inspired by the fact that Zr65 has a rather good plasticity for MGs and Zr55 also exhibits marginal plasticity [41], whereas the Zr50 MG used for a previous study shows ~0 plasticity. As will be discussed later, different Zr/Cu ratios often indicate different fractions of characteristic SROs, which may facilitate a comparative study. The changes in thermal and mechanical properties resulting from structural rejuvenation were also examined. With the aim of finding a correlation between the chemical composition and structural rejuvenation, the level of rejuvenation of Zr55 and Zr65 MGs was compared with other compositions reported in the literature, regardless of whether they were mechanically and/or thermally processed.

3.2 Changes in thermal and mechanical properties induced by high-pressure torsion

Fig. 3.1(a) and (b) show the XRD patterns of the Zr55 and Zr65 MGs before and after HPT, respectively. For all these samples, only a broad halo peak at $2\theta \approx 38°$ can be observed, typical for amorphous alloys. However, XRD analysis could not detect any obvious change in the peak width or shift of the peak position. The amorphicity of the samples was also confirmed by TEM. Fig. 3.2 shows TEM bright-field images and the corresponding diffraction patterns (inset) of the Zr55 and Zr65 samples deformed by 50 rotations of HPT (referred to as $N = 50$ hereafter). The salt-and-pepper contrast in the bright-field image and the broad halo in the diffraction pattern indicate that both the samples remained amorphous after HPT deformation, without any signs of crystallization.

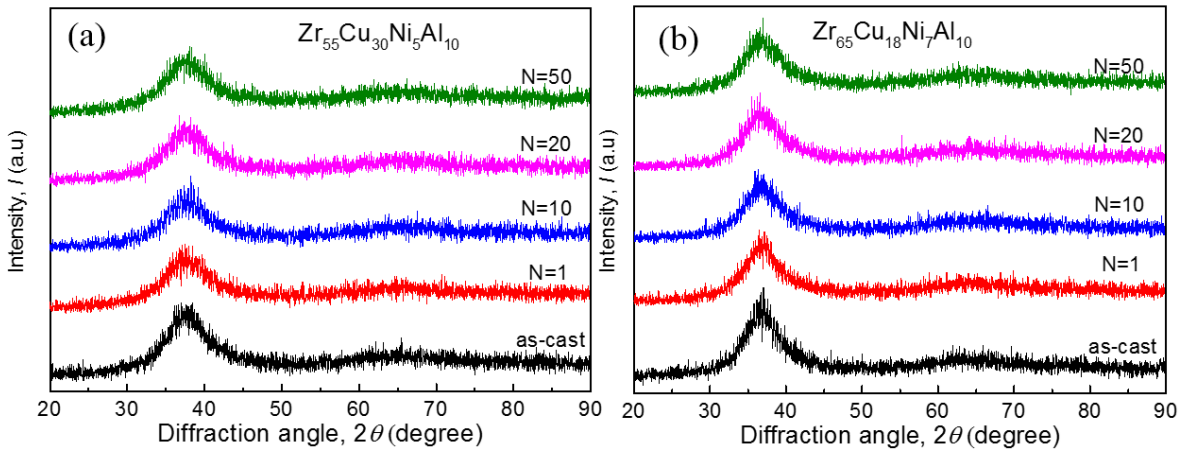

Fig. 3.1. XRD patterns of the (a) Zr55 and (b) Zr65 samples before and after HPT.

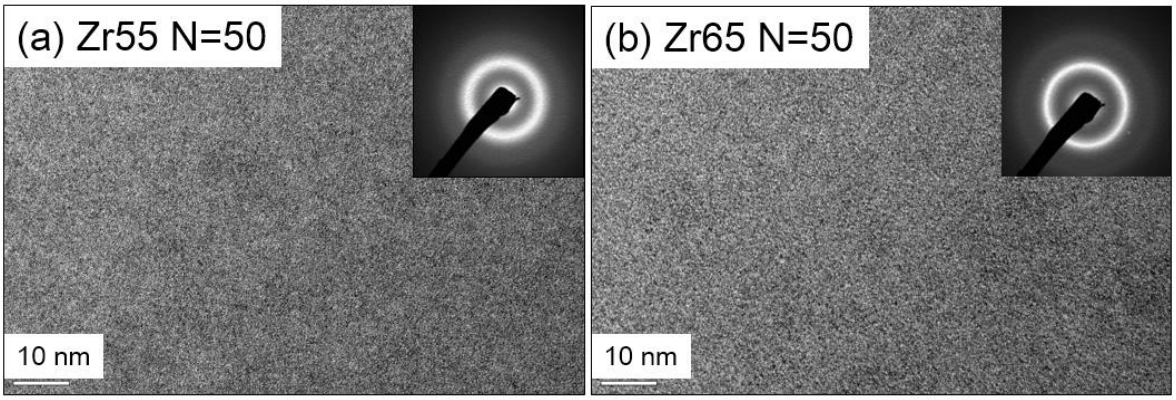

Fig. 3.2. Bright-field TEM images of Zr55 (a) and Zr65 (b) samples deformed by $N = 50$ rotations of HPT. The insets are corresponding selected area diffraction patterns.

3.2.1 Thermal analysis

3.2.1.1 Isochronal and isothermal DSC tests for Zr55

Fig. 3.3 shows the isochronal DSC curves of the Zr55 samples before and after HPT. It can be seen that the crystallization mode remains the same after HPT, there is only one exothermic peak for all the samples. In regards to the characteristic temperatures, the glass transition temperature (T_g) is unchanged (~682 K), however, both the onset (T_x) and peak (T_p) temperatures of crystallization become lower, as is plotted as a function of the number of rotations (N) in Fig. 3.4. This suggests that the thermal stability of the Zr55 MG was slightly deteriorated by HPT.

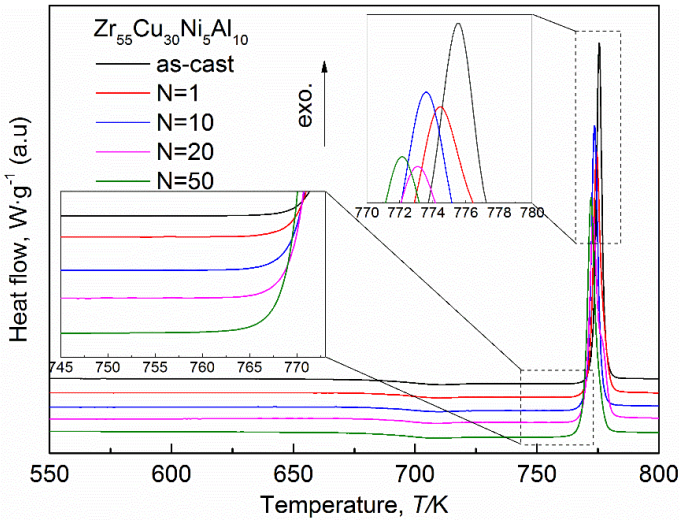

Fig. 3.3. DSC curves of the Zr55 samples before and after HPT. The insets show the detail of the DSC curves in the vicinity of the onset and peak temperature, respectively.

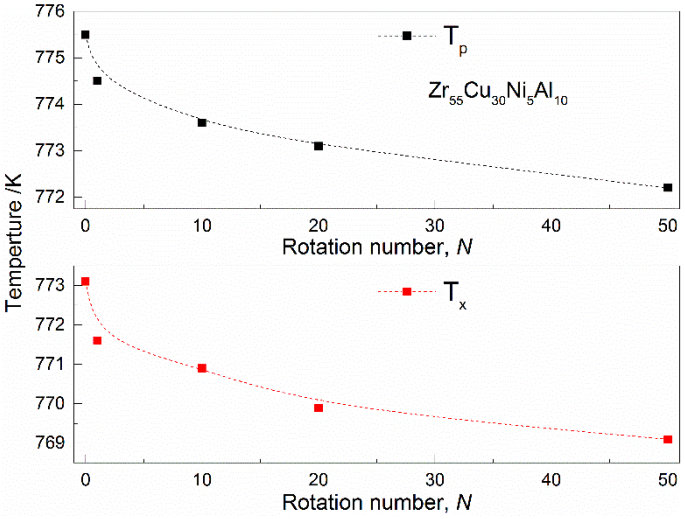

Fig. 3.4. Changes of onset crystallization temperature (T_x) and peak crystallization temperature (T_p) as a function of rotation number (N).

To quantitatively analyze this idea, the activation energy of crystallization was calculated using the logarithmic Kissinger equation [92]:

$$\ln\frac{\Phi}{T^2} = -\frac{E_a}{RT} + \ln\frac{ZR}{E_a} \tag{3.1}$$

where Φ is the heating rate, T is the specific temperature (T_x for the calculation here), R is the gas constant, E_a is the apparent activation energy and Z is the frequency factor evaluating the times of collision of the atoms participating in the crystallization reaction. The fitted lines are shown in Fig. 3.5, together with the DSC curves of the as-cast and N = 50 HPT samples heated at different scanning rates. The slight increase in E_a from 312 ±14 kJ/mol to 323 ±11 kJ/mol after HPT for Zr55 MG lies in the margin of fitting error, suggesting that the energy barrier between each saddle point of the potential energy landscape is almost the same. On the other hand, the value of Z is also very similar for the samples before and after HPT ($R\,E_a\ e^{39.0\pm2.2}$ and $R\,E_a\ e^{40.7\pm1.7}$ min^{-1}), indicating the Kissinger method is not accurate enough to reveal the difference in the thermal stability.

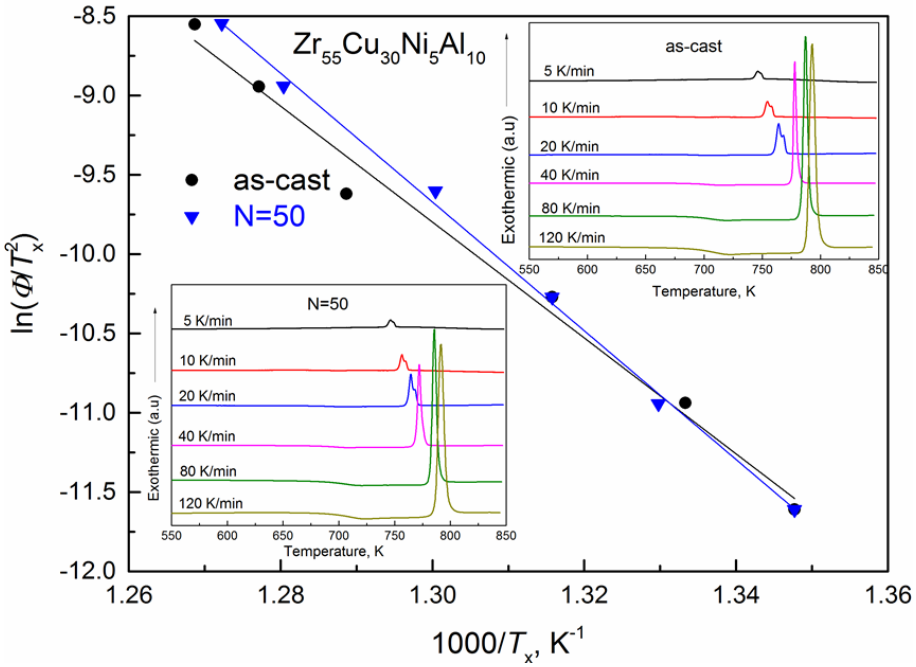

Fig. 3.5. The Kissinger plots of the as-cast and N = 50 HPT Zr55 MG samples. The insets are the DSC curves at different heating rates for these two samples.

Therefore, isothermal DSC tests were conducted on as-cast and N = 50 HPT-deformed Zr55 samples. Fig. 3.6 shows the isothermal DSC curves for the as-cast and N = 50 HPT samples. It is clear for both samples that the duration of crystallization was shorter at a higher temperature. And a higher temperature could lead to a

sharper exothermic peak as well as a shorter incubation time for crystallization.

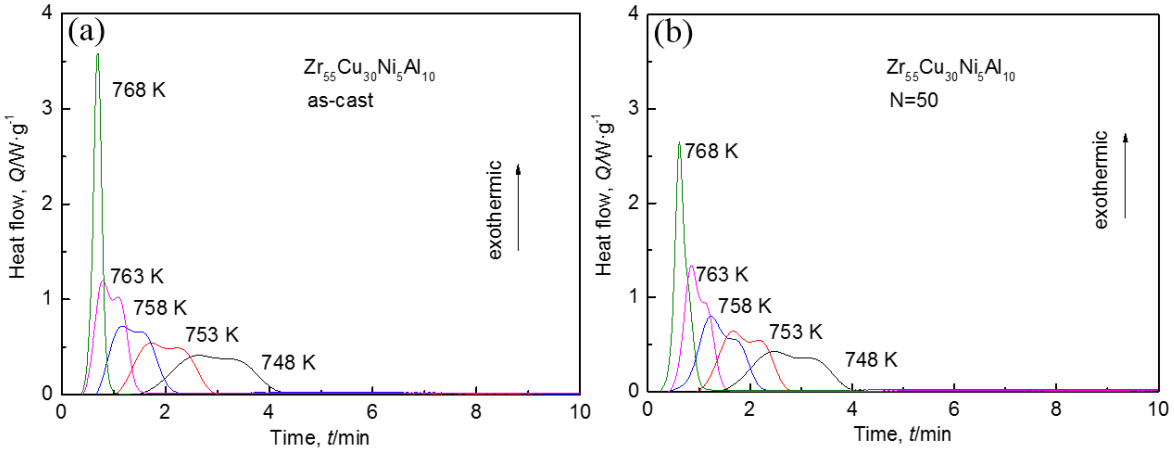

Fig. 3.6. Isothermal DSC curves of the Zr55 sample (a) in the as-cast state and (b) deformed by N = 50 HPT.

The incubation time for crystallization is defined as the time it takes to reach 1% crystallization (the heat release reaches 1% of the total amount). Fig 3.7 shows the relative volume fraction of the crystallized fraction as a function of the annealing time (t). It is apparent that the incubation time decreased with isothermal annealing temperature. Moreover, it can be seen that the N = 50 HPT Zr55 sample exhibited a faster crystallization than the as-cast one. The exact value of the incubation time is also listed in Table 3.1, confirming that the thermal stability decreased after HPT.

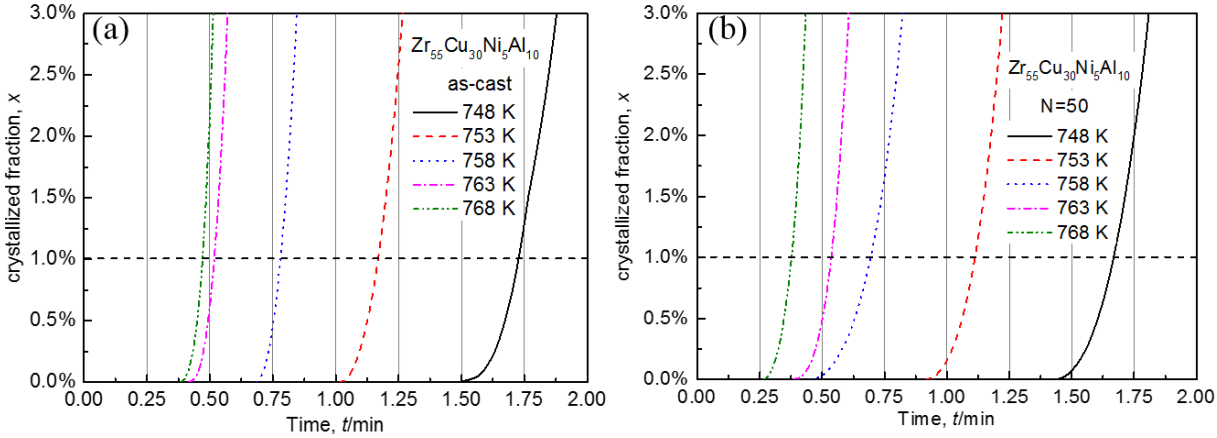

Fig. 3.7. Relative volume fraction of the crystallized phase as a function of the annealing time for the Zr55 samples (a) in the as-cast state and (b) deformed by N = 50 HPT.

Table 3.1 Incubation time for the Zr55 samples in the as-cast state and deformed by N = 50 HPT.

annealing temp. / sample	748 K	753 K	758 K	763 K	768 K
as-cast	1.78	1.17	0.78	0.54	0.47
N=50	1.67	1.11	0.70	0.54	0.36

The crystallization kinetics in isothermal heating is studied using the Kolmogorov-Johnson-Mehl-Avrami equation (KJMA) [93]:

$$\ln(-\ln(1-x)) = n\ln k + n\ln(t-\tau) \tag{3.2}$$

where τ corresponds to a time lag (incubation time), n is the Avrami exponent and k is a kinetic coefficient. The KJMA plot of $\ln[-\ln(1-x)^{-1}]$against $\ln(t-\tau)$ should be a straight line with a slope of n. The fitted curves and Avrami exponents for the Zr55 samples in the as-cast state and deformed by N = 50 HPT are shown in Fig. 3.8. The result shows that the crystallization process can be divided into two stages. From 743 K to 758 K (T_g+100 K), the $n \approx 2$, indicating that the crystallization process is initiated by one-dimensional nucleation and growth [93]. As the temperature increases, the crystallization process will gradually evolve to two-dimensional ($n \approx 3$) and or even three-dimensional ($n \approx 4$) nucleation and growth as reported in ref. [93]. It is worth noticing that HPT did not significantly alter the crystallization process of the Zr55 MG, the different n obtained at different annealing temperatures for the as-cast and N = 50 samples could only be a result of the fitting error.

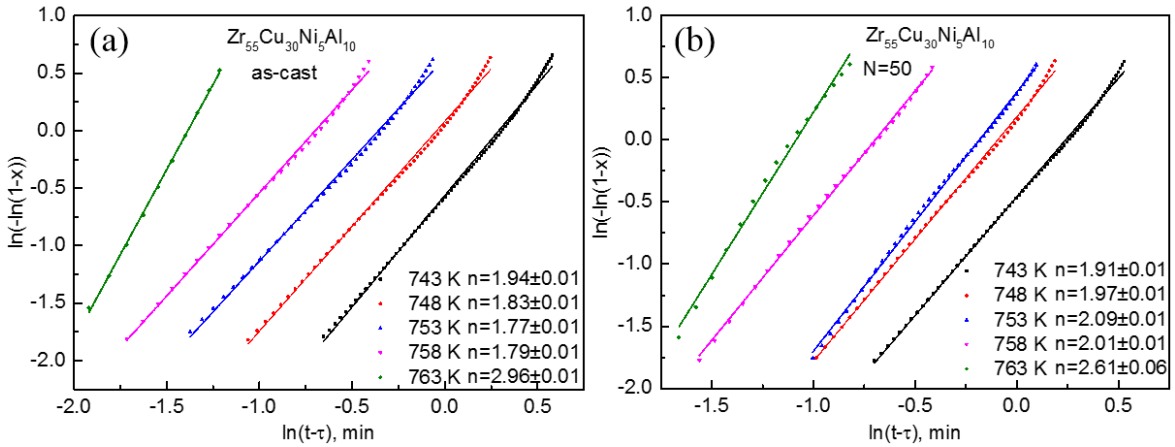

Fig. 3.8. Avrami plots of $\ln[\ln(1-x)^{-1}]$ versus $\ln(t-\tau)$ at different temperatures obtained from isothermal DSC scans.

3.2.1.2 Isochronal and isothermal DSC tests for Zr65

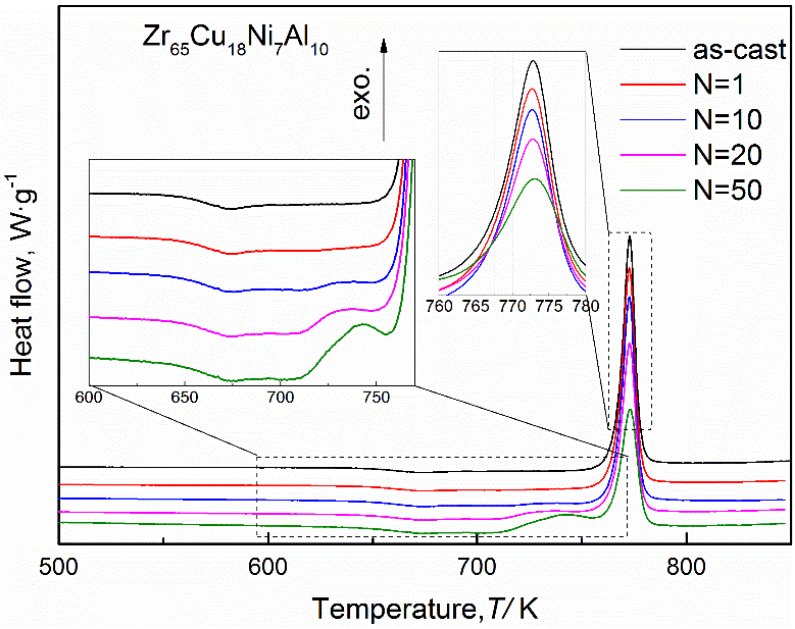

Fig. 3.9. DSC curves of the Zr65 samples before and after HPT. The insets show the detail of the DSC curves in the vicinity of the onset and peak temperature, respectively.

Compared to Zr55, the changes of the characteristic temperatures and crystallization mode of the Zr65 MG after HPT were more obvious. Fig. 3.9 shows the isochronal DSC curves of the Zr65 samples before and after HPT. The T_g remained unchanged (~651 K), similar to the Zr55 MG. However, the crystallization mode changed gradually from a single-peak to two-peak reaction with increasing N, and the T_x was significantly lowered. The worsening of the thermal stability signified by the narrowing of the supercooled liquid region ($\Delta T_x = T_x - T_g$) can be quantitatively analyzed using equation 3.1. Fig. 3.10 presents the Kissinger plots of the as-cast and N = 50 HPT Zr65 MG samples. The E_a decreased from 205 ±7 kJ/mol to 150 ±17 kJ/mol after HPT, suggesting the energy barrier between each saddle point of the potential energy landscape was considerably lowered.

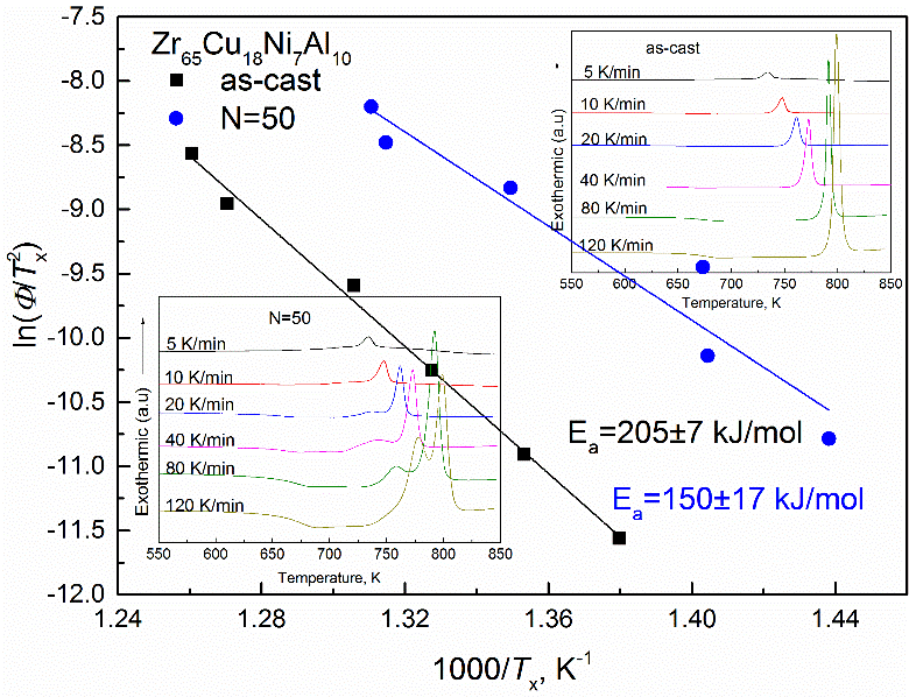

Fig. 3.10. The Kissinger plots of the as-cast and N = 50 HPT Zr65 MG samples. The insets are the DSC curves at different heating rates for these two samples.

The small exothermic peak at the lower temperature side of the main peak not only deteriorated the thermal stability of the supercooled liquid, but also changed the crystallization mode. In this context, the crystallization products were analyzed. In the case of Zr65, HPT caused significant changes in the crystallization behavior. For the HPT-deformed sample (N = 50), heating to 754 K (between the 1st and the 2nd onset crystallization temperature, T_{x1} and T_{x2}) led to the precipitation of Zr_2Cu, Zr_6NiAl_2 and some unknown phases. Further heating to 847 K (~50 K over T_{x2}) led to the precipitation of Zr_2Ni. The same precipitates could be identified in the as-cast Zr65 sample after heating to 847 K (~50 K over T_{x2}). However, the intensity of the peaks corresponding to Zr_2Ni was stronger. The precipitation of Zr_2Ni was clearly suppressed after HPT. The changes in the crystallization mode could be related to the hypoeutectic nature of Zr65 MG. Specifically, the excessive Zr atoms would increase the number of Zr-Ni atomic bonds due to the large enthalpy of mixing [94], these bonds may be damaged preferentially because of the relatively small interatomic distance [95], repressing the crystallization of Zr_2Ni. Mitrofanov *et al*. have observed a similar phenomenon in $Pd_{38}Ni_{40}P_{22}$ (ΔT_x = 58 K) and $Pd_{40}Ni_{40}P_{20}$ (ΔT_x = 66 K) MGs, in which the latter sample exhibited a larger decrease in the width of the supercooled liquid region after cold-rolling [96]. They interpreted this phenomenon from the viewpoint of "potential energy landscape" (as opposed to "atomic pairs"),

suggesting that plastic strain could generate new local configurations with low kinetic stability against crystallization (somewhat analogous to "fragmented clusters"). It was concluded that there are more such newly generated "less-stable" local configurations for an MG with a wider supercooled liquid region. Their argument can be well applied to the Zr55 (ΔT_x = 92 K) and Zr65 (ΔT_x = 115 K) MGs. This also brings to mind that interesting parallels exist between different structural indicators.

The crystallization products of the Zr55 MG was also examined as a comparison. The as-cast and HPT-deformed (N = 50) Zr55 samples were heated up to 798 K, about 50 K higher than T_x, in the DSC furnace. In the case of both the as-cast and HPT annealed samples, the crystallization products were Zr_2Ni, Zr_2Al, Zr_2Cu and some unknown phases. The XRD patterns of the crystallization products for Zr55 and Zr65 MGs are shown in Fig. 3.11.

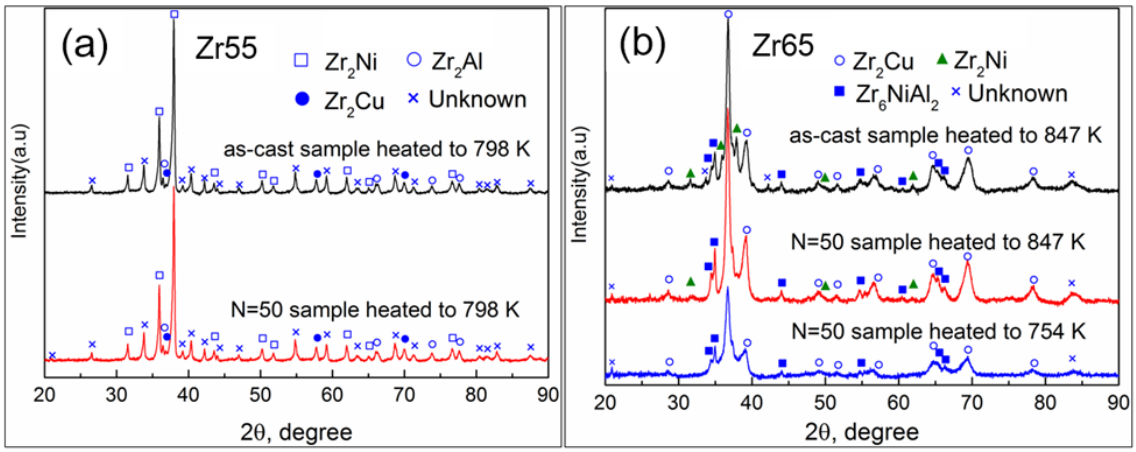

Fig. 3.11. XRD profiles of (a) annealed Zr55 and (b) annealed Zr65 samples.

3.2.1.3 Relaxation enthalpy

When it comes to structural rejuvenation, the most important thermal parameter is the relaxation enthalpy (ΔH_{rel}). One explanation is that ΔH_{rel} is proportional to the amount of free volume such that [30]:

$$\Delta H_{rel} = \beta \Delta v_f \tag{3.3}$$

where β is a constant and Δv_f is the change of free volume per atomic volume.

Representative DSC curves for the Zr55 and Zr65 samples in the as-cast state and deformed to N = 50 are presented in Fig. 3.12. The ΔH_{rel} was calculated from the area encircled by the 1st and the 2nd heating curves of DSC analysis:

$$\Delta H_{\mathrm{rel}} = \int_{T_1}^{T_2} \frac{W_1(T) - W_2(T)}{c} dT \tag{3.4}$$

where T_1 and T_2 are the start and finish temperatures of relaxation, respectively. W_1 and W_2 are the heat flow of the 1st and 2nd run, respectively, and c is the heating rate.

The ΔH_{rel} in both the Zr55 and Zr65 alloys increased with N (Fig. 3.13), similar to $Zr_{50}Cu_{40}Al_{10}$ (Zr50) alloy in ref. [37]. In the case of Zr55 (Fig. 3.12(a) and (b)), the ΔH_{rel} was 85 J/mol in the as-cast state, which increased to 761 J/mol after 50 rotations, indicating significant structural rejuvenation induced by HPT. Besides the increase in ΔH_{rel}, there was also a decrease in the onset temperature of structural relaxation (T_{onset}, marked by an arrow in Fig. 3.12). This suggests that the disordered structures induced by HPT are thermally unstable. The composition dependence of mechanically-induced structural rejuvenation will be discussed at the end of this section.

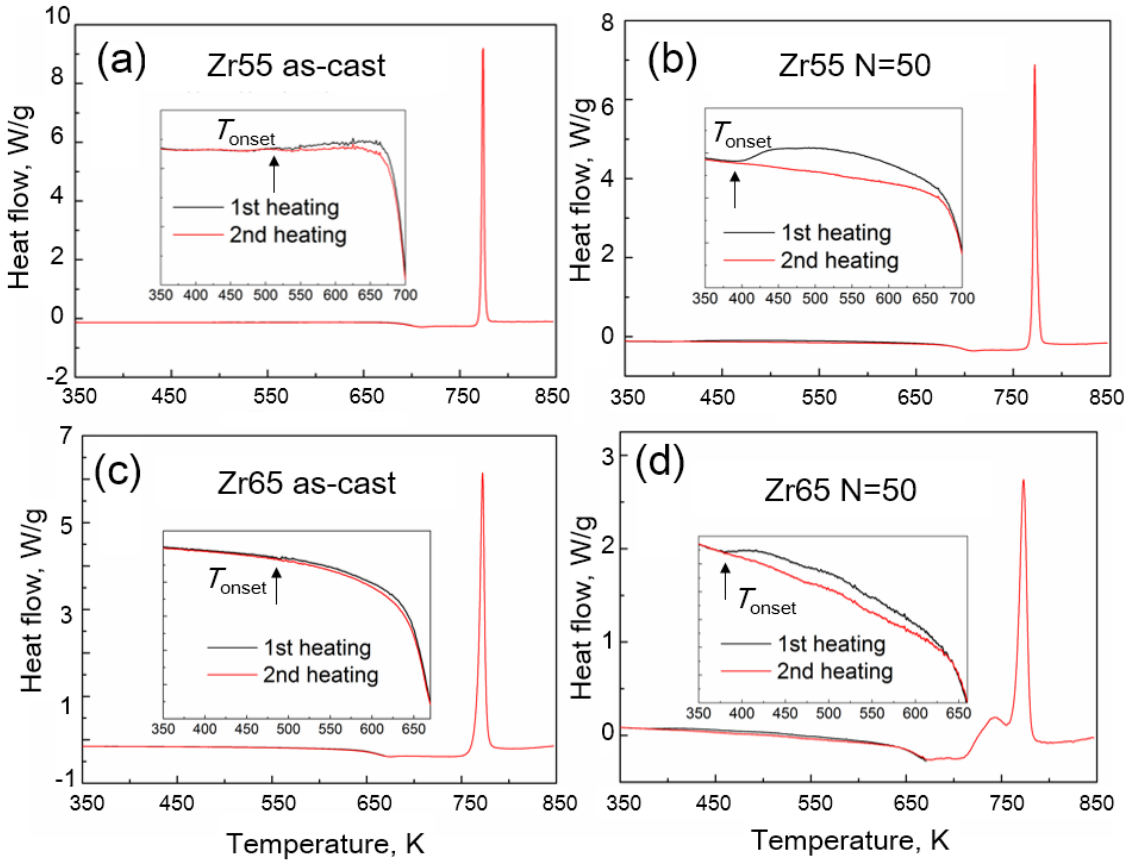

Fig. 3.12. DSC profiles of Zr55 MG in the as-cast state (a) and after 50 rotations of HPT (b), and Zr65 MG in the as-cast state (c) and after 50 rotations of HPT (d). T_{onset} denotes the starting temperature of structural relaxation.

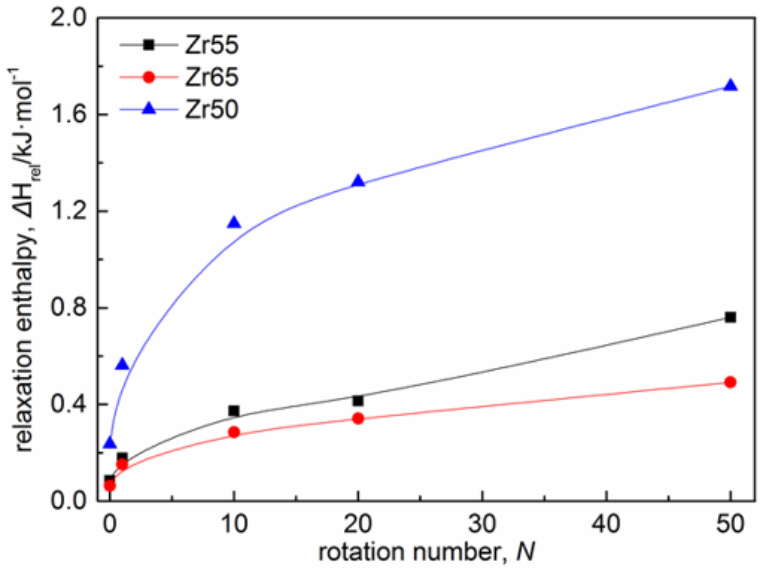

Fig. 3.13. Calculated structural relaxation enthalpy as a function of the number of rotations.

3.2.2 Mechanical properties

3.2.2.1 Vickers hardness

Besides the changes in thermal properties as seen above, the structural rejuvenation induced by HPT also resulted in changes in the mechanical properties. Vickers micro-hardness of the Zr55 and Zr65 MGs before and after HPT are plotted in Figure 3.14 as a function of the distance from the disk center. It is obvious that HPT induced obvious strain-softening in these two MGs, and the hardness seemed to be lower at the rim than at the center. From the optical images (Fig. 3.15) one can see that there is shear banding around the indents only for the as-cast samples.

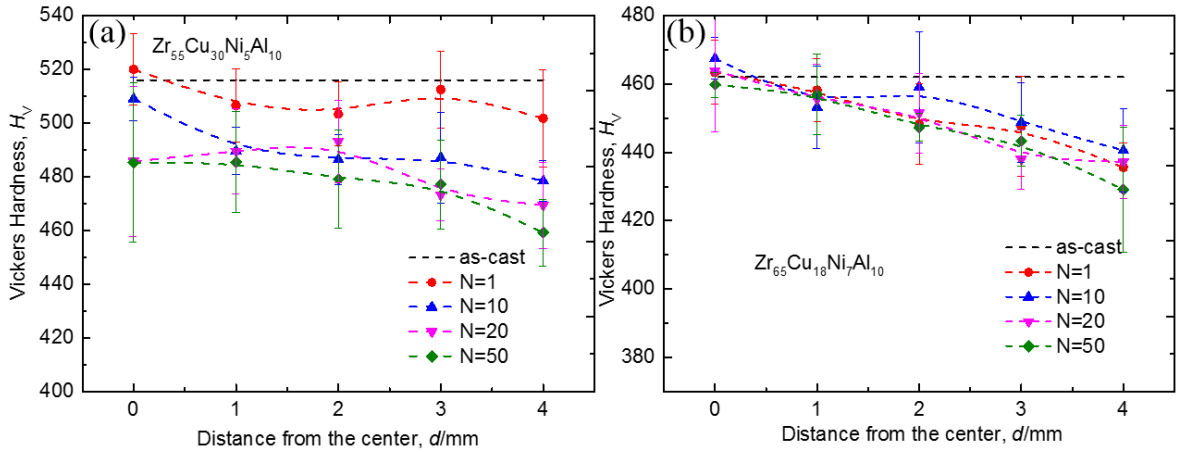

Fig. 3.14. Vickers micro-hardness of the Zr55 and Zr65 MGs before and after HPT.

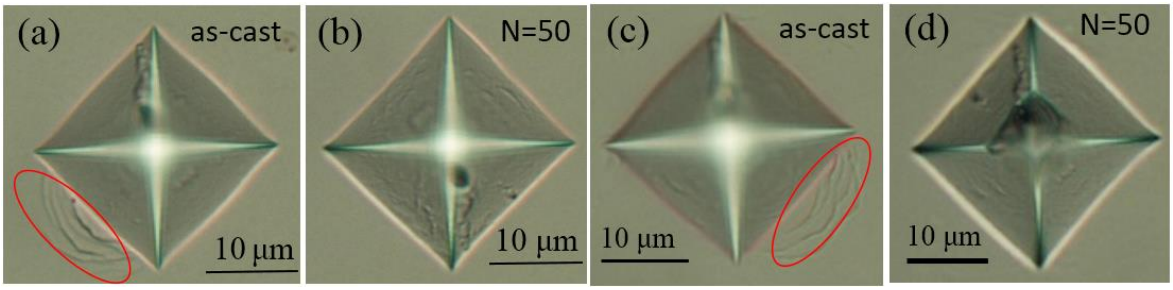

Fig. 3.15. Optical microscope images of the Vickers indent 4 mm from the disk center for Zr55 MG in the as-cast state (a) and after 50 rotations of HPT (b), and Zr65 MG in the as-cast state (c) and after 50 rotations of HPT (d). Areas with obvious shear banding are encircled by the red line.

3.2.2.2 Nanoindentation

The evolution of the mechanical properties induced by HPT was also analyzed using nanoindentation. Fig. 3.16(a) shows typical load-depth curves of the as-cast and HPT-deformed Zr55 samples. The maximum indentation depth increased with increasing N, signifying strain-softening by structural rejuvenation. Moreover, the pop-in behavior associated with discrete shear band propagation [97, 98] disappeared in the sample deformed by 50 rotations, demonstrating that the deformation during nanoindentation became less localized after HPT. The disappearance of pop-in was directly reflected in the indent morphology. Scanning probe microscope (SPM) image in Fig. 3.16(b) shows pile-ups around the indent in the as-cast sample. In comparison, no pile-up can be seen in the sample deformed by 50 rotations (Fig. 3.16(c)). Thus, HPT significantly reduced the extent of strain localization and made the deformation more homogeneous [37]. The sample plasticity was evaluated by the plastic criterion (R_w), which is defined by the ratio between the residual displacement after unloading and the maximum displacement during loading [75]. In the case of Zr55, the R_w increased from 0.681 ± 0.009 to 0.701 ± 0.012 after HPT to $N = 50$, demonstrating an improvement in plasticity.

On the other hand, in the case of Zr65 (Fig .3.16(d)), pop-in can still be observed in the load-depth curve even for the sample deformed to 50 rotations, and pile-ups around the indents related to the formation of discrete shear bands remained in existence (Fig. 3.16(e) and (f)). Correspondingly, there was only a slight increase in R_w, from 0.700 ± 0.011 to 0.709 ± 0.008.

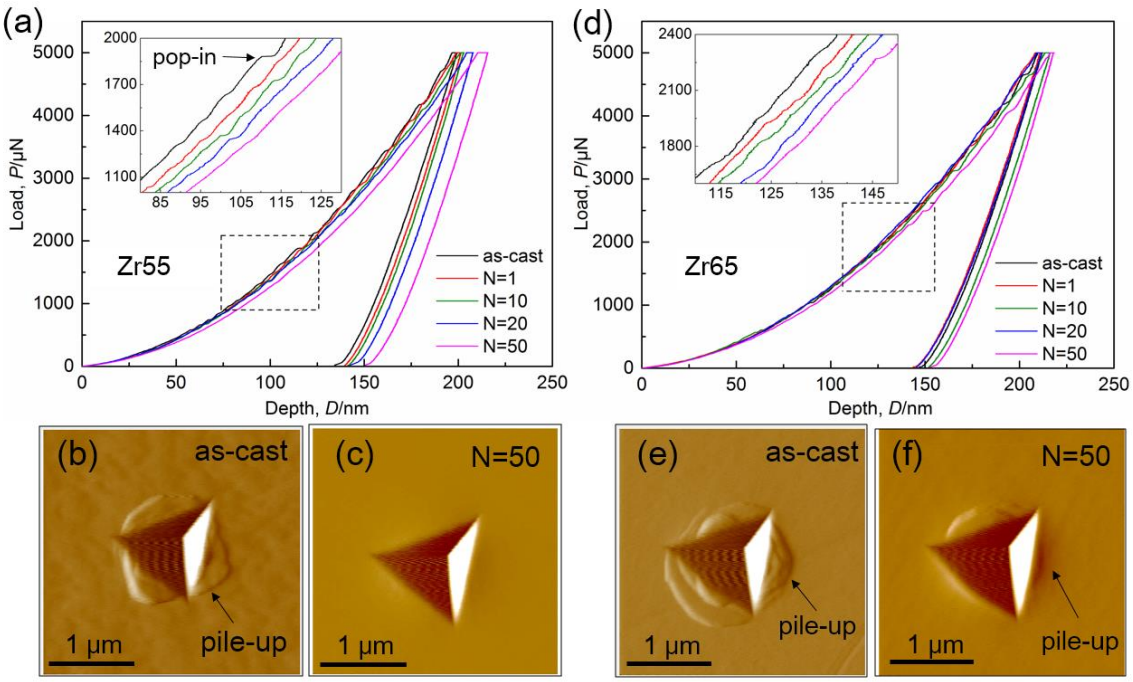

Fig. 3.16. (a) Load-depth curves of the as-cast and HPT-deformed Zr55 samples. The inset shows an enlarged view of the curves marked by a dashed square. (b) SPM image of Zr55 in the as-cast state. (c) SPM image of Zr55 deformed by N = 50 rotations. (d) Load-depth curves of the as-cast and HPT-deformed Zr65 samples. The inset shows an enlarged view of the curves marked by a dashed square. (e) SPM image of Zr65 in the as-cast state. (f) SPM image of Zr65 deformed by N = 50 rotations.

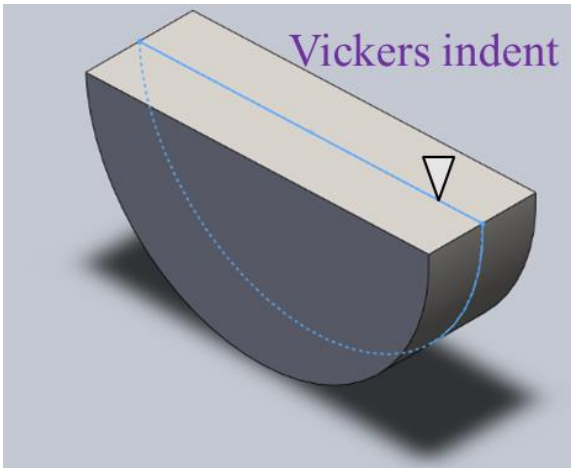

Fig. 3.17. Schematic illustration of the Vickers indent for the purpose of shear band observation.

The development of shear bands beneath the surface can be observed analogously using Vickers indent. The indentation was performed on the interface of two mirror-polished half disks (Fig. 3.17) using a load of 200gf. For the as-cast Zr55 sample (Fig 3.18), we can see two kinds of shear bands: semicircle and radial. The semicircle shear bands were intercepted by the radial ones, creating shear off-set. The space between semicircle

shear bands lies in the range from 0.1 to 1 micron, and gradually increase with depth. For the sample after 50 rotations, instead of well-defined semicircle shear bands, one can only see the tiny wavy pattern with much smaller spacing between each peak. The radial shear bands with a larger spacing can be also observed. This suggested that the shear band density is higher in the HPT-deformed sample than in the as-cast one, indicating the shear band propagation is less discrete. In contrast, for the as-cast Zr65 sample (Fig. 3.19), the shear bands are irregular and convoluted. Probably as a result of interception among well-developed semicircle and radial shear bands, which is typical for samples with a lower hardness [99]. After high-pressure torsion, the shear bands become less defined and one can see some semicircle shear bands as deformation proceeds away from the indent. The shear band propagation beneath the Vickers indent is analogous to that under nanoindentation.

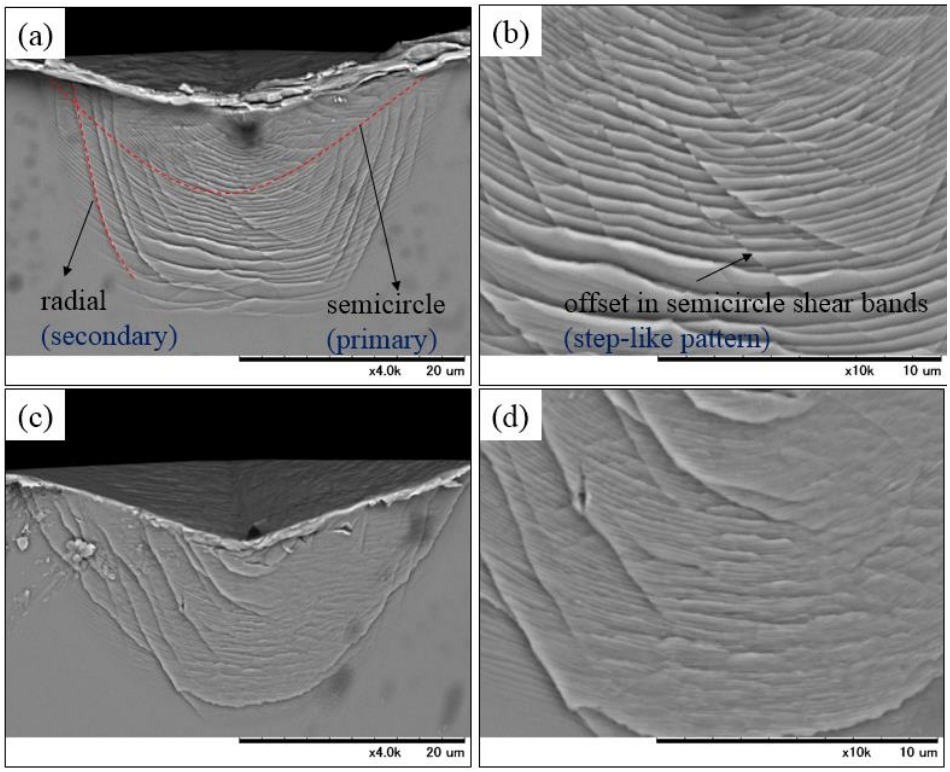

Fig. 3.18. Cross-sectional images of shear band patterns underneath a Vickers indentation for Zr55 as-cast ((a) and (b)) and HPT-deformed (N = 50) ((c) and (d)) samples.

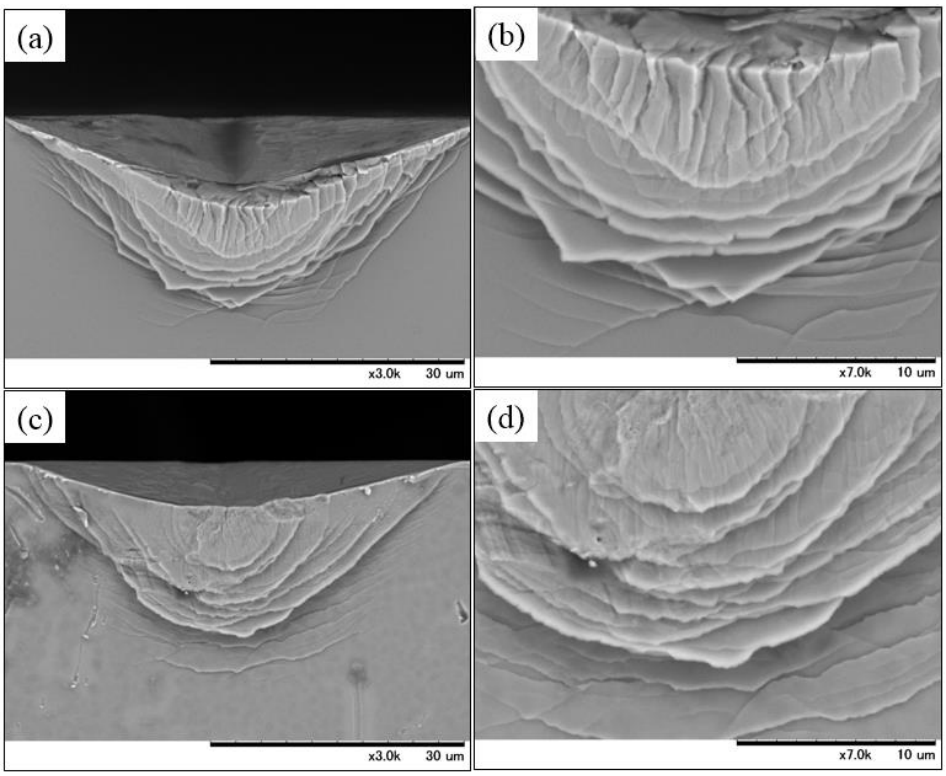

Fig. 3.19. Cross-sectional images of shear band patterns underneath a Vickers indentation for Zr65 as-cast ((a) and (b)) and HPT-deformed (N = 50) ((c) and (d) samples.

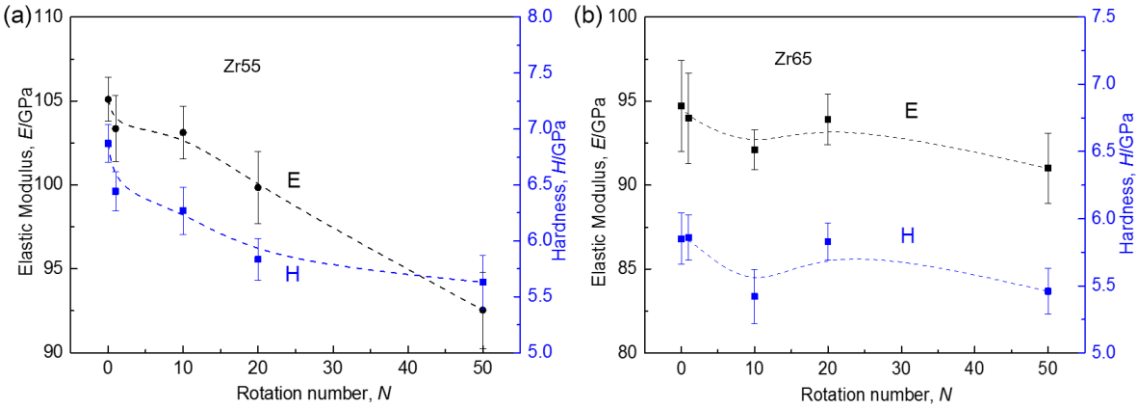

Fig. 3.20. Elastic modulus E and hardness H plotted against the number of rotations N for (a) Zr55 and (b) Zr65 MGs.

The calculated values of elastic modulus (E) and hardness (H) are plotted as a function of N in Fig. 3.20. (The Poisson ratio of the Zr55 and Zr65 for the calculation using equation 2.3 is estimated to be 0.363 and 0.370, respectively [100].) The E and H of Zr55 decreased with N from 105.1 ±1.3 GPa and 6.87 ±0.17 GPa in the as-cast state to 92.5 ±2.3 GPa and 5.63 ±0.24 GPa at N = 50, respectively. In comparison, the decrease in E and H of Zr65 was smaller, from 94.8 ±2.7 GPa and 5.85 ±0.19 GPa in as-cast condition to 91.0 ±2.1 GPa and

5.46 ±0.17 GPa at N = 50, respectively. Interestingly, both E and H seem to rise slightly as N increases from 10 to 20. One may assume that this could be attributed to nanocrystallization in the N = 20 sample. However, TEM observation (not shown) confirmed that there was no sign of crystallization. The above results obtained from nanoindentation suggested that strain softening and delocalization of deformation induced by HPT was more prominent in Zr55 than in Zr65.

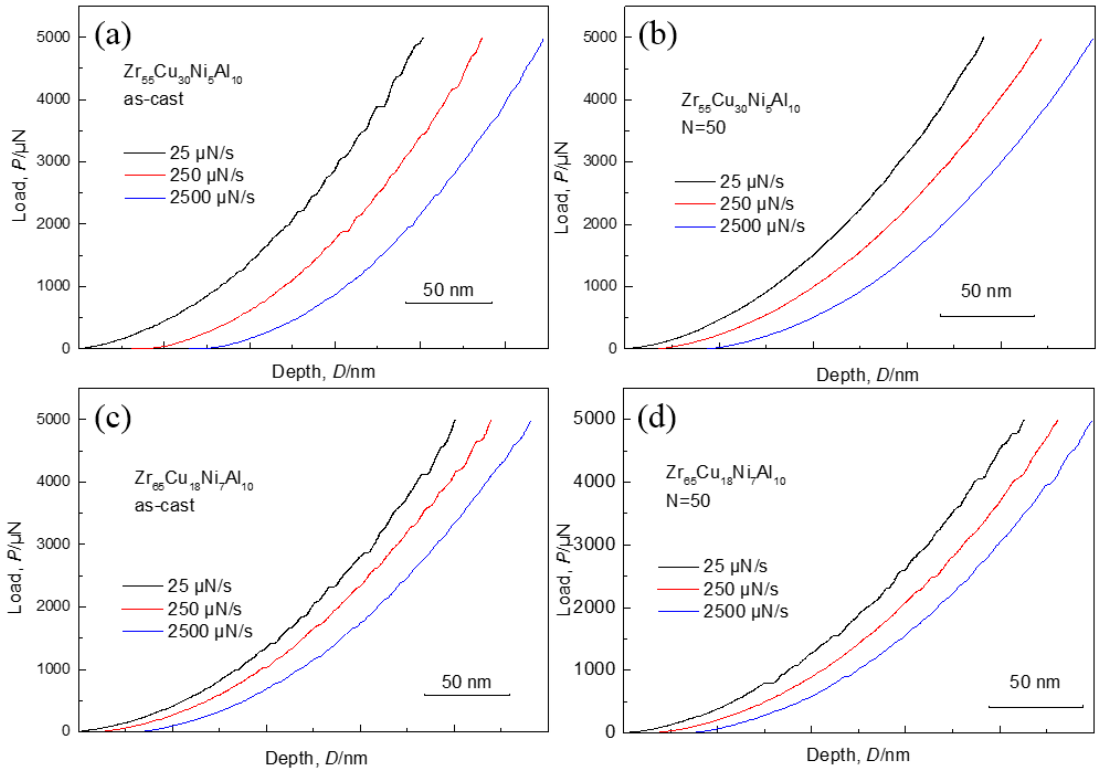

Fig. 3.21. Loading curve of nanoindentation tests at different loading rates for Zr55 MG in the as-cast state (a) and after 50 rotations of HPT (b); and Zr65 MG in the as-cast state (c) and after 50 rotations of HPT (d).

The pop-in behavior observed in Fig. 3.16 is dependent on the loading rate. Fig. 3.21 displays the loading part of the load-depth curves at different loading rates for the Zr55 and Zr65 MGs in the as-cast and deformed (N = 50) states. In these figures, the starting point of the each curve is displaced so that multiple curves can be seen clearly. For both Zr55 and Zr65 MGs, it is apparent that the number and magnitude of pop-in decrease with loading rate, suggesting a transition from discrete to continuous yielding [98]. Increasing loading rate across two orders of magnitude from 25 to 2500 μN/s caused the nature of serration to change substantially, namely, from the step-like curves at low loading rates to the ripple-shaped curves. The variation tendency is similar for the HPT-deformed sample, only that the serration was less obvious. It should be noted that the reduction in the number and magnitude of the pop-in induced by HPT was more pronounced for Zr55 MG.

specifically, pop-in can still be observed for the Zr65 MG deformed by N = 50 HPT at a loading rate of 2500 μN/s.

In fact, during nanoindentation with a constant loading rate, the indentation strain rate ($\dot{\varepsilon}$) is not a linear function of time. Instead, it is defined by the following equation [98]:

$$\dot{\varepsilon} = \frac{1}{h}\frac{\mathrm{d}h}{\mathrm{d}t} \tag{3.5}$$

In Fig. 3.22, the indentation strain rate is plotted as a function of depth. At the beginning of each experiment, the strain rate was very high (as the denominator h is close to zero), but decreased with depth and gradually approached an approximately constant value. As the figures for the as-cast samples illustrate (Fig 3.22 (a) and (c)), the curves are not smooth or monotonic, but exhibit many short peaks, especially at a low loading rate. These short peaks correspond to the pop-ins that were shown in Fig 3.18. For the HPT-deformed samples, peaks can also be observed but the magnitude and number were considerably smaller, only a few short peaks can be observed in the sample deformed by N = 50 HPT at the loading rate of 2500 μN/s. The decrease in the number of pop-in with increasing loading rate suggests the high loading rate suppresses the nucleation and propagation of shear bands.

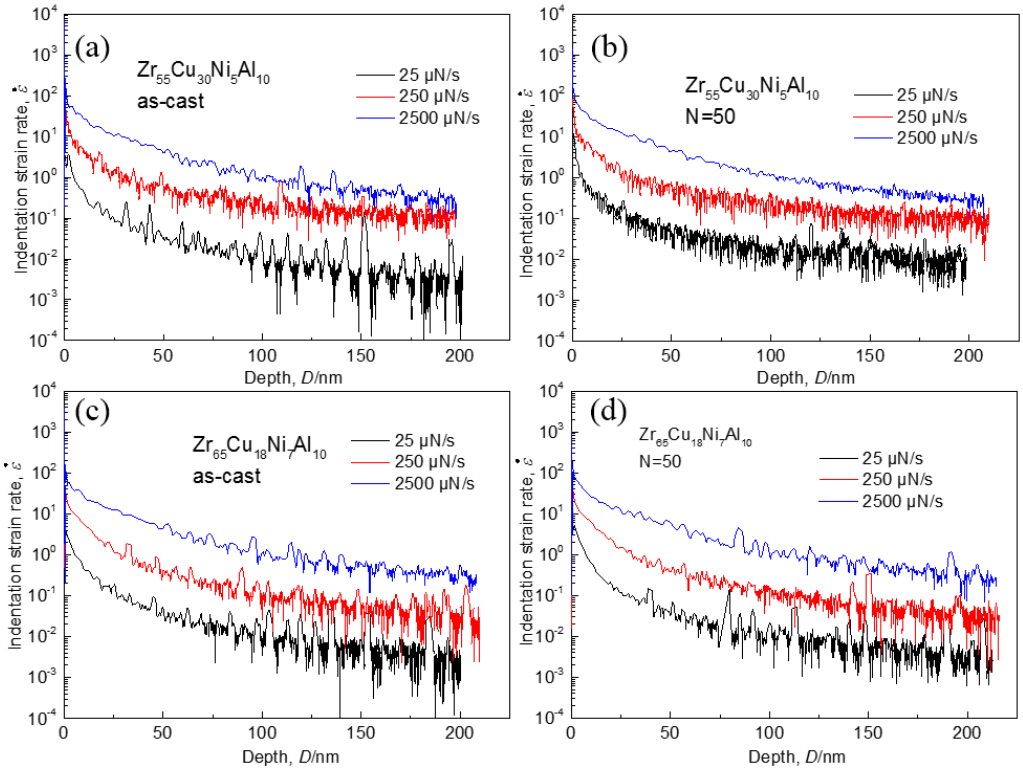

Fig. 3.22. Indentation strain rate at different loading rates for Zr55 MG in the as-cast state (a) and after 50 rotations of HPT (b); and Zr65 MG in the as-cast state (c) and after 50 rotations of HPT (d).

3.2.2.3 Nanoscratch

In order to get another perspective of the deformation mode, nanoscratch was performed on the Zr55 and Zr65 MGs (Fig. 3.23). The tests were performed at a constant normal force of 1000 μN at different scratch rates. As can be seen, the HPT-deformed samples exhibited a lower coefficient of friction, which could be attributed to the decrease in hardness after HPT [101]. Furthermore, the coefficient of friction seems to be scratch-rate independent, which could be attributed to the fact that the scratch rate in this study is low such that adiabatic heating can be neglected [101]. On the other hand, the curves of the as-cast sample were more serrated, especially at the beginning for a low scratch rate. Such serration behavior gradually disappears with increasing scratch rate. The change of the deformation mode can be directly observed from the morphology of the scratch (Fig. 3.24 and Fig. 3.25). For the as-cast sample, the scratch consists of hump and saddle like parts when the scratch rate is low, which correspond to the serration of the curves in Fig. 3.23. At a higher rate, the scratch became more uniform like a ridge. The HPT deformed sample shows similar feature, except that the profile of the deformed sample at a lower speed was smoother.

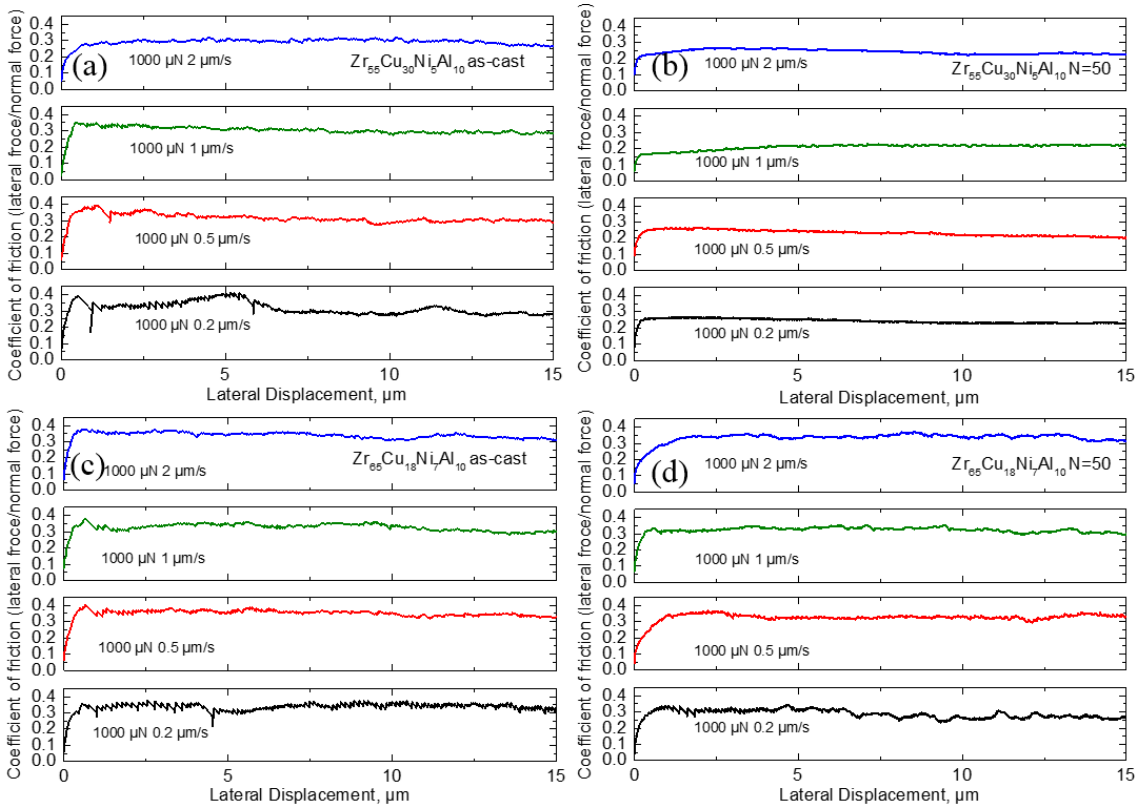

Fig. 3.23. Coefficient of friction at different loading rates for Zr55 MG in the as-cast state (a) and after 50 rotations of HPT (b); and Zr65 MG in the as-cast state (c) and after 50 rotations of HPT (d).

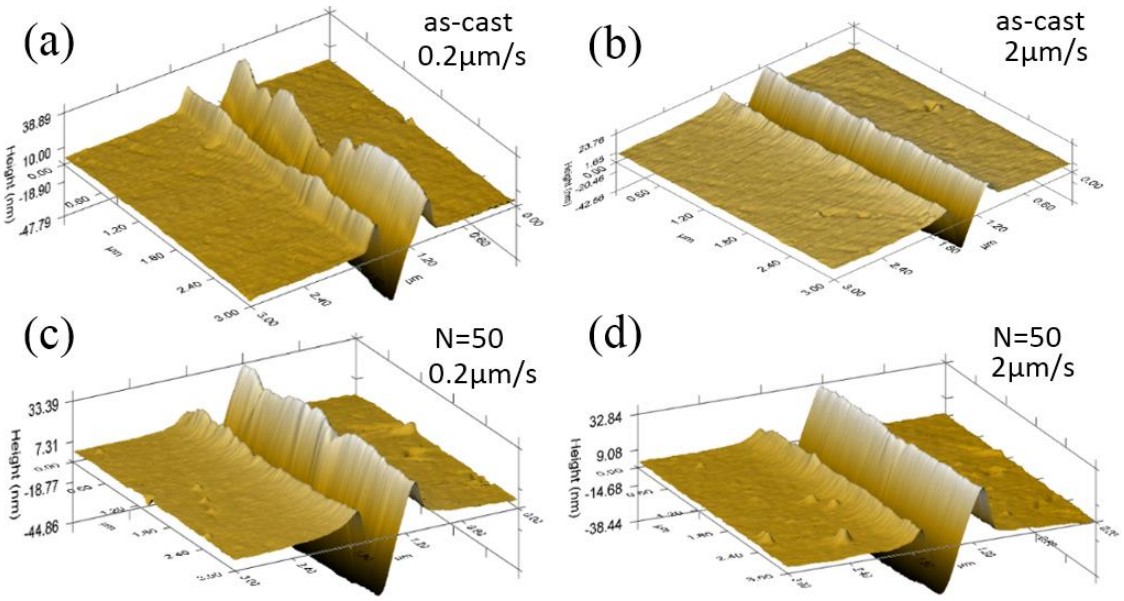

Fig. 3.24. Groove morphology of the as-cast Zr55 MG scratched at (a) 0.2 μm/s and (b) 2 μm/s; and HPT-deformed (N = 50) Zr55 MG scratched at (c) 0.2 μm/s and (d) 2 μm/s.

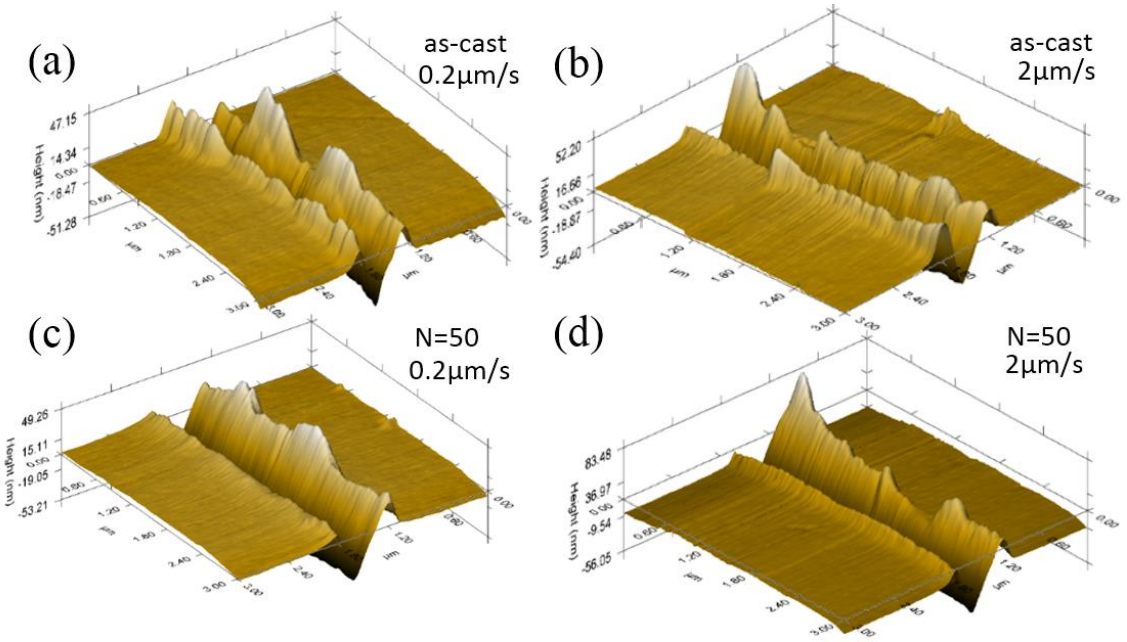

Fig. 3.25. Groove morphology of the as-cast Zr65 MG scratched at (a) 0.2 μm/s and (b) 2 μm/s; and HPT-deformed (N = 50) Zr65 MG scratched at (c) 0.2 μm/s and (d) 2 μm/s.

3.2.2.4 Tensile tests

Tensile tests were performed on the sample wire-cut sample (see Fig. 2.6) to evaluate the changes in the mechanical properties on a larger scale. Similar to the results obtained from nanoindentation, after 50 rotations, the elastic modulus of Zr55 dropped from 98 GPa to 86 GPa, and the tensile stress (σ_f) decreased from 1.61 GPa to 1.52 GPa (Fig 3.26). The non-linearity of the stress-strain curve could be caused by the flawed sample preparation method and the small dimension of the samples that caused poor contact between the specimen and the gauge. It should be noted that the elastic modulus measured by tensile tests in smaller than that measured by nanoindentation because equation 2.2 fails to take into account the contribution of pile-up to the projected area. There was no pronounced improvement in plasticity. Both samples fractured catastrophically after approximately two percent elastic deformation (Fig. 3.26).

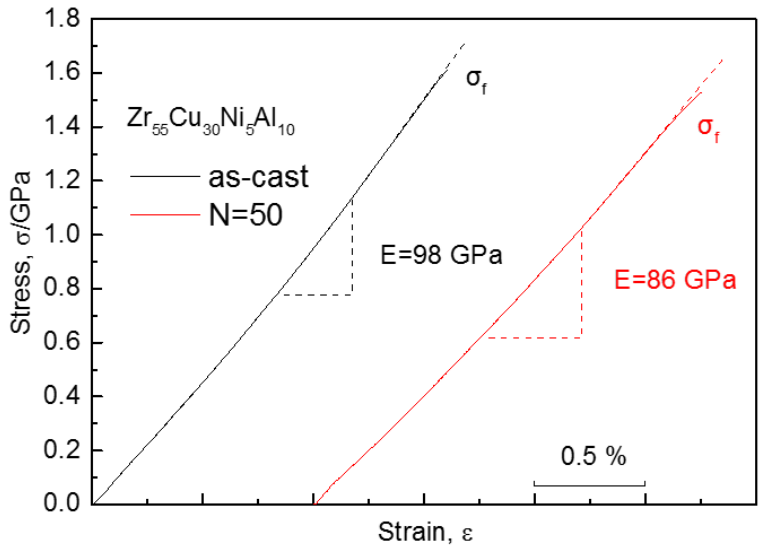

Fig. 3.26. Stress-strain curves of as-cast and HPT-deformed (N = 50) Zr55 MGs.

Even so, one can still see some difference in terms of the fracture morphology (Fig. 3.27). For the as-cast sample, only the primary shear plane can be seen, but several shear bands became discernible after 50 rotations of HPT. Nonetheless, it was not enough to cause a significant increase in the plasticity. The deviation of the fracture angle (θ_t) from 45 ° indicates that fracture of MGs is a combined effect of normal and tensile stress [102]. On the fracture surface of the as-cast sample (Fig. 3.28), shear bands form the core (encircled by the red dash line) and vein patterns; however, for the HPT-deformed sample, one can see the branching of the vein patterns, forming secondary veins. The average length of vein patterns is much smaller in this case and the expansion of is more multi-directional, which is similar to the less localized deformation during

nanoindentation. It has been proposed that fracture originates from the core (induced by normal stress) and then propagate towards outside the core forming vein pattern (driven by shear stress) [102].

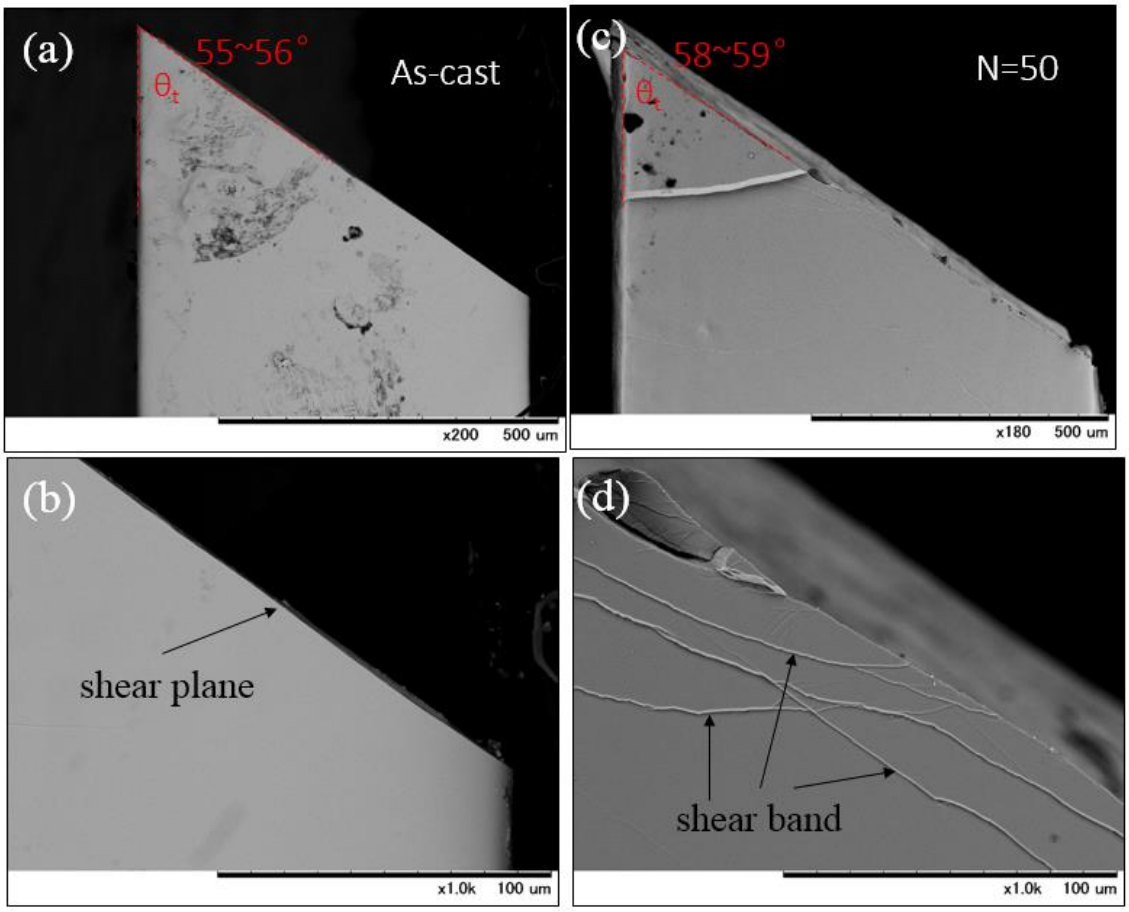

Fig. 3.27. Shear plane of the as-cast ((a) and ((b)) and deformed ((c) and ((d)) Zr55 MGs.

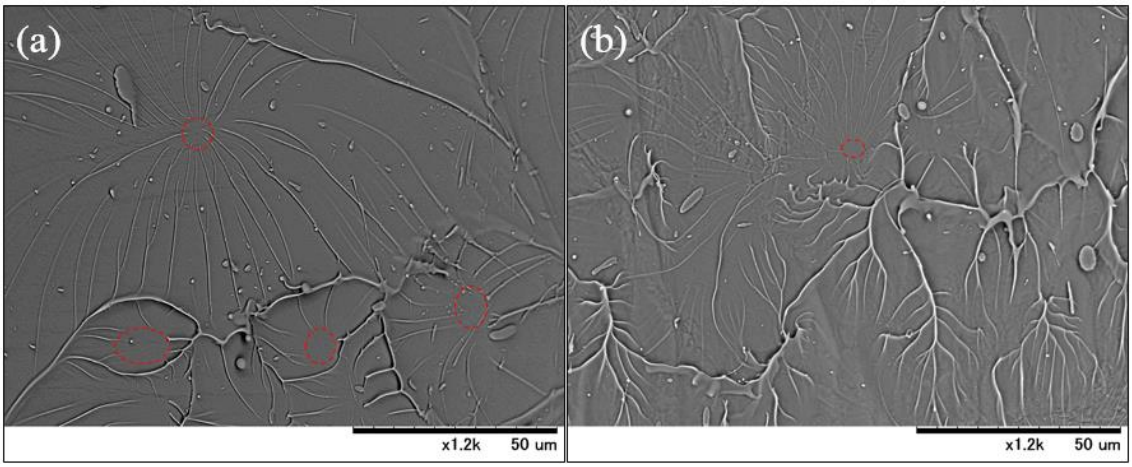

Fig. 3.28. Facture surface of the (a) as-cast and (b) deformed (N = 50) Zr55 MGs.

On the other hand, the changes of mechanical properties for Zr65 is less obvious in tensile tests. As shown in Fig. 3.29, after 50 rotations, the elastic modulus of Zr65 dropped from 85 GPa to 80 GPa, and the tensile

stress (σ_f) decreased from 1.47 GPa to 1.46 GPa. The fracture morphology of the as-cast Zr65 MG is like that of the Zr55, exhibiting a primary shear plane on the side-view and core and vein pattern on the facture surface (Fig. 3.30). However, the fracture surface of the Zr65 N = 50 sample is very peculiar (Fig. 3.31). The fractured area seemed to be composed of three patterns: i) droplet, ii) honeycomb and iii) mirror-like. To the author's knowledge, such a complex fracture pattern has never been reported before, and the formation mechanism remains unclear. One possible explanation is that shear band consists of a cold front and a hot tail, which result in the droplet and mirror-like patterns, respectively [103].

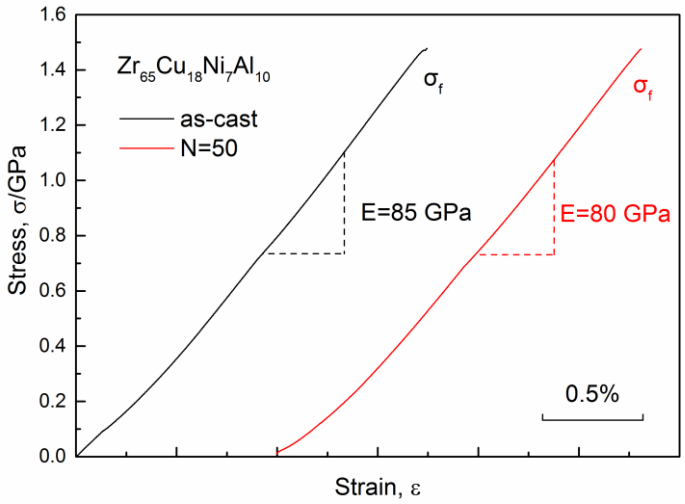

Fig. 3.29. Stress-strain curves of as-cast and HPT-deformed (N = 50) Zr65 MGs.

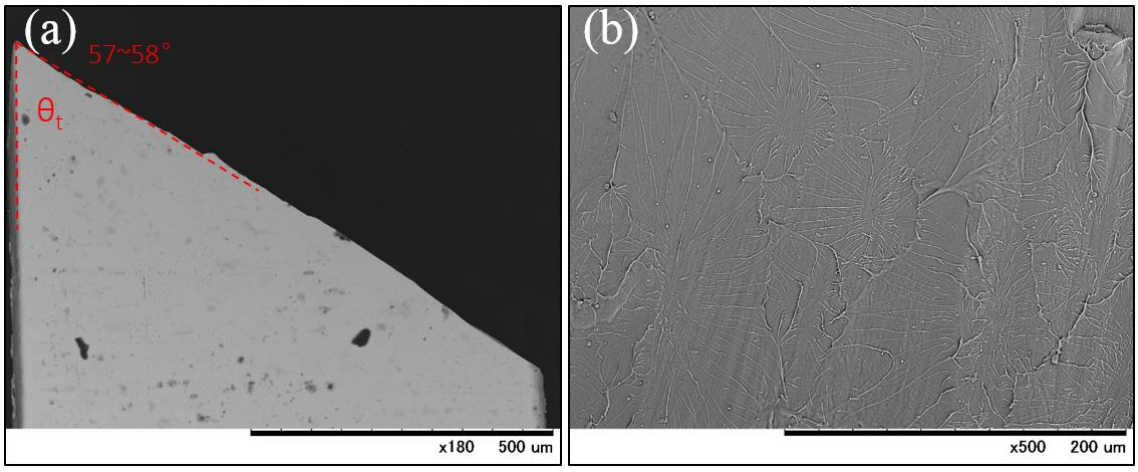

Fig. 3.30. Fracture morphology of the as-cast Zr65 MG on the side-view (a) and on the fracture surface (b).

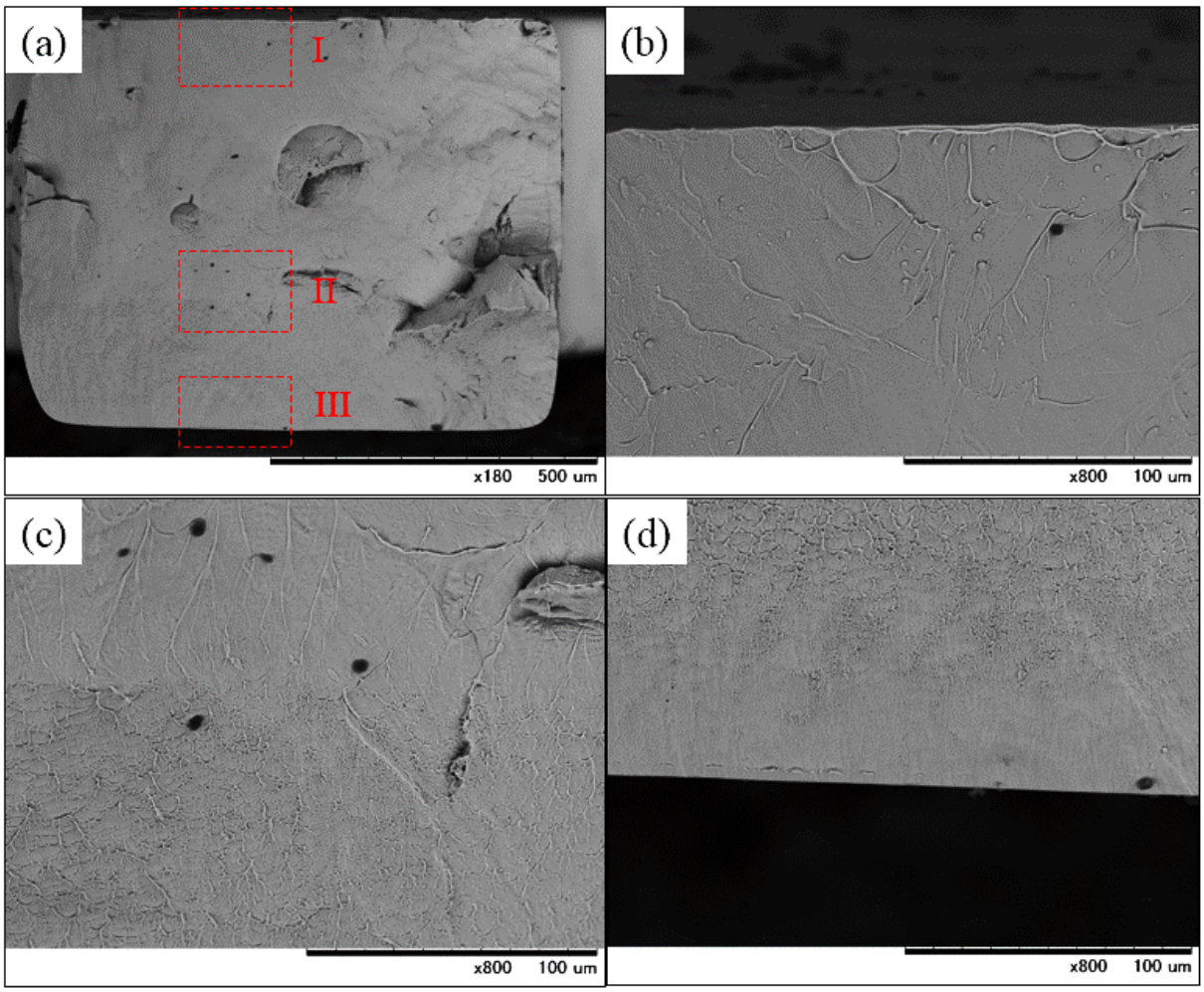

Fig. 3.31. Facture surface of the (a) *N* = 50 Zr65 MG. (b)-(d) are the enlarged images of areas I-III.

3.2.2.5 Dependence of the mechanical and thermal property on structural rejuvenation

HPT induced obvious strain-softening in Zr55 and Zr65 MGs (lowering of *E* and *H*). It is also apparent that the deformation became more homogeneous after HPT, as were seen in the absence of pop-in and pile-up (Fig. 3.16), uniform groove morphology of the nanoscratch (Fig. 3.24 and 3.25) and well-expanded shear bands in tensile tests (Fig. 3.27). As introduced earlier at the beginning of this chapter, plastic deformation of an MG is mediated by the shear transformation zones (STZs). Studies have shown that STZs are more likely to be generated in local areas with certain structural features, *e.g.* areas with more structural disorder [104], larger free volume [105], or under higher atomic-level stresses [106].

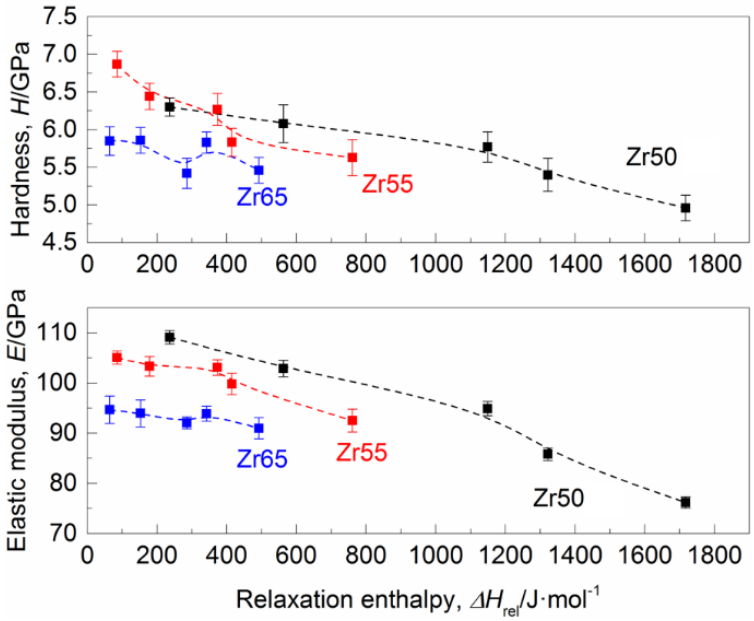

Fig. 3.32. Hardness H and elastic modulus E plotted against ΔH_{rel} for Zr50 (ref. [37]), Zr55 and Zr65 MGs.

Free volume refers to the part of thermal expansion, or excess volume that can be re-distributed without energy change [13]. Under the application of external force, atom clusters around the free volume may be activated to compensate shear strain, and this cluster of atoms is called STZ. The STZ propagates as deformation proceeds, once the size of STZ reaches a critical value in a particular direction, shear band will form and localized deformation would ensue. The difference between the as-cast sample and the HPT-deformed sample is that there is more free volume in the latter, which is indicated by a larger ΔH_{rel} as demonstrated in equation 3.3. The increase in ΔH_{rel} was accompanied by a reduction in H and E (Fig. 3.32), similar to a previous research conducted on $Zr_{50}Cu_{40}Al_{10}$ (Zr50) MG [37]. As a result of the net increase in free volume, the activation of STZ in the HPT-deformed sample would be easier than in the as-cast one. Furthermore, there are more possible directions along which the STZ can flow. Therefore, HPT-deformed samples exhibit relatively homogeneous plastic deformation. On the other hand, structural rejuvenation is also accompanied by the creation of shorter atomic bonds (anti-free volume) [38]. Acting as crystallization embryos, these sites may deteriorate the thermal stability of the supercooled liquid by lowering T_x [107-109], although not necessarily change the crystallization mode. In our present study, the deterioration of the thermal stability of Zr65 is more drastic than the case of Zr50 and Zr55, which suggests a higher extent of shorter atomic bonds creation. It is noteworthy that the microstructure-property relationship of an MG can also be interpreted from

the perspective of polyhedral clusters [34] or "flexibility volume" [17]. The concept of "free volume" was adopted in this section as the structural indicator for simplicity.

3.3 Composition dependence of mechanically-induced structural rejuvenation

Both Zr55 and Zr65 exhibited a smaller increase in ΔH_{rel} compared to that reported for Zr50 subjected to HPT under the same processing conditions [37]. This difference in the extent of structural rejuvenation can be attributed to the difference in their atomic topological structures. A number of molecular dynamics simulations show that in Zr-Cu MGs and supercooled liquids, an icosahedral short-range order with the Voronoi index being <0, 0, 12, 0> is one of the most populous constituent clusters [19, 34, 110, 111].

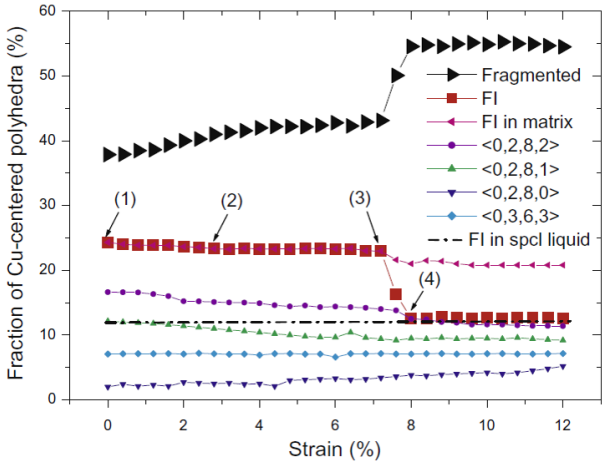

Fig. 3.33. Fractions of the dominant polyhedrons as a function of strain in the region that evolves into the localized band [111]. (FI: full icosahedral)

The more solid-like and ordered icosahedral clusters will be partially destroyed by plastic deformation [19], leading to a growth in the number of less shear-resistant fragmented clusters [111] (Fig. 3.33). These fragmented clusters are more liquid-like as well as more prone to becoming shear transformation zones [111]. Therefore, plastic deformation during HPT can lead to a drastic decrease in the population of relatively ordered structures [111], which increases the level of disordering and the number of geometrically unfavored motifs [18]. Specifically in the binary Zr-Cu system, the proportion of the icosahedral clusters strongly depends on composition. Cheng *et al.* pointed out that the amount of icosahedral clusters would decrease with an increasing Zr/Cu ratio [112]. It is therefore reasonable to speculate that a lower Zr/Cu ratio (more ordered structure) can result in a higher potential for disordering, *i.e.* structural rejuvenation. This speculation matches well with the results that Zr50 with the lowest Zr/Cu ratio exhibited the largest increase in ΔH_{rel} and that Zr65 exhibits the

smallest increase. The effect of Al is not discussed here, because Zr50, Zr55 and Zr65 have the same amount of Al. Nonetheless, it is worth mentioning that Al has a significant influence on the topological and electronic structure of an MG [113]. Simply speaking, the addition of Al would increase the covalency of the interatomic bonds, which enhances the number and symmetry of the icosahedral SRO as well as the spatial connectivity (*i.e*. MRO).

Continuing the discussion on the icosahedral clusters, during liquid quenching, the number of the icosahedral cluster will increase as the supercooled liquid undergoes glass transition, reaching a more ordered atomic structure [110]. This ordering process tends to be more pronounced for a more fragile liquid [110], in which the relaxation time deviates from the Arrhenius behavior. Even under the circumstance that the most dominant short-range order is not icosahedral, the relation between ordering and fragility can still hold true [112]. By definition, a liquid exhibiting a temperature-independent (Arrhenius law) activation energy of viscous flow is the strongest. And a fragile liquid would show some deviation from such independence [114]. According to Adam and Gibbs, the slow-down of the kinetics and thermodynamics of glass formers are closely related to the loss of configuration entropy such that [115, 116]:

$$\eta = A\exp(\frac{B}{TS_c(T)}) \tag{3.6}$$

where η is the viscosity, $S_c(T)$ is the configurational entropy as a function of temperature (T), and A and B are constants. It is straightforward that a strong glass former (a larger η) experiences a less pronounced ordering process (a slighter decrease in S_c).

In order to quantify the degree of deviance from Arrhenius law, the fragility index m was introduced [117]:

$$m = \frac{\partial \log < \tau >}{\partial < T_g / T >}\Big|_{T=T_g} \tag{3.7}$$

where $<\tau>$ is the average relaxation time, and T is the temperature.

Mauro *et al*. also confirmed that fragility depends on the rate of ordering near T_g and the similarity between the MG and liquid, instead of the type of ordering [114]. In particular, they defined a structural fragility index (γ) proportional to the difference in the structure factors ($S(q)$) of the metallic liquid and the supercooled liquid at T_g, and found that the more fragile the liquid the large the γ. In a different study, it was found that a stronger liquid ($Mg_{65}Cu_{20}Y_{10}$) experiences less pronounced ordering process than a weaker liquid

($Zr_{36}Cu_{64}$), and the latter undergoes a drastic increase in the icosahedral SRO whereas the former experience a slight increase in less ordered <0, 3, 6, 0> and <0, 2, 8, 0> SROs [20]. Lately, Wei *et al*. demonstrated that the fragility is also linked to the rate of expansion of MRO towards more stable network/aggregation schemes [118]. These results combined suggest that the fragility depends on how drastic the ordering process during liquid-to-glass transition escalates. We can therefore assume that an MG formed from a more fragile liquid can be more susceptible to mechanically-induced rejuvenation as it has more ordered SROs to start with, which is similar to Greer and Sun's speculation on thermally-induced one [36]. Calculated by fitting thermodynamic parameters using the following equation [117, 119]:

$$m = \frac{DT_0T_g}{(T_g - T_0)^2 \ln 10} \tag{3.8}$$

where m is the fragility index, D is the strength parameter controlling how closely the liquid system obeys the Arrhenius law, and T_0 is the asymptotic value of T_g, usually can be taken as the onset of the glass transition within the limit of an infinitely slow cooling and heating rate. The D and T_0 can be fitted by the equation:

$$\ln \Phi = \ln B - \frac{DT_0}{T_g - T_0} \tag{3.9}$$

where Φ is the heating rate and B is a timescale parameter. The m of Zr50, Zr55 and Zr65 glass-forming liquid calculated at a heating rate of 20 K/min using equation 3.8 is 46, 42 and 35, respectively. Indeed, for these three MGs, the most pronounced structural rejuvenation was observed in the composition formed from the most fragile liquid. The curves fitted by equation 3.8 is shown in Fig. 3.34.

Extending this idea to more general circumstances, Fig. 3.35 shows the correlation between the fragility and the increase in ΔH_{rel}, together with data in literature obtained on various MG systems rejuvenated by the same or very similar processes [35, 82, 83, 91, 96, 120, 121]. Table 3.2 provides a detailed list about the compositions and processing conditions. It seems clear that the level of rejuvenation (increase in ΔH_{rel}) and fragility are positively related. Even though there could exist a large discrepancy between the values of fragility obtained by thermodynamic and kinetic methods [119], the theoretical argument based on this concept is valid. To reiterate, rejuvenating a more ordered glass (formed from a more fragile liquid) would be easier than to rejuvenate an already relatively disordered one [34].

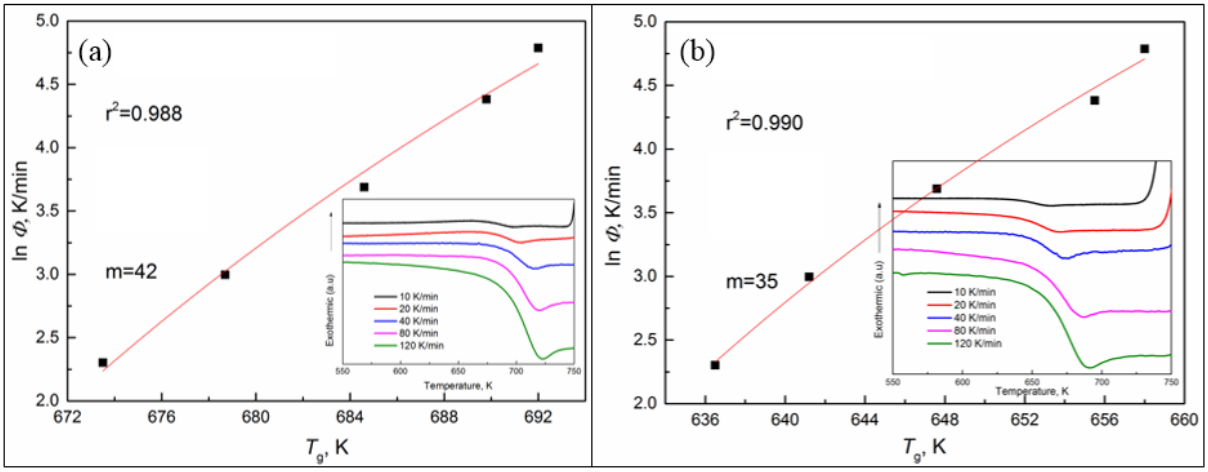

Fig. 3.34. Heating rate (Φ) plotted as a function of glass transition temperature (T_g) for the calculation of fragility index. (a) and (b) represent the case of Zr55 and Zr65 MGs, respectively. The insets are the DSC curves at different Φ.

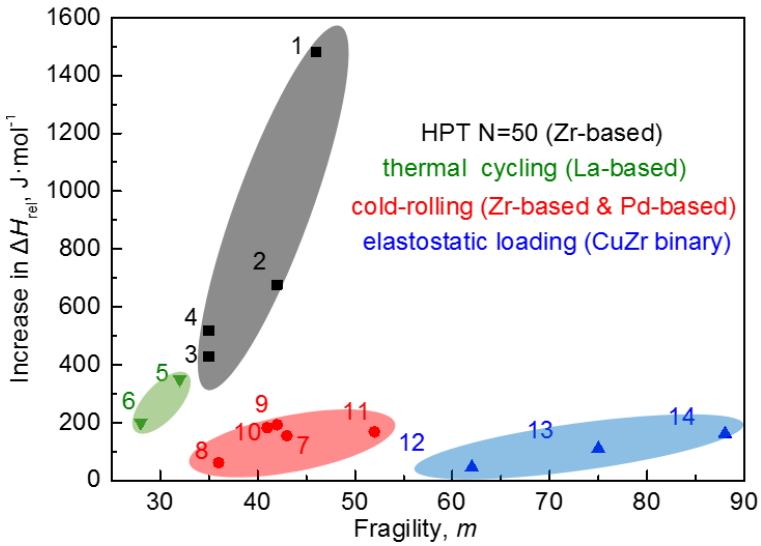

Fig. 3.35. Plot of ΔH_{rel} obtained by various rejuvenation methods versus liquid fragility of the processed samples. The values of ΔH_{rel} are from ref. [91] (#4 $Zr_{65}Cu_{17}Ni_5Al_{10}Au_3$), ref. [35] (#5 $La_{55}Ni_{20}Al_{25}$ and #6 $La_{55}Ni_{10}Al_{35}$), ref. [120] (#7 $Zr_{46.5}Cu_{45}Al_7Ti_{1.5}$ and #8 $Zr_{64.14}Cu_{15.75}Ni_{10.12}Al_{10}$), ref. [83] (#9 Zr55), ref. [96] (#10 $Pd_{38}Ni_{40}P_{22}$), ref. [121] (#11 $Pd_{77.5}Cu_6Si_{16.5}$) and ref. [82] (#12 $Zr_{50}Cu_{50}$, #13 $Zr_{43}Cu_{57}$, #14 $Zr_{35}Cu_{65}$). Fragility of alloy #4-14 or similar compositions were obtained from ref. [119, 122-124].

Compared with other rejuvenation methods by plastic deformation such as cold-rolling or shot-peening, HPT can induce a much higher strain and can deform the whole sample instead of just the surface. In terms of the increase in ΔH_{rel}, HPT seems to be the most effective. Taking the Zr55 MG as an example, the maximum increase in ΔH_{rel} is ~200 J/mol after cold-rolling to 63% thickness reduction [83], and 505 J/mol after heating

up to 1.07 T_g followed by fast cooling [33]. On the other hand, thermal cycling and plastic deformation could have a different influence on the relaxation spectrum. Specifically, T_{onset} would remain unchanged after thermal cycling as reported in ref. [35] whereas it decreased from ~0.75T_g to ~0.6T_g after plastic deformation by HPT (Fig. 3.12). The lowering of T_{onset} could be related to an enhanced β-relaxation [36].

Table 3.2 Lists of the MGs subjected to different methods of rejuvenation.

Alloy number	Processing methods	Composition	Fragility	Increase in ΔH_{rel} (J/mol)
1	50 rotations of HPT	$Zr_{50}Cu_{40}Al_{10}$	46	~1480
2		$Zr_{55}Cu_{30}Ni_5Al_{10}$	42	~680
3		$Zr_{65}Cu_{17}Ni_5Al_{10}Au_3$	35	~430
4		$Zr_{65}Cu_{18}Ni_7Al_{10}$	35	~520
5	Thermal cycling	$La_{55}Ni_{20}Al_{25}$	32	~300
6		$La_{55}Ni_{10}Al_{35}$	28	~200
7	Cold-rolling to ~60% thickness reduction	$Zr_{46.13}Cu_{15.75}Ni_{10.12}Al_{10}$	36	~140
8		$Zr_{46.5}Cu_{45}Al_7Ti_{1.5}$	43	~310
9		$Zr_{55}Cu_{30}Ni_5Al_{10}$	42	~170
10		$Pd_{38}Ni_{40}P_{22}$	41	~180
11		$Pd_{77.5}Cu_6Si_{16.5}$	52	~170
12	Elastostatic loading at 90% fracture strength for 12 hours	$Zr_{50}Cu_{50}$	62	~45
13		$Zr_{43}Cu_{57}$	75	~110
14		$Zr_{35}Cu_{65}$	88	~160

3.4 Summary

HPT deformation induced significant structural rejuvenation in $Zr_{55}Cu_{30}Ni_5Al_{10}$ and $Zr_{65}Cu_{18}Ni_7Al_{10}$ metallic glasses. Such rejuvenation led to a lower E and H, a more homogeneous deformation, and an improved room temperature plasticity. Processed under the same HPT deformation conditions, the observed increase in ΔH_{rel} varied with the chemical compositions of the MGs such that a more pronounced rejuvenation was observed in the MG with the lowest Zr/Cu ratio. An attempt was made to correlate such composition dependence to the fragility of the glass-forming liquid. The results suggested that an MG formed from a more fragile liquid tends to be more susceptible to structural rejuvenation. Our study could promote future research on the compositional dependence of structural rejuvenation as a way to expand the applications of MGs.

Chapter 4 Solid-state amorphization in a Zr-Cu-Al crystalline alloy

4.1 Solid-state amorphization

Amorphous alloys have been studied extensively due to their unique properties such as a high strength, large elastic limit, and good corrosion resistance. Conventionally, bulk amorphous alloys have been fabricated by rapid-quenching of the melt [125]. Solid-state amorphization (SSA) offers another way to produce amorphous alloys by particle beam irradiation [126] or by severe plastic deformation [127]. Mechanism of SSA can be attributed to the introduction of a high density of lattice defects and forced mixing of constituent components [127]. Several methods have been used for SSA by utilizing plastic deformation, such as mechanical alloying [128], cold rolling [5] and high-pressure torsion (HPT) [7, 47, 129, 130]. Since the last century, a number of investigations on amorphization by HPT have been conducted. Stolyarov *et al*. observed partial amorphization of $Pr_{20}Fe_{73.5}B_5Cu_{1.5}$ after 5 rotations of HPT, but the hard magnetic properties were deteriorated [131]. TiNi, one of the most important engineering materials for the shape memory effect, has also been amorphized by HPT [9]. Sun *et al*. investigated the effect of HPT deformation on an alternating stack of pure elemental Cu, Zr and Al sheets to produce binary and ternary amorphous alloys. They observed amorphization, although no clear signature of glass transition was detected in the DSC traces [47]. Meng *et al*. fabricated almost fully amorphous samples using tilt-cast ingots of $Zr_{50}Cu_{50-x}Al_x$ (x = 4, 6, 10) alloys [7]. The initial microstructures (before SSA) were a mixture of Cm and B19' martensite phases, ZrCu with B2 structure, τ_5 ($Zr(CuAl)_2$), and Zr_2Cu. The ZrCu intermetallic compound undergoes martensitic transformation from the B2 structure to two monoclinic martensite phases at ~440 K [44, 45]. One of these martensite phases has a base structure (B19') with $P2_1/m$ symmetry and the other has a superstructure Cm symmetry. The lattice structures of these phases are schematically shown in Fig. 4.1. The SSA was considered to take place preferentially in these martensite phases, and more pronounced amorphization was observed for Zr-44at%Cu-6at%Al and Zr-40at%Cu-10at%Al alloys in accordance with glass forming ability. Glass transition was observed in all compositions and the glass transition temperatures (T_g) were similar to those of rapidly quenched bulk metallic glass (MG) samples. Sundeev *et al*. observed "in-situ" SSA during HPT by monitoring the changes in torque. They thereby suggested "grain boundary sliding" as the primary mechanism for SSA, in which the grain boundary absorbed the newly-generated lattice defects [132].

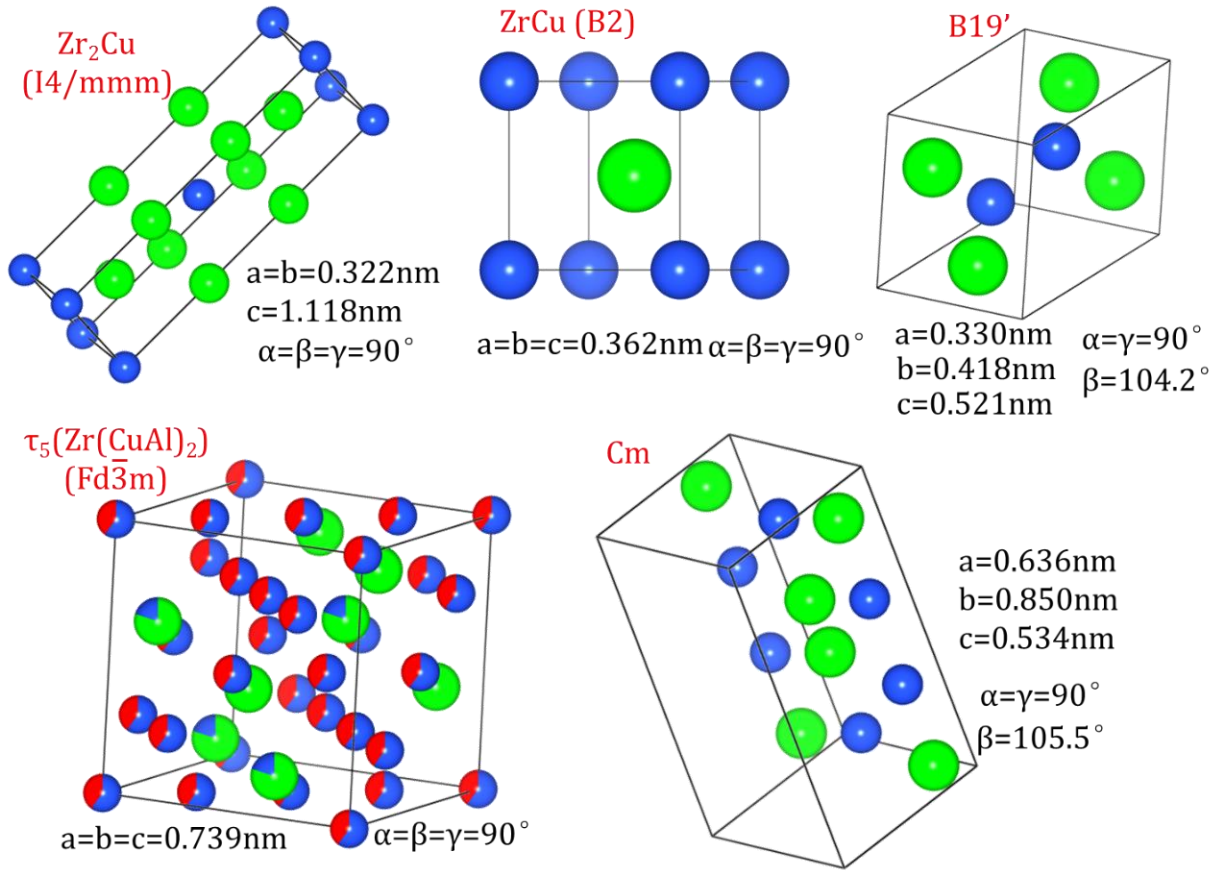

Fig. 4.1. Schematic illustration of the lattice structure of the constituent phases of the Zr-40at%Cu-10at%Al alloy. (The green, blue and red balls correspond to Zr, Cu and Al atoms, respectively.)

The mechanisms of the amorphous phase formation by liquid-quenching and by HPT deformation are very different since there is no liquid-to-glass transition in the SSA. Thus the amorphous alloys fabricated by different methods different structures and properties may exhibit different structures and properties. However, most reports about HPT-induced amorphization are focused on its dependence on chemical composition [7, 47, 130, 133, 134]; and less attention has been paid to the properties of the HPT-amorphized alloys, especially in comparison to the MG made by melt-quenching (MQ). Recently, Yang *et al*. suggested by atomistic simulation that amorphous alloys obtained by SSA are slightly more disordered (*i.e.*, rejuvenated) than the one obtained by MQ [135]. Specifically, SSA produces amorphous phase with a lower atomic packing density and a higher energy state than MQ. However, the confirmation by solid experimental results and the study of the microstructure-property relationships remain unexplored.

In this chapter, the evolution of mechanical and thermal properties of a crystalline Zr-40at%Cu-10at%Al alloy during SSA by HPT will be studied. Comparison of mechanical properties and thermal properties with

those of the tilt-cast $Zr_{50}Cu_{40}Al_{10}$ MG suggests that amorphous phase fabricated from SSA by HPT is more rejuvenated than the one made by MQ.

4.2 Microstructure observation

Cylindrical samples (10 mm diameter) were fabricated by tilt-casting method. The obtained rods were sliced into disks and then annealed at 1073 K for 72 hours in an argon-filled quartz tube to attain full crystallization. The fully crystallized undeformed samples were used as starting material for HPT deformation. The back-scatter electron SEM image of the undeformed sample is displayed in Fig. 4.2, together with the corresponding elemental distribution. It can be seen that before HPT, the sample consists of crystals in the size of several microns with three distinct chemical makeups. As will be shown later in the XRD profiles, the black, grey, and white areas with nominal compositions of $Zr_{36.85}Cu_{42.41}Al_{20.74}$, $Zr_{47.93}Cu_{47.89}Al_{4.19}$, and $Zr_{61.36}Cu_{36.71}Al_{1.94}$ correspond to τ_5, ZrCu, and Zr_2Cu phases, respectively.

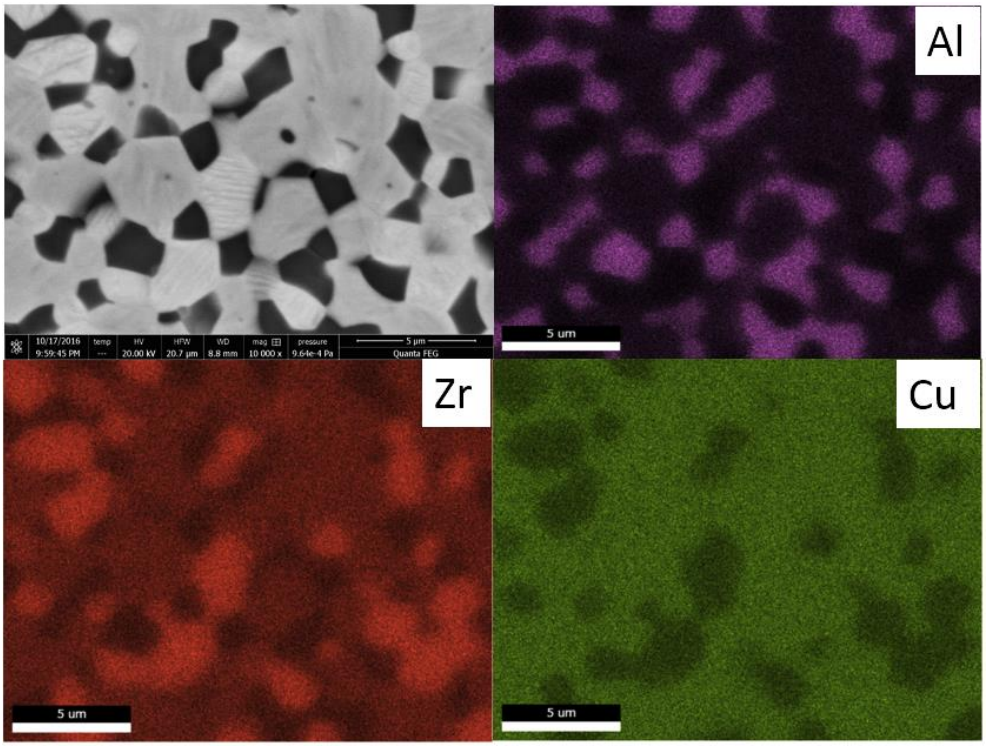

Fig. 4.2. Back-scatter electron SEM images of the fully crystallized undeformed $Zr_{50}Cu_{40}Al_{10}$ alloy, together with the mappings of elemental distribution.

10 rotations of HPT results in significant grain distortion and mixing, leading to the formation of river-like pattern (Fig. 4.3(a)). Increasing the rotation number to 20 renders the microstructure more homogenous. One can only see particles in the size of ~1 μm (Fig. 4.3(b)). After 100 rotations of HPT (Fig. 4.4), no

discernible grains can be observed in the SEM images. It should also be noted that the grain-refinement and elemental mixing were more pronounced at the edge of the sample than at the center where the island-like pattern can be observed (circled by the black dash line in Fig. 4.4).

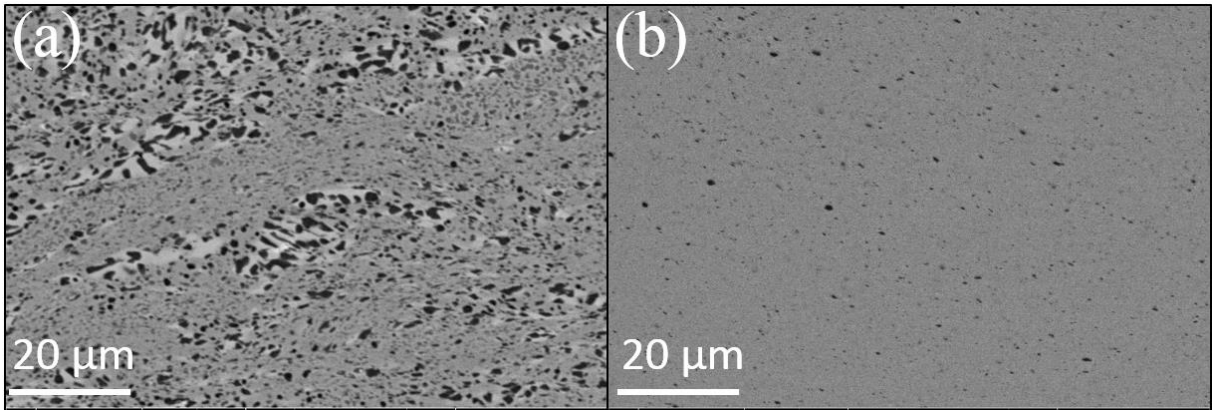

Fig. 4.3. Back-scatter electron SEM images of the Zr-40at%Cu-10at%Al alloy deformed by (a) 10 and (b) 20 rotations of HPT.

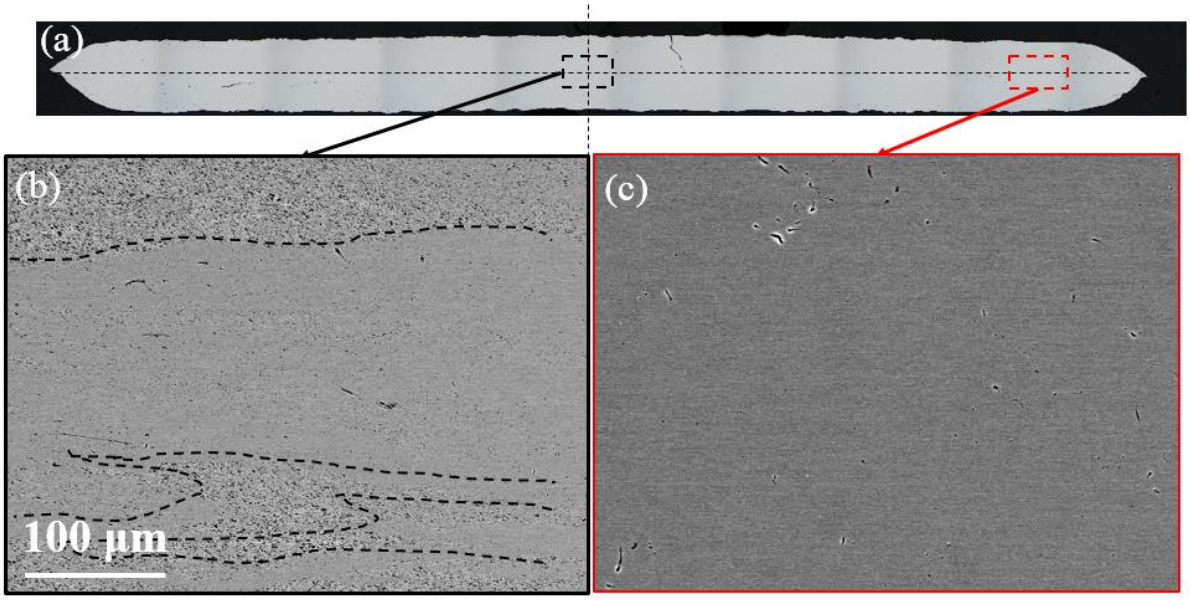

Fig. 4.4. Optical (a) and back-scatter electron SEM images ((b) and (c)) of the Zr-40at%Cu-10at%Al alloy deformed by 100 rotations of HPT.

The XRD patterns in Fig. 4.6(a) reveals the evolution of the microstructure with increasing number of rotations (N). The fully crystallized undeformed sample mainly consisted of five phases, namely Zr_2Cu, τ_5, ZrCu with B2 structure and two martensite phases (Cm and B19'). The sharp crystalline peaks gradually weaken and broaden with increasing number of rotations of HPT deformation, which indicates significant grain refinement. After 10 rotations, a broad halo peak at $2\theta \approx 38°$ can be seen, suggesting the formation of an

amorphous phase. On Increasing the HPT deformation to higher numbers of rotations, the peak intensity decreases more significantly and the relative intensity of the halo becomes higher as the volume fraction of the amorphous phase increases. There is not much further change in the XRD pattern for after 50 rotations. Two small peaks corresponding to τ_5 phase still remain even after 100 rotations, indicating achieving a complete SSA seems impossible in this intermetallic system by HPT. The peak positions of the halo in XRD patterns of the MG and the sample deformed to N = 100 are almost the same, similar to the observation in $Ni_{40}Ti_{60}$ amorphous alloys made by liquid-quenching and mechanical alloying [128]. TEM observation (Fig. 4.2(b)) shows that after 100 rotations small crystals in the size of tens of nm are embedded in the amorphous matrix. The lattice structure of the remaining τ_5 phase can also be seen in the bright-field TEM image with a higher resolution (Fig. 4.6). The fringe spacings of 4.19 and 2.61 Å are close to the (111) and $(2\bar{2}0)$ interplanar distances of the τ_5 phase, respectively.

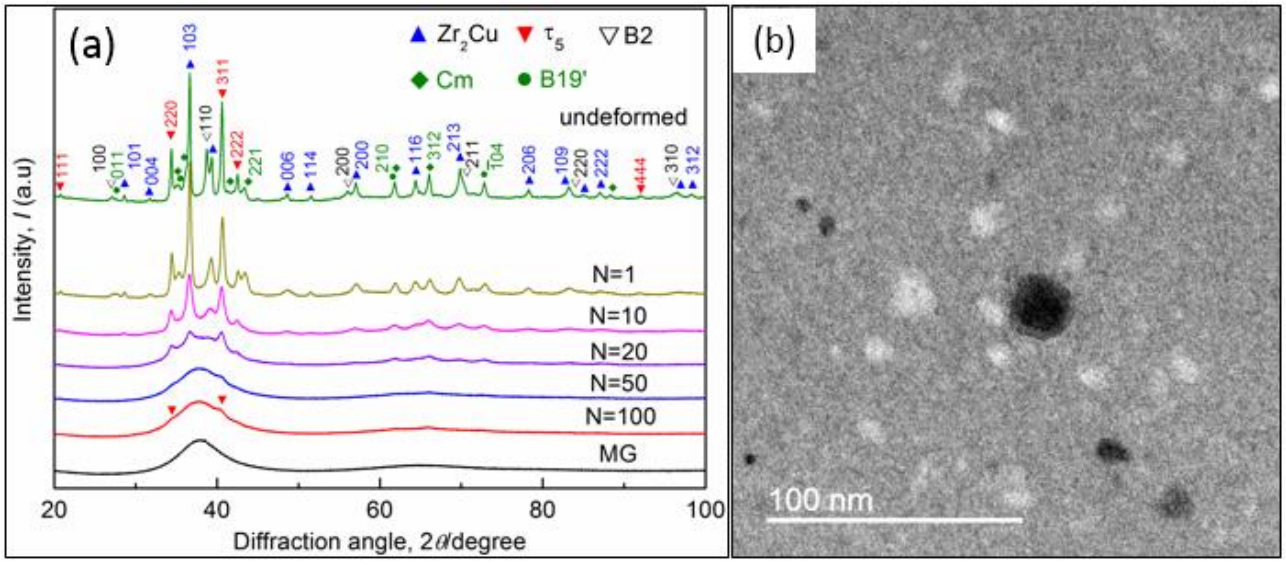

Fig. 4.5. (a) XRD patterns of Zr-40at%Cu-10at%Al alloy in different states: undeformed, HPT-deformed at various rotations (N), and as-cast metallic glass (MG). (b) TEM bright field image of the N = 100 sample.

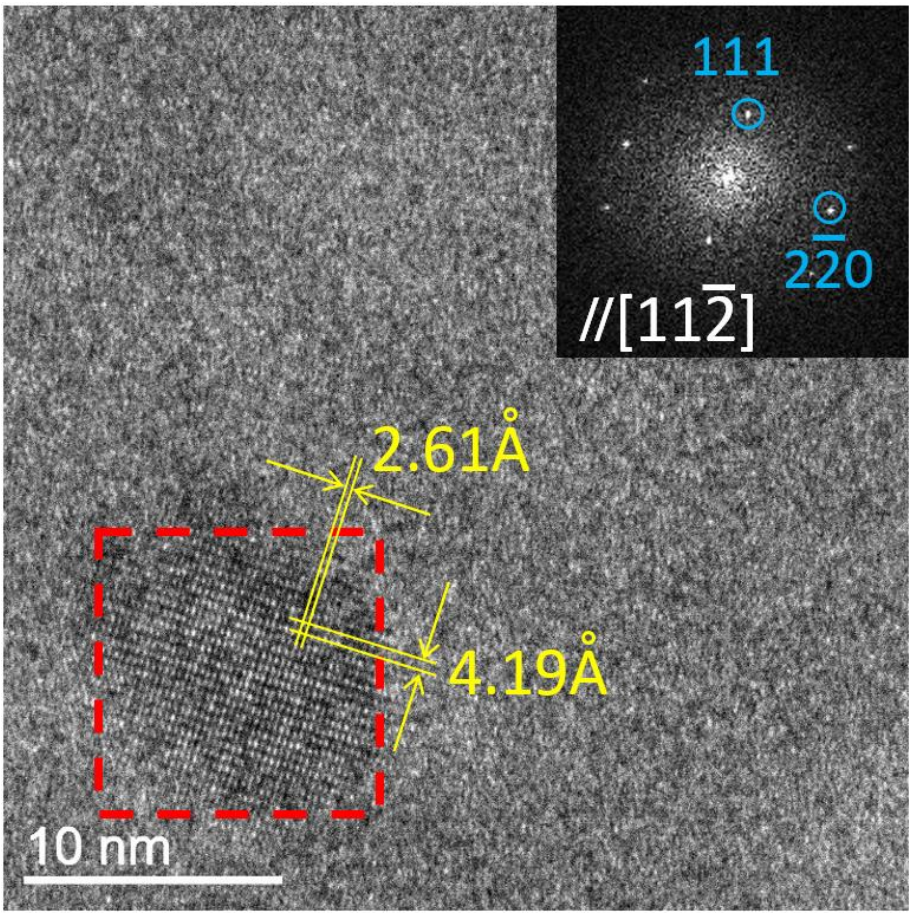

Fig. 4.6. Bright-field TEM image showing the lattice structure of the residual τ_5 phase in the amorphous matrix for the Zr-40at%Cu-10at%Al alloy deformed by 100 rotations of HPT. The inset shows the fast Fourier transformation of the area encircled by the red dash line.

The volume fraction of each phase was roughly estimated from the XRD patterns as the ratio between the I_i and I_{total}, where I_i is the integral intensity of each specific phase and I_{total} is the sum of the integral intensity of all the phases, this algorithm has been used to calculate the relative volume fraction of the amorphous phase [136, 137]. Fig. 4.7 shows that the volume fraction of the amorphous phase on the median plane increases with rotation number, but such increase was slower for higher rotation numbers. The insets are the Gaussian-fit curves of the XRD patterns for undeformed and N = 100 samples. Using this method, the relative volume fracture of the constituent phases in the undeformed samples τ_5, martensite phases, B2 and Zr_2Cu is estimated to be 34%, 30%, 14% and 22%, respectively. The normalized volume fraction of these phases at different rotation numbers is presented in Fig. 4.8. It shows that B2 and martensite phases were amorphized preferentially. Taking into account the chemical composition of each phase, this results suggest that chemical disordering could play a major role in SSA [9].

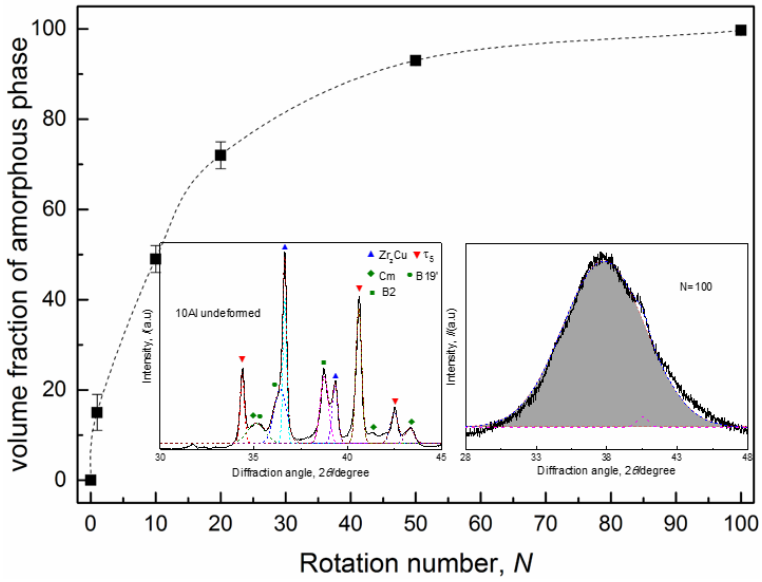

Fig. 4.7. Estimated volume fraction of the amorphous phase on the median plane. The insets show the Gaussian fit of the XRD patterns for the undeformed and N = 100 samples.

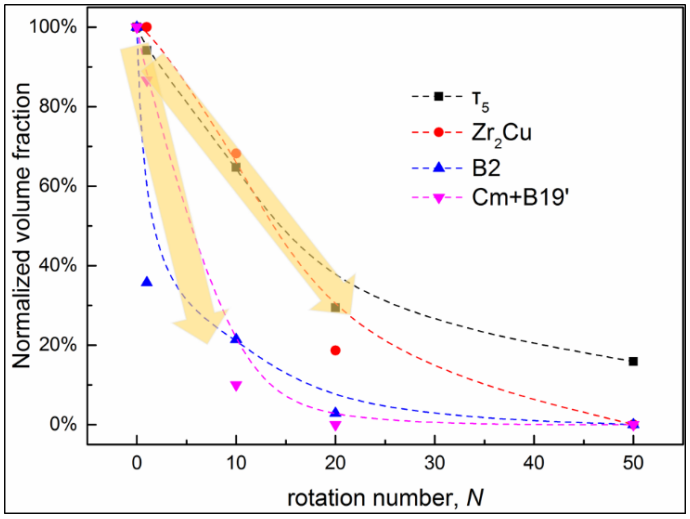

Fig. 4.8. Normalized volume fractions of the constituent phases at different N.

The existence of nanocrystals τ_5 can deviate the nominal composition of the HPT-amorphized phase to that of the $Zr_{50}Cu_{40}Al_{10}$ MG. To (semi-)quantitatively examine this idea, EDS analysis was conducted in the STEM mode using a JEOL 2100F microscope. Fig. 4.9 shows the STEM image of the sample deformed by N = 100. It can be seen that Cu and Zr were uniformly distributed throughout the sample, whereas Al was segregated in some local regions (encircled by the white dash line).

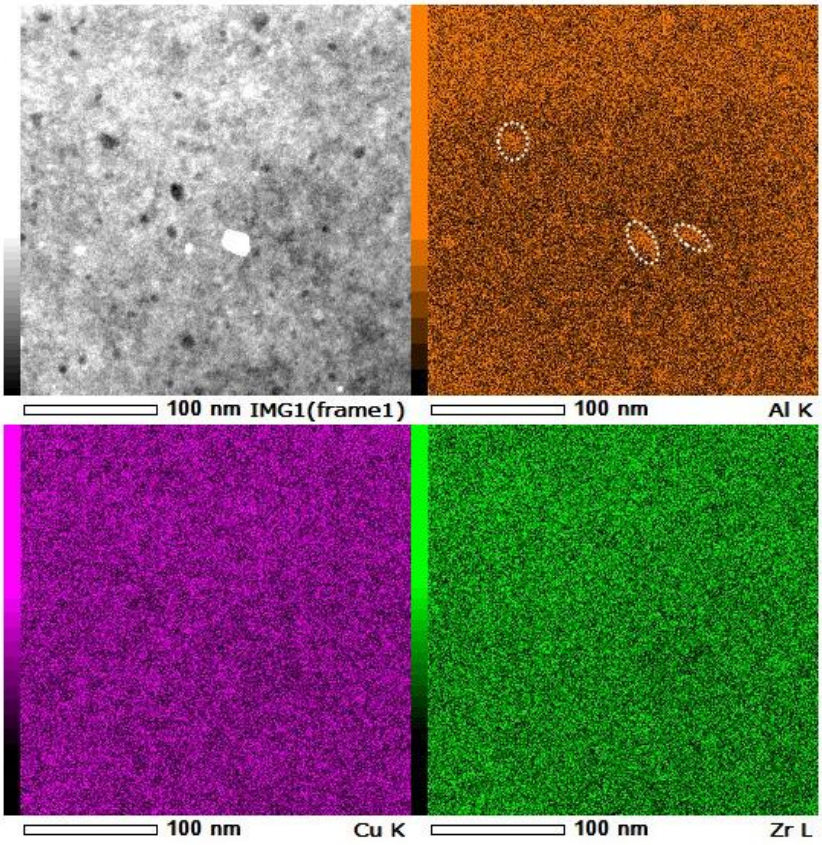

Fig. 4.9. STEM image (camera length = 20 mm) of the Zr-40at%Cu-10at%Al alloy deformed by 100 rotations of HPT, together with the mappings of elemental distribution.

4.3 Evolution of thermal and mechanical properties: evidence for concurrent rejuvenation during solid-state amorphization

4.3.1 Thermal analysis

HPT-induced grain refinement and amorphization have a large impact on the thermal and mechanical properties of the undeformed sample. Fig. 4.10 shows the DSC curves of the undeformed and HPT-deformed samples. For the undeformed sample, only the endothermic signal corresponding to reverse martensitic transformation can be detected (inset of Fig. 4.10). However, such transformation cannot be observed after one rotation of HPT deformation. The fluctuations around 750 K might be caused by the annihilation of a large amount of lattice defects [47]. After 10 and more rotations, obvious exothermic flow begins to appear, which could be ascribed to the crystallization of the HPT-induced amorphous phase. The onset temperature of crystallization (T_x) gradually increases with rotation numbers, and for the N = 100 sample, an obvious glass transition prior to T_x can also be seen. In addition, there existed an exothermic reaction in the broad temperature range from around 370 K for the N = 20, 50 and 100 HPT-deformed samples. This may be due to structural

relaxation of the amorphous phase, suggesting that the amorphous phase formed by HPT is structurally rejuvenated [37]. This point will be discussed later in more details.

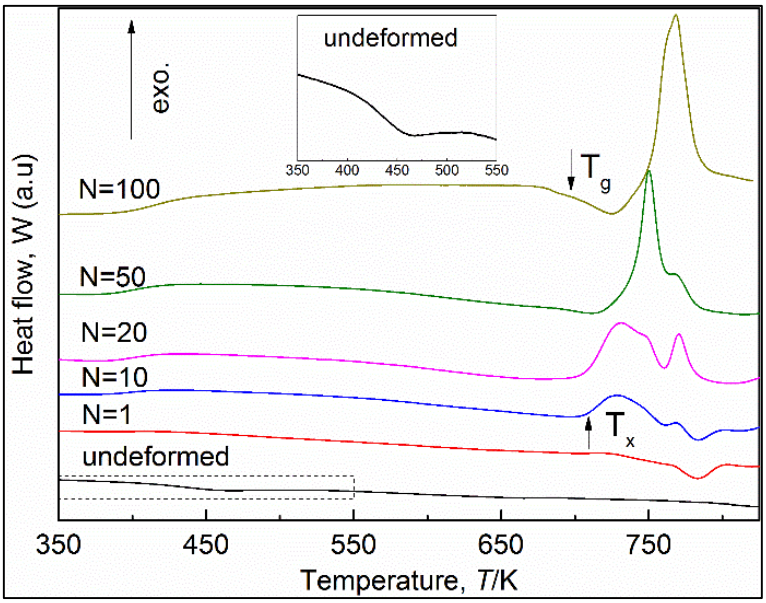

Fig. 4.10. DSC curves of samples deformed by various rotations (*N*) of HPT.

For the calculation of relaxation enthalpy (ΔH_{rel}), all samples were heated twice. The first run was from room temperature to the end of relaxation. The second run was conducted on the same sample from room temperature to above T_x. The existence of nanocrystals τ_5 can deviate the nominal composition of the HPT-amorphized phase to that of the MG. Nonetheless, the glass transition of the MG and N = 50 and 100 samples commence at approximately the same temperature (Fig 4.11). T_x of the MG is higher than that of the HPT-deformed samples by ~42 K, leading to a wider supercooled liquid region. This could be attributed to the existence of residual τ_5 crystals acting as heterogeneous nucleation sites. The relaxation enthalpy (ΔH_{rel}) of the MG (~160 J/mol) is much smaller than that of the N = 20 (~ 770 J/mol), N = 50 (~ 1950 J/mol) and N = 100 (~2450 J/mol) HPT-deformed samples.

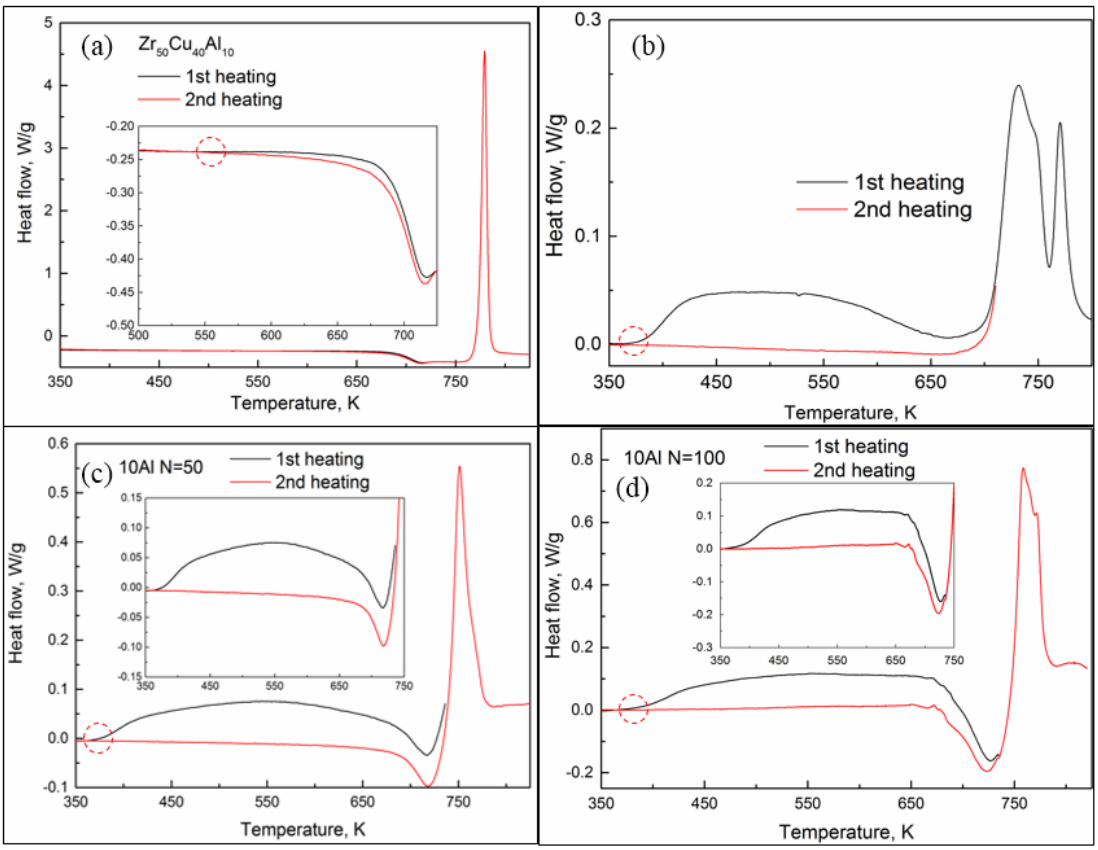

Fig. 4.11. DSC curves of the MG, N = 20, 50 and 100 samples for the calculation of relaxation enthalpy (ΔH_{rel}). The onset temperature of relaxation is encircled by the red dash line.

4.3.2 Vickers indent and nanoindentation

HPT-induced grain refinement and amorphization also have a large impact on the hardness. Fig. 4.12(a) shows plots of the Vickers hardness measured on the cross-section of the disks as a function of distance from the disk center. One rotation of HPT deformation leads to significant grain refinement, which results in an increase in hardness from 440 ±7 H_v in the undeformed state to 544 ±12 H_v. The sample hardness in the case of N = 10 is at the level of N = 1, which could be attributed to the formation of the amorphous phase and further grain refinement that have opposite contributions to hardness. Increasing the rotation number beyond 10 leads to further reduction in hardness. Specifically, the hardness of the sample deformed to N = 100 is even smaller than that of the MG. Considering that there are residual τ_5 crystals in the N = 100 sample acting as a strengthening phase, the real hardness value of this sample should be much smaller than the MG. Furthermore, shear bands can be observed around the indent of the MG (Fig. 4.12(b)), whereas the sample amorphized by N = 100 HPT exhibits smooth morphology that is similar to a rejuvenated MG in the previous chapter.

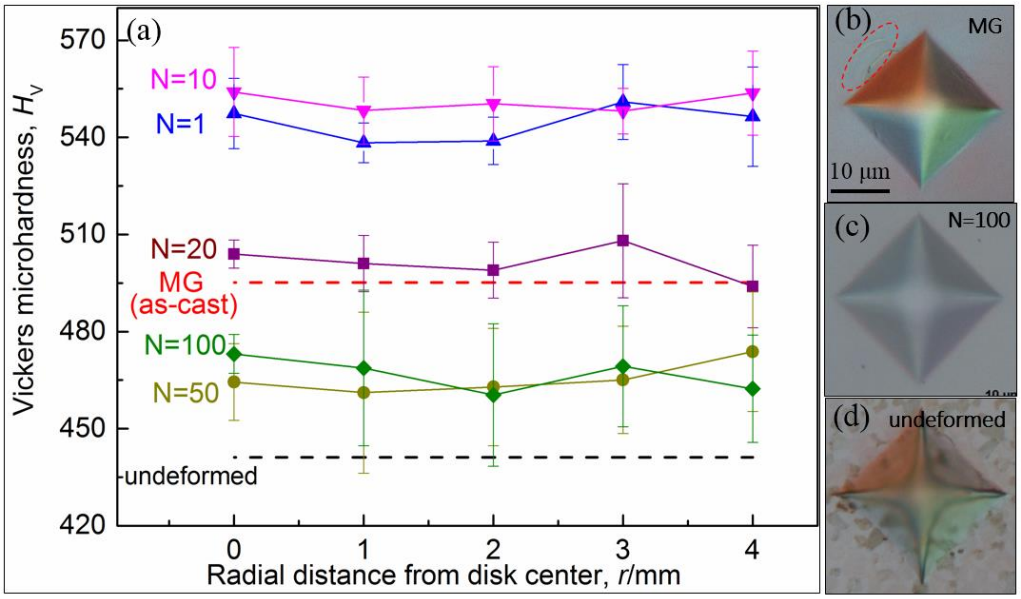

Fig. 4.12. (a) Vickers hardness on the cross-section as a function of distance from the disk center for the MG and HPT-deformed samples. (b) - (d) optical images of the indents.

For a better comparison of the mechanical properties, nanoindentation was performed. Fig. 4.13(a) shows the load-depth curves of the undeformed sample indented on different phases. The modulus (*E*) and hardness (*H*) for τ_5, ZrCu and Zr_2Cu are 147.1±7.0 GPa and 12.56±0.71 GPa, 110.5±4.3 GPa and 6.51±0.15 GPa, 132.6±6.0 GPa and 8.53±0.26 GPa, respectively. The phases with the composition of ZrCu (B2 and two martensite phases) have the lowest hardness value, which may be another reason for their propensity to SSA as seen in Fig. 4.6. On the other hand, the τ_5 phase having the largest hardness may explain why it is the last phase remained in the amorphous matrix. Nanoindentation tests were also conducted on the HPT-deformed samples as well as on the MG as a comparison. Fig. 4.14(a) shows the representative load-depth curves. Pop-in in the loading curve is observed for MG, which could be related to discrete bursts of plastic deformation [37]. However, there is no pronounced pop-in for the *N* = 50 and 100 sample, suggesting that the deformation mode is more homogeneous. The scanning probe microscopy (SPM) images (Fig. 4.14(b) and (c)) of the indents exhibit the difference in deformation mode as well. Pile-ups appear around the indent in the MG sample, whereas no pile-up can be seen for the *N* = 100 sample. The *E* and *H* of the MG are 104.1±1.8 GPa and 7.34±0.18 GPa, respectively. In comparison, the *N* = 100 sample exhibits lower *E* and *H* (97.4±1.6 GPa and 6.30±0.12 GPa, respectively). The absence of pop-ins and shear bands as well as the reduced *E* and *H* in the *N*=100 sample resembled those in the HPT-deformed $Zr_{50}Cu_{40}Al_{10}$ MG [37], suggesting that SSA by HPT led to the formation of a structurally-rejuvenated amorphous phase. Fig. 4.15 plot the bar chart of the *E* and *H* of

the HPT-deformed samples as a function of *N*.

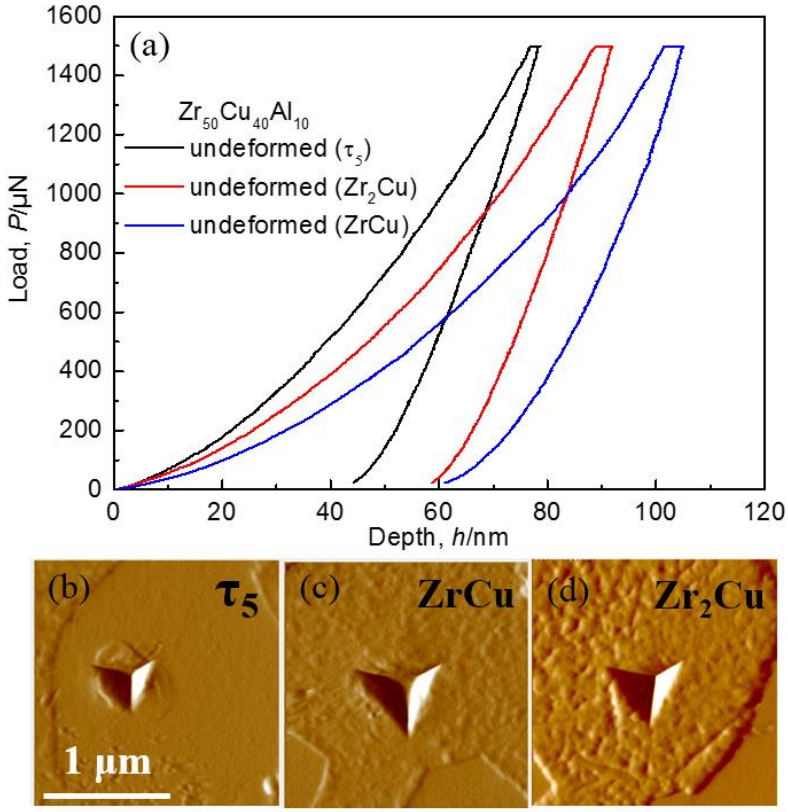

Fig. 4.13. (a) Load-depth curves performed on different constituent phases of the undeformed Zr-40at%Cu-10at%Al alloy. (b)~(d) are the corresponding SPM images of the indents.

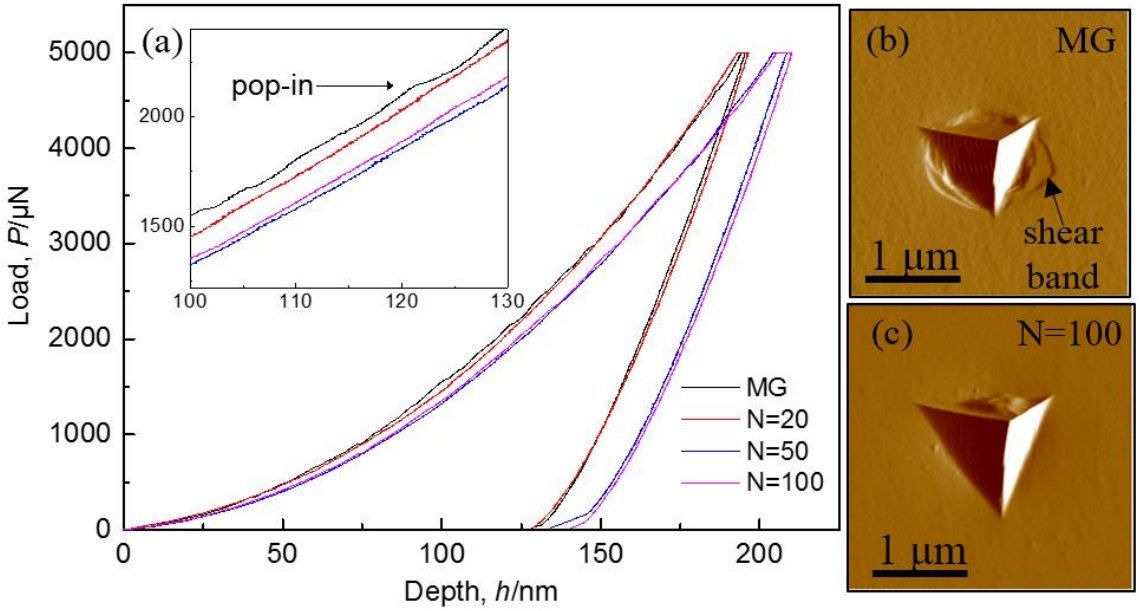

Fig. 4.14. (a) Nanoindentation load-depth curves of the MG and HPT-deformed samples. The corresponding SPM images of the indents for the MG and *N* = 100 samples are shown in (b) and (c).

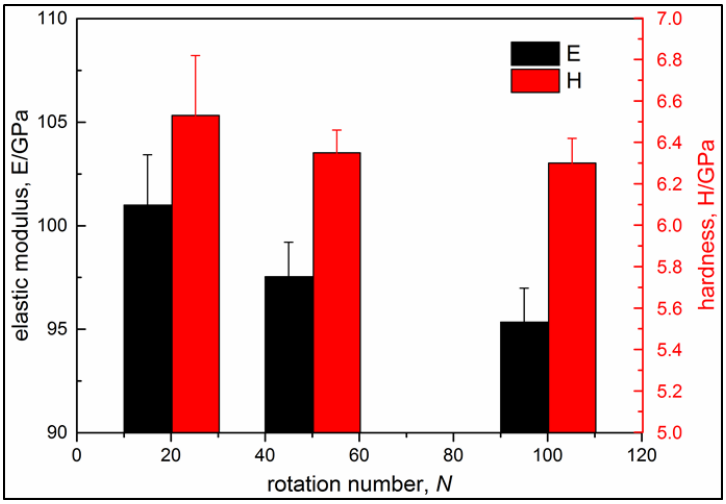

Fig. 4.15. Elastic modulus (*E*) and hardness (*H*) values as a function of *N*.

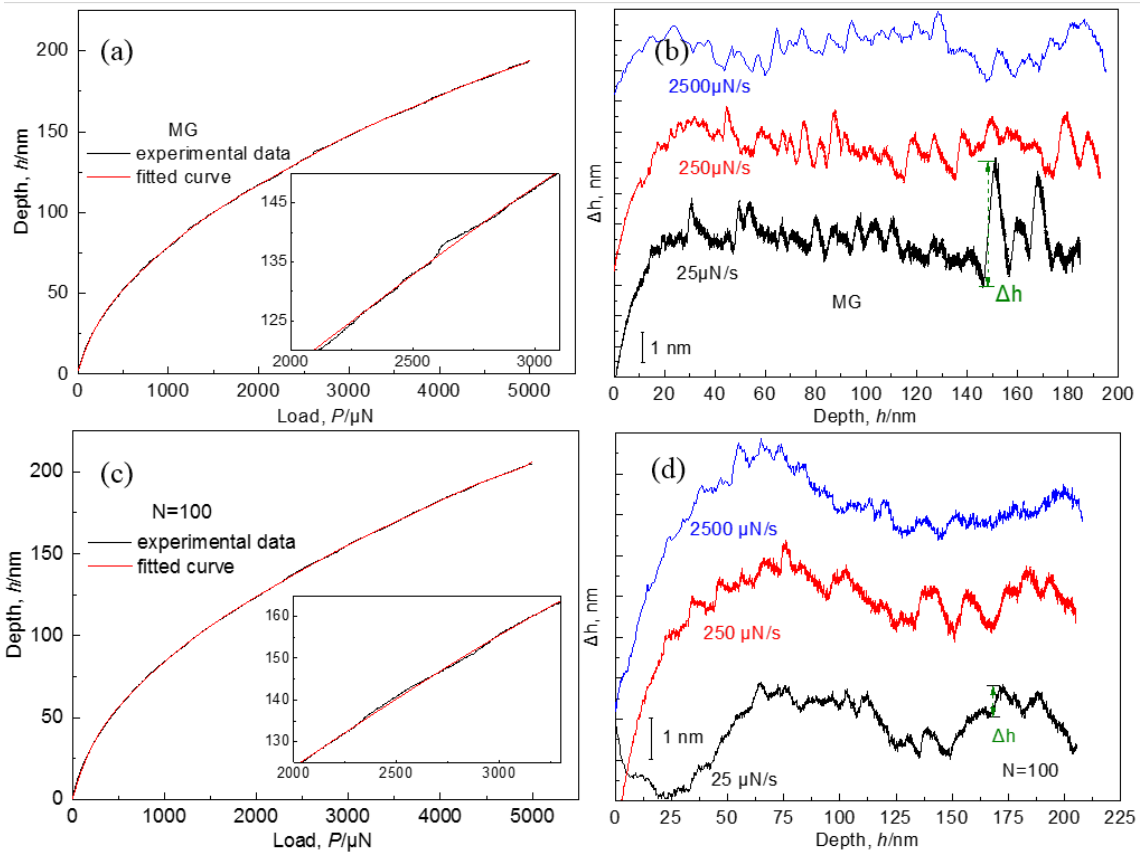

Fig. 4.16. Representative polynomial function fitting curves of the depth-load for the loading part of (a) MG and (c) $N = 100$ samples, with the correlation between Δh and h of cold-rolled (b) MG and (d) $N = 100$ samples showing the serration events.

4.3.3 Discussion

4.3.3.1 Cut-off value of strain burst size

It is evident from the number and magnitude of pop-in in the loading curves that the MG exhibits larger strain bursts than the N = 100 sample. To further confirm this observation, we conducted a quantitative analysis of the distribution of strain burst size as detailed in ref. [138] and [139]. To put it simply, the loading curve is first fitted to a polynomial function to get the baseline (Fig. 4.16(a) and (c)). After baseline subtraction, the pop-in events as a function of indentation depth (h) becomes fairly obvious (Fig. 4.16(b) and (d)). The depth change (Δh) of each pop-in is then normalized to h, which reveals strain burst size ($S = \Delta h/h$). Fig. 4.17 shows the cumulative probability distributions of S, *i.e.*, the percentage of the number of pop-in events with S being larger than a given value P ($>S$) of the MG and N = 100 samples. For both samples, smaller strain bursts seem to be more probable. With the increase of S, the probability distributions exhibit a drastic decrease. The change of P ($>S$) as a function of S can be fitted by an empirical relation [138, 139]:

$$P(>S) = AS^{-\beta}\exp(-S/S_c) \tag{4.1}$$

where A is a normalization constant, β is a scaling exponent, and S_c is the cut-off value of S. Although the MG and N = 100 sample possess similar values of β (~0.18), the S_c of the MG (0.009 ± 0.003) is larger than that of the N = 100 sample (0.005 ± 0.001). It is worth mentioning that both β and S_c of these two samples are on the same order of magnitude as that of a typical Zr-based MG $Zr_{41.25}Ti_{13.75}Ni_{10}Cu_{12.5}Be_{22.5}$ [138]. Generally, S_c corresponds to a critical shear avalanche size that can be regarded as the deformation unit (DU) size [139]. These rigidly packed DUs would move in concordance during deformation. A smaller DU suggests that fewer atoms are needed to initiate a collective motion, which gives rise to smaller internal stress concentration [138]. Therefore, a smaller S_c could lead to an easier dissipation of external strain into the matrix under indentation [139], which could correspond to an easier generation of the STZs. The absence of shear avalanche (a small S_c) can contribute to the continuous generation of multiple shear deformed areas and a more homogeneous deformation mode during plastic deformation, which was reflected in the disappearance of pop-in and pile-up as observed in the N = 100 sample (Fig. 4.12(c)).

4.3.3.2 Sub-T_g and near-T_g annealing of the amorphized sample

In an earlier study, Meng *et al*. demonstrated that both E and H of an MG decreased with increasing ΔH_{rel}, and thereby attributed this phenomenon to a large amount of rejuvenated structure [37]. In order to clarify whether this tendency can hold true in the HPT-amorphized samples, isochronal heating was conducted on the N = 100 sample to several different annealing temperatures (T_{anneal}), which are 393 K (T_g-300 K), 538 K (T_g-

155 K) and 713 K (T_g+20 K). Fig. 4.18(a) shows the load-depth curve of these annealed samples, together with the SPM images of the indents (Fig. 4.18(b)-(e)). With the increase of T_{anneal}, the localized deformation was gradually restored and pile-up as well as pop-in started to re-appear. Such a reversible transformation of the deformation mode has been reported in an MG rejuvenated by HPT. Fig. 4.19 shows plots of the changes of E and H of the annealed samples as a function of ΔH_{rel}, together with the data from ref. [37] that corresponds to the as-cast MG samples deformed by HPT. For the N = 100 HPT-deformed sample, both E and H decrease gradually with increasing ΔH_{rel}. However, compared to MG samples with the same ΔH_{rel}, the HPT-amorphized samples tends to show higher E and H, which could be ascribed to the incomplete amorphization where the residual crystals act as a strengthening phase.

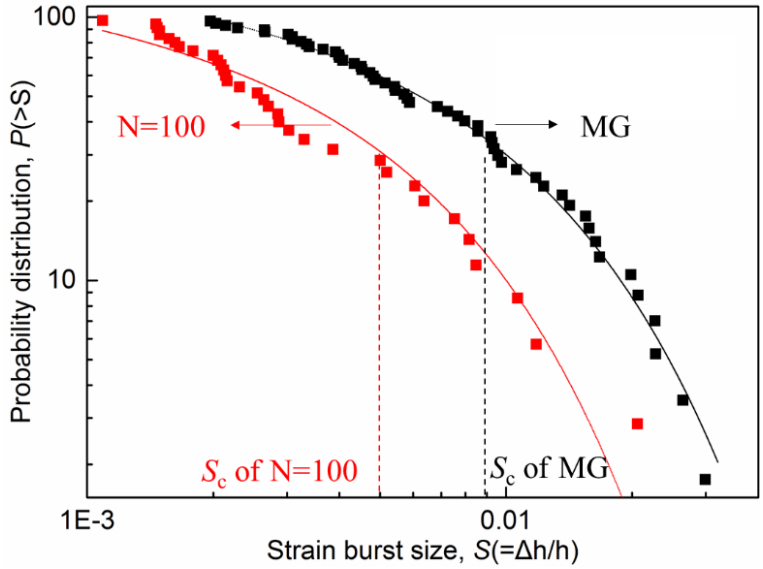

Fig. 4.17. Cumulative probability distributions of strain burst size of MG and N = 100 HPT-deformed samples.

4.3.3.3 Probable reasons for large heat release

The HPT-amorphized N = 50 and N = 100 samples exhibit exceptionally large ΔH_{rel} compared to MG samples subjected to HPT in ref. [37]. Specifically in the condition of deformation by 50 rotations, the ΔH_{rel} for the rejuvenated MG sample is ~1720 J/mol, smaller than that of the HPT-amorphized sample (~1950 J/mol). One may argue that such a large ΔH_{rel} should not be solely attributed to the structural relaxation. Therefore, other possible factors were considered.

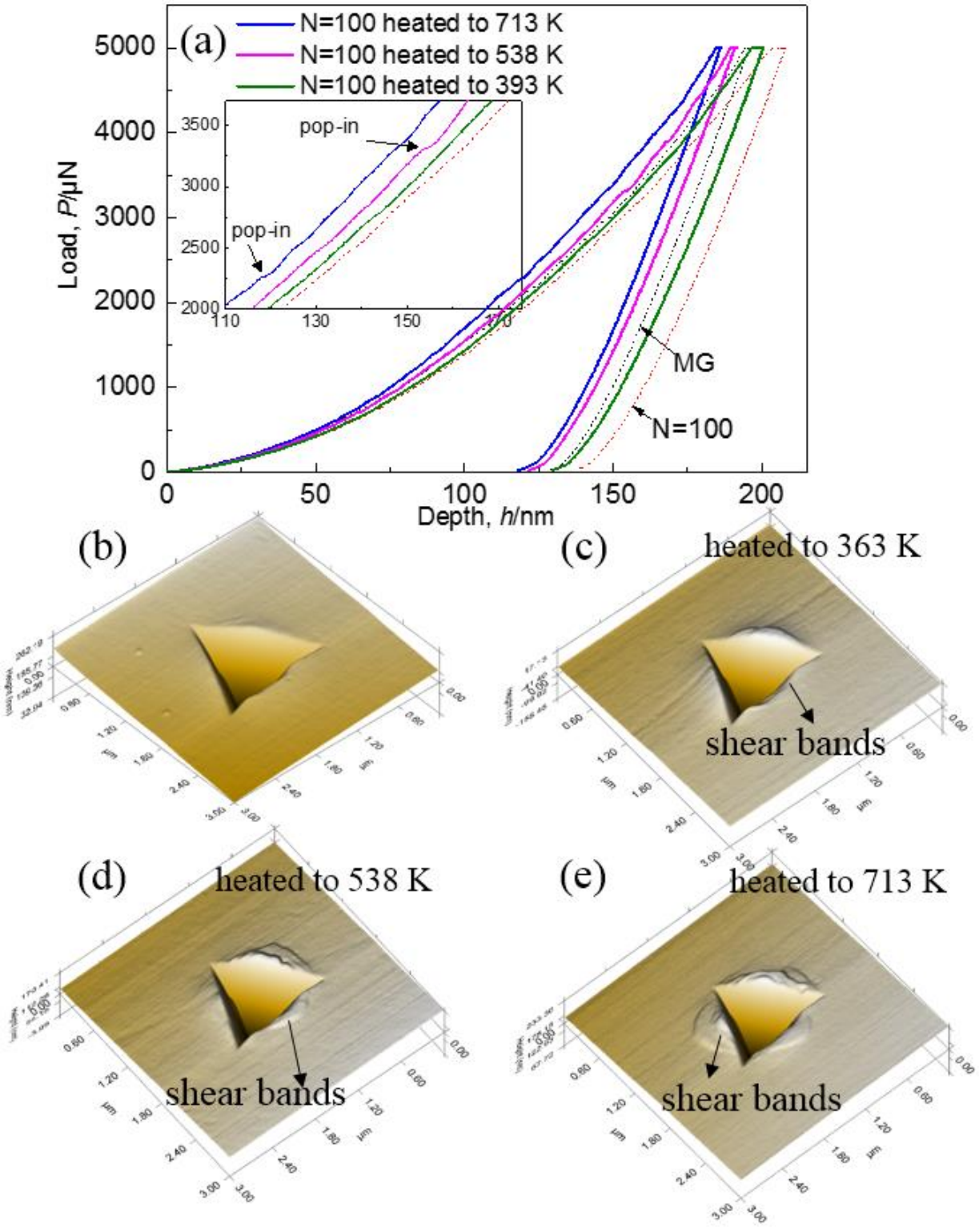

Fig. 4.18. (a) Load-depth curve of these annealed samples. (b)-(d) SPM images of the indents for the undeformed sample and the samples heated to 363 K, 538 K and 713 K in the DSC furnace, respectively.

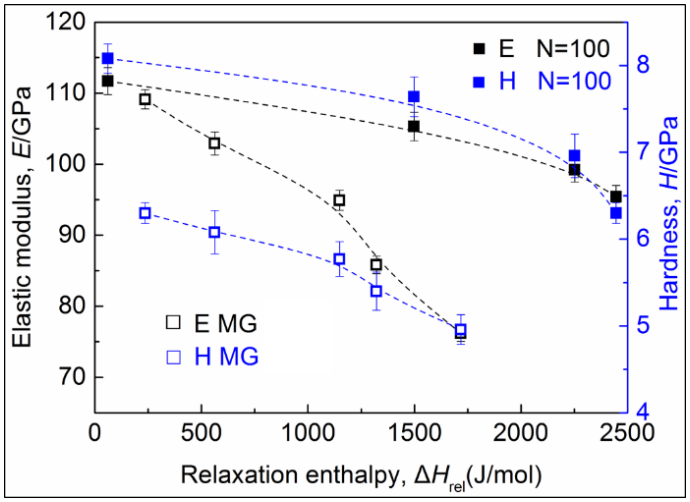

Fig. 4.19. E and H of the $N = 100$ and MG samples as a function of ΔH_{rel}.

First, it is generally believed that solid-state amorphization through mechanical means is achieved by the accumulation of lattice defects [127, 140]. The recovery of these defects can lead to enthalpy release upon heating. However, this may not be applied here as the remaining crystals in few. Second, one may assume that the residual stress could have a significant influence on the heat release. Haruyama *et al*. proposed that the residual stress energy per unit volume (E_{rs}) can be evaluated by:

$$E_{rs} = \sigma_{rs}\varepsilon_{app} / 2 \tag{4.2}$$

where σ_{rs} is the residual stress and ε_{app} the apparent strain [83]. However, using their method (taking $\sigma_{rs} \approx 0.5$ GPa [141], $\varepsilon_{app} \approx 1\%$; $\rho = 7\times10^6$ g/m^3), the E_{rs} is only approximately 20 J/mol, amounting to only ~1% of the overall ΔH_{rel}. Third, Lu *et al*. proposed that grain growth may contribute to ΔH_{rel} following the equation [142]:

$$\Delta H = \frac{1}{\rho}\gamma\left(\frac{1}{d} - \frac{1}{d_0}\right) \tag{4.3}$$

where ρ is the density, γ is the interfacial energy, d and d_0 denote the grain size after and before growth, respectively. However, in-situ TEM observation with a heating holder (Fig. 4.20, with a heating rate of 40 K/min) in the sub-T_g regime did not show any noticeable grain growth (compared to Fig. 4.5(b)). Lastly, possible chemical relaxation (elemental segregation) and the start of grain growth can also contribute to the observed large ΔH_{rel}, as was suggested by Hentschel *et al*. in electroless plated Ni-3.6%P layers [143].

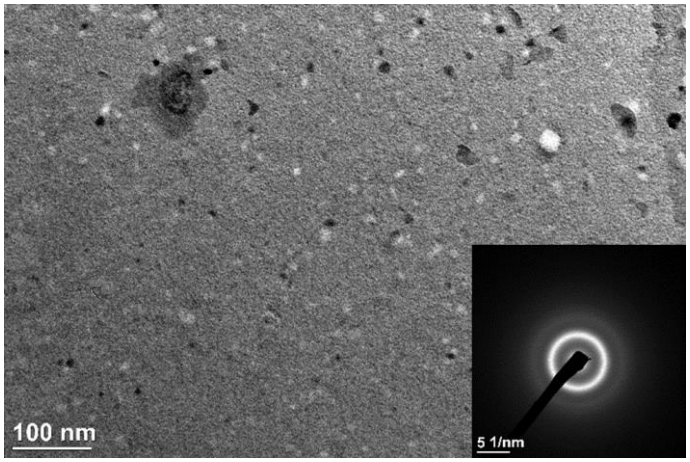

Fig. 4.20. Bright-field TEM image of the N = 100 HPT-deformed sample heated to 733 K using a heating holder. The inset is the corresponding diffraction pattern.

Besides the overall heat release, the relaxation spectrum is also different. Specifically, the onset temperature of structural relaxation of the MG sample (~0.8T_g) is higher than that of the N = 100 sample (~0.55T_g), suggesting an enhanced β relaxation [36]. Moreover, unlike the MG whose relaxation ends at ~T_g, the relaxation of the N = 100 sample seems to extend to ~T_x. This is likely to be caused by chemical relaxation where the nanocrystals equilibrate with the remaining amorphous phase that would later initiate an abrupt onset of nucleation [144].

Last but not least, a lower onset relaxation temperature and a higher relaxation enthalpy (Fig. 4.11), the decrease in Vickers microhardness (Fig. 4.12), and the absence of pop-in in loading curve and semi-arc steps in nanoindentation tests (Fig. 4.14), all suggest that compared to the amorphous phase obtained by MQ, the amorphous phase obtained by SSA has extensively rejuvenated structure.

4.3.3.4 Formation of SROs during melt-quenching and SSA

Ding *et al*. studied the structural changes during the liquid-to-glass process from the perspective of polyhedral clusters and potential energy landscape [110]. They pointed out that the clusters with a lower potential energy (clusters with a Voronoi index of <0, 0, 12, 0> for $Cu_{64}Zr_{36}$ and <0, 3, 6, 0> for $Pd_{82}Si_{18}$, respectively) would increase at a comparatively high rate upon cooling (Fig. 4.21), thus lowering the overall energy of the system. In contrast, there is little information in the literature regarding the formation of the polyhedral clusters during SSA. This leads to the assumption that the type and fraction of SROs in the solid-state amorphized structure is more arbitrary and random. In other words, different clusters with different potential energies would form without preference.

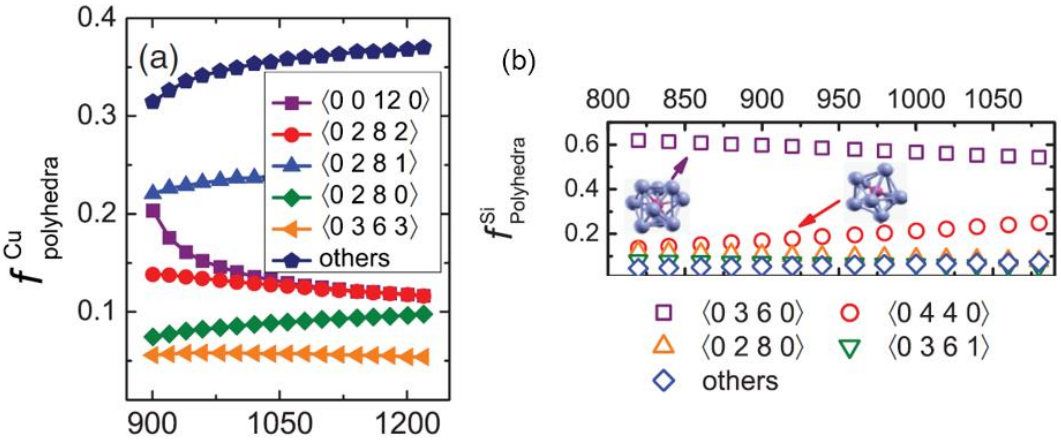

Fig. 4.21. Fractions of different polyhedral clusters as a function of the temperature during melt-quenching for (a) $Cu_{64}Zr_{36}$ and (b) $Pd_{82}Si_{18}$ glass-forming liquids [110].

4.4 Solid-State amorphization by high-pressure torsion using different rotation speeds

As introduced earlier, solid-state amorphicity can be inherited from the liquid by rapid quenching the melt where crystallization is avoided. On the other hand, amorphous alloys can also be obtained by introducing massive lattice defects to their crystalline counterparts [127, 140]. Generally, it is necessary to increase the concentration of lattice defects to a certain level such that the Gibbs free energy of the defected crystal exceeds that of the corresponding amorphous phase [127, 140]. For example, Nagase *et al*. reported that a critical dosage is required for irradiation-induced solid-state amorphization (SSA) in Ti-Ni-Fe alloys [2]. Sun *et al*. also suggested that there exists a critical strain for SSA induced by HPT [145]. The previous section also suggests that increase the rotation number could lead to further SSA. Nonetheless, neither a critical dosage nor a critical strain equates a critical concentration of lattice defect. Therefore, when it comes to a specific fabrication method, SSA depends certainly yet obscurely on the processing conditions.

Speaking of HPT, the extent of SSA is largely dependent on the processing parameters such as rotation number [7, 47, 133, 145] and deformation temperature [146, 147]. Although the influence of deformation temperature remains conflicting, it seems clear that increasing the rotation number would almost certainly lead to an increase in the volume fraction of the amorphous phase [7, 47, 133]. However, most studied were conducted using a constant rotation speed of the movable anvil; and little is known about the influence of the rotation speed. In this present study, 50 rotations of HPT was performed in the same starting material used in the previous section (crystalline $Zr_{50}Cu_{40}Al_{10}$) using different rotation speeds. The results show that the faster

the rotation speed, the more marked the amorphization.

The XRD patterns in Fig. 4.22 confirmed that the undeformed sample before HPT mainly consisted of five phases, namely Zr_2Cu, τ_5, ZrCu with B2 structure and two martensite phases (Cm and B19'). Deforming to 50 rotations at the anvil rotation speed of 0.2 rpm led to slight peak broadening, which suggested grain refinement by severe plastic deformation. Such phenomenon became more pronounced with increasing rotation speed. For the samples deformed at 0.5 and 1 rpm, an obvious broad halo peak corresponding to an amorphous phase can also be seen at $2\theta \approx 38°$. For the samples deformed at 0.2 and 0.5 rpm, all phases existed in the undeformed sample can be identified. In contrast, only the peaks corresponding to τ_5 can be observed superimposed on the broad halo peak.

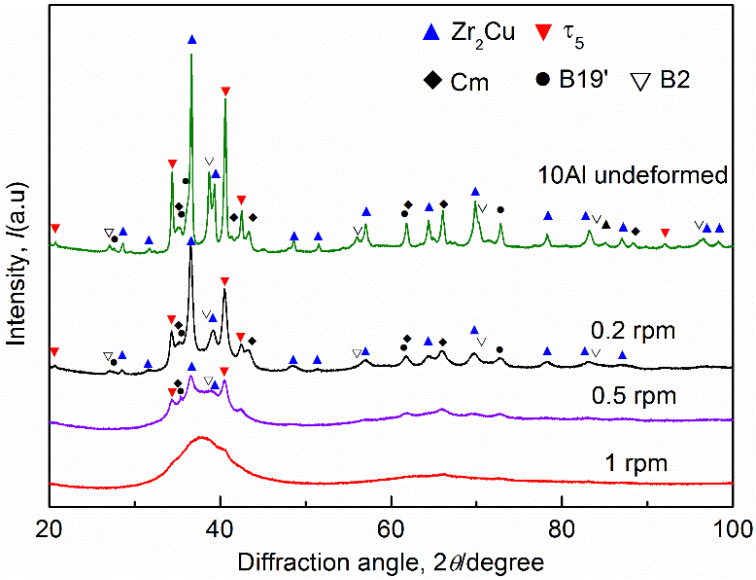

Fig. 4.22. XRD profiles of the undeformed sample and the samples deformed by 50 rotations of HPT at different rotation speeds.

Fig. 4.23 shows the DSC curves (at a heating rate of 40 K/min) of the undeformed sample and the samples deformed by 50 rotations of HPT at various anvil rotation speeds. For the undeformed sample, only a weak endothermic peak corresponding to reverse martensitic transformation can be detected at approximately 450 K. In contrast, such transformation cannot be observed for the other three samples deformed by 50 rotations of HPT. Instead, one can see the exothermic peaks corresponding to the crystallization of the HPT-induced amorphous phase and the glass transition. It should be noted that the glass transition temperatures of these three deformed samples were almost identical and the crystallization modes are alike (*i.e.* almost unimodal), indicating the obtained amorphous phases have similar compositions. For the sample deformed at 1 rpm, there

existed a broad exothermic peak in the range from ~420 K to ~700 K. This could be attributed to the structural relaxation of the amorphous phase [7]. More importantly, the crystallization enthalpy (ΔH_{cry}) increased with the rotation speed (inset of Fig. 4.20). Assuming that the volume fraction of the amorphous phase is in scale with the ΔH_{cry}, the samples deformed at 0.2 and 0.5 rpm are estimated to possess 19% and 64% amorphous phase compared to the sample deformed at 1 rpm, respectively.

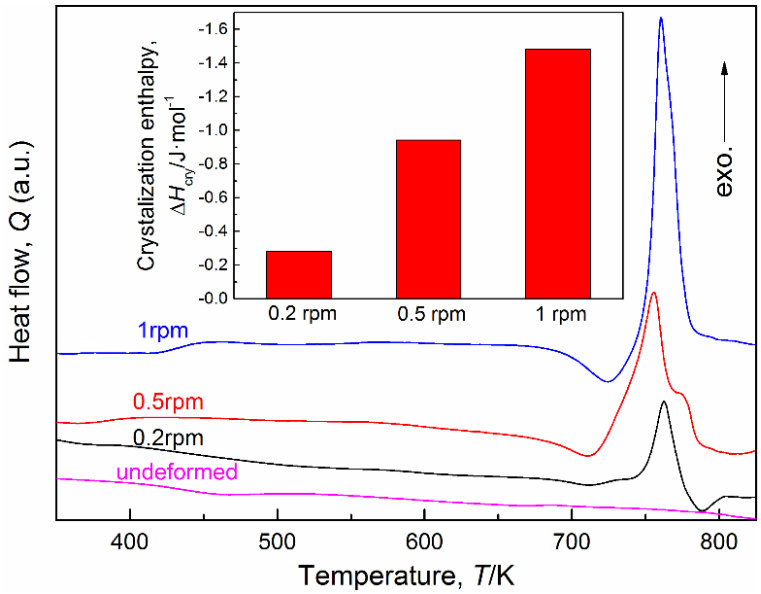

Fig. 4.23. DSC curves of the undeformed sample and the samples deformed by 50 rotations of HPT at different rotation speeds. The inset shows the bar chart of the crystallization enthalpy of the deformed samples.

The SEM backscattered electron (BSE) images in Fig. 4.24 clearly exhibit the difference in the microstructure of the samples deformed at different rotation speeds. The observation was performed at a position about 4 mm from the center of each sample. The undeformed sample (Fig. 4.24(a)) was composed of crystals in the size of several microns, and the elemental distribution was inhomogeneous. Deforming to 50 rotations at 0.2 rpm led to grain refinement and mixing of the constituent elements in certain areas, but there remained some parts where the crystals seemed slightly elongated y*et al*most intact (encircled by the red dash line in Fig. 4.24(b)). The grain refinement and mixing were more pronounced for the sample deformed at 0.5 rpm (Fig. 4.24(c)), and the intact area was significantly reduced. Deforming at 1 rpm resulted in the formation of a featureless morphology where no discernible crystals can be seen (Fig. 4.24(d)). More importantly, the elemental distribution was more homogeneous compared to the samples deformed at lower speeds. The microstructure of the sample deformed at 1 rpm can be seen more clearly using TEM. The bright-field TEM

image reveals that after 50 rotations, small crystals in the size of tens of nm are embedded in the amorphous matrix (not shown), which is similar to the one deformed by N = 100 HPT in the previous section (Fig. 4.5(b)).

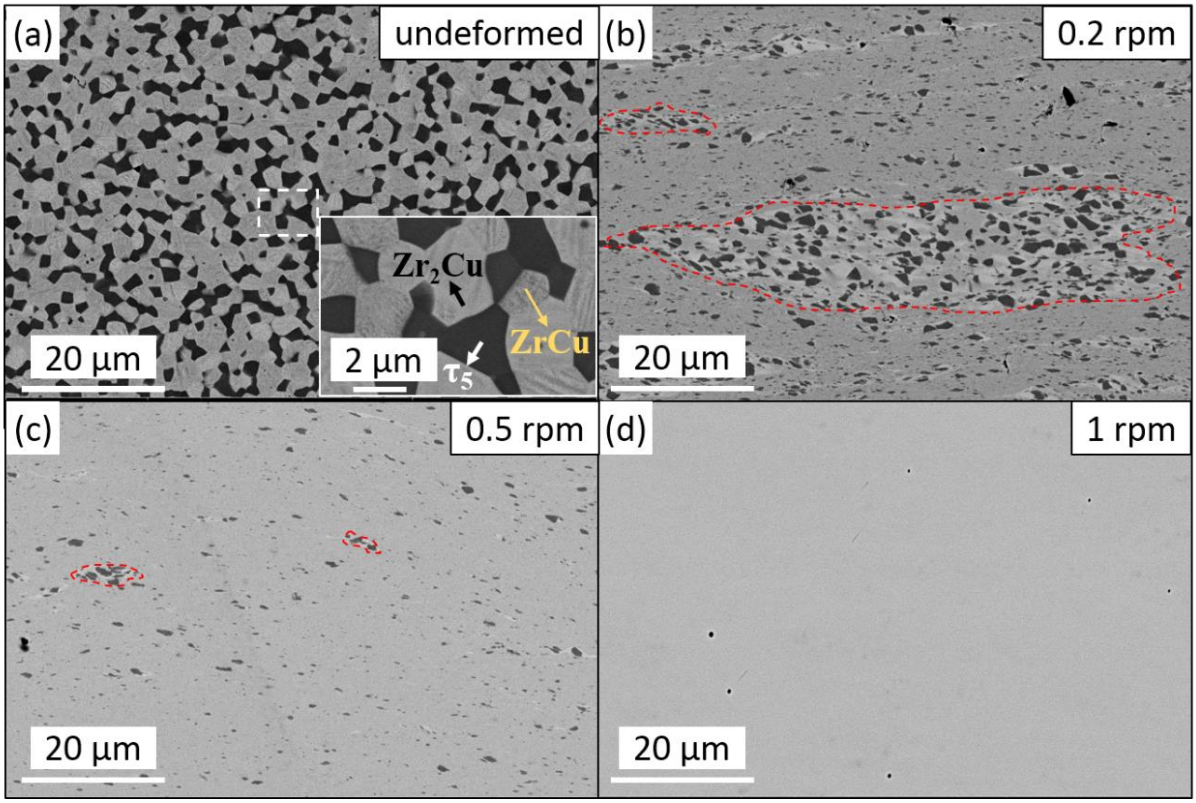

Fig. 4.24. SEM backscatter electron images of the (a) undeformed sample and (b)-(d) the samples deformed by 50 rotations of HPT at different rotation speeds.

SSA can be viewed as defect-induced melting [127]. According to the generalized Lindemann melting criterion, SSA takes place if the sum of the mean square displacement of atoms from their equilibrium positions due to lattice defects ($<\mu^2_{sta}>$) and the one related to thermal vibration ($<\mu^2_{vib}>$) reaches a critical value for melting [127]. The $<\mu^2_{sta}>$ increases with the concentration of crystalline defects, and the $<\mu^2_{vib}>$ increases with temperature. It is worth mentioning that the Lindemann melting criterion has also been used to explain glass transition, which always takes place as the most probable mean square displacement of the atoms reaches 20% of the average interatomic distance [148].

The process of SSA during HPT in the present alloy was previously studied by Meng *et al.* [7] in details. SSA proceeds in an inhomogeneous manner in the sample during HPT deformation. It often starts in shear bands where the deformation localizes and thus crystalline defect density can be extremely high even when macroscopic strain is not so high (lower N). With a higher number of N, SSA occurs in a more homogeneous

manner but it was also shown that the SSA occurs preferentially in ZrCu martensite phase with a high density of internal twins, which is the majority phase, and then extends to Zr_2Cu phase and τ_5 phase [7]. The volume of amorphous increased with the extent of deformation which is presumably due to the increase in the defect density, such as dislocations and vacancies. In addition, twins and interphase boundaries provided the preferential accumulation sites for the crystalline defects and thus can enhance SSA.

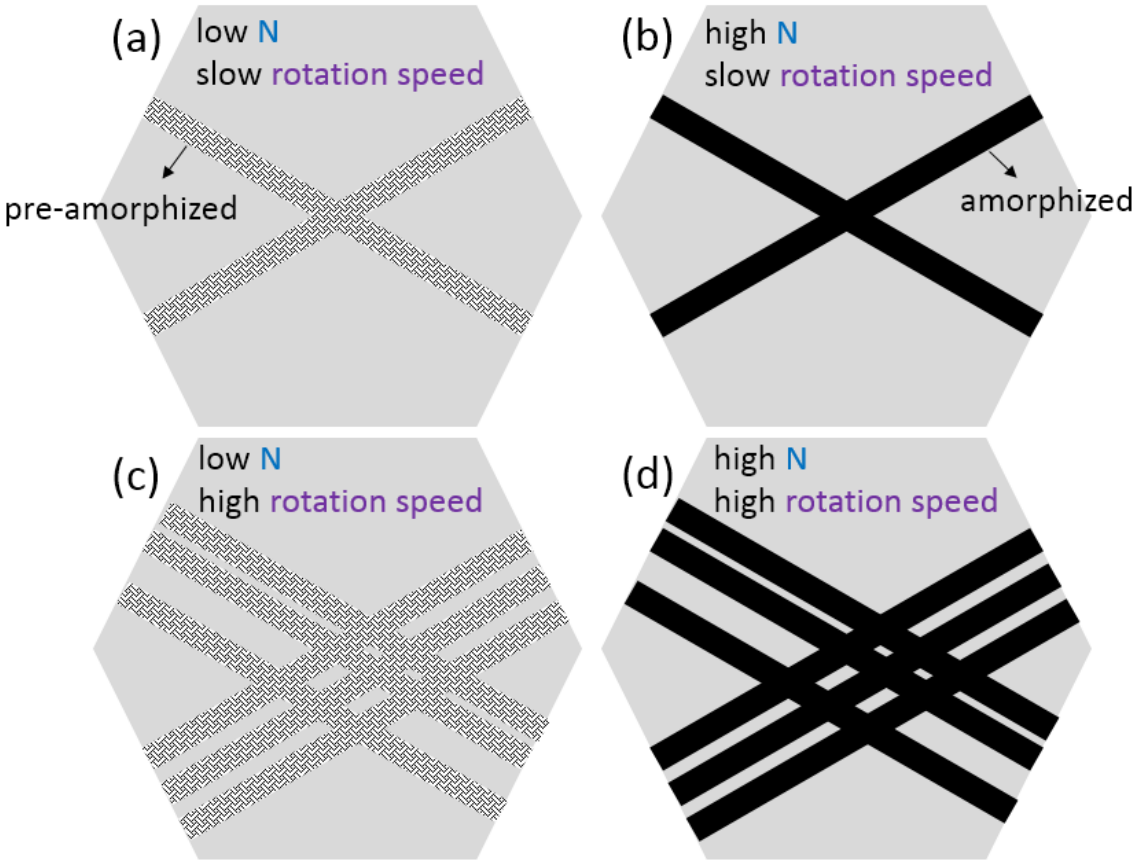

Fig. 4.25. Schematic illustrations of the process of SSA by a low rotation speed at (a) low and (b) high rotation numbers; and SSA by a high rotation speed at (c) low and (c) high rotation numbers. (The pattern in the stripes of (a) and (c) represent the mobile dislocation.)

In the present study, an increase in the anvil rotation speed led to a nearly 5-fold increase in the volume of amorphous after HPT deformation of N = 50 (inset of Fig. 4.23). Equivalent shear strain (γ) is given by $\gamma = 2\pi Nr/\sqrt{3}h$, where N is the rotation number, r the distance from the center of the sample, and h the thickness of the sample [52]. The shear strain rate ($\dot{\gamma}$) can be therefore calculated as $\dot{\gamma}=2\pi\dot{N}r/\sqrt{3}h$. The $\dot{\gamma}$ at the position 4 mm from the center for the samples deformed at 0.2 rpm, 0.5 rpm, and 1 rpm are calculated to be 5.7×10^{-2} s^{-1}, 1.4×10^{-1} s^{-1}, 2.8×10^{-1} s^{-1}, respectively. According to the Orowan relation, the $\dot{\gamma}$ is proportional to the product of the density of mobile dislocations and the dislocation velocity [149]. Also, vacancy production rate by

dislocation jogs is proportional to the strain rate [150]. Thus it is inferred that the increasing anvil rotation speed led to a local increase in the defect density which resulted in the increase in the volume of amorphous phase. In other words, there are more lattice defects in the sample as a whole. This idea is schematically illustrated in Fig. 4.25. Initially, HPT deformation leads to an increase of the local defect density (Fig. 4.25(a)). Once the defects density reaches a critical value that the Lindemann melting criterion is met, SSA would take place (Fig. 4.25(b)). A higher rotation speed of the movable anvil would increase the volume that experiences local rise of density defects (Fig. 4.25(c)), and the resulting amorphous phases obtained at different rotation speeds are qualitatively the same (low rotation speed in Fig. 4.25(b) and high rotation speed in Fig. 4.25(d)). The DSC curve of the sample deformed at 0.2 rpm resembled that of the sample deformed at 1 rpm; the glass transition and crystallization of these samples commence at approximately the same temperature. This suggests that the structure of the amorphous phase produced by SSA at different strain rates may be very similar irrespective of the rotation speed.

Another possible cause of the strain rate dependence may be the effect of temperature increase during deformation. The change in the temperature of the sample during HPT measured by the infrared camera is shown in Fig. 4.26. For the sample deformed at 0.2 rpm, the rise in temperature was trivial. On the other hand, 50 rotations of HPT at 1 rpm increased the temperature only by ~40 K. The measured temperature may only reflect the condition of the periphery of the sample and the actual temperature of the sample could be higher. Nonetheless, our results are similar to the ones obtained from finite element modeling [151] and thermo-couple measurements [152]. A temperature rise can contribute to increasing defect density either through an increase in thermal vacancies or through lowering yield stress. The amount of thermal vacancy at this temperature is far below that required to induce SSA. Since the sample composed of intermetallic phases, the temperature effect on yield stress is also negligible at this temperature range. Hence, the observed temperature increase of about 40 K may be too small to account for the 5-fold increase of amorphous volume.

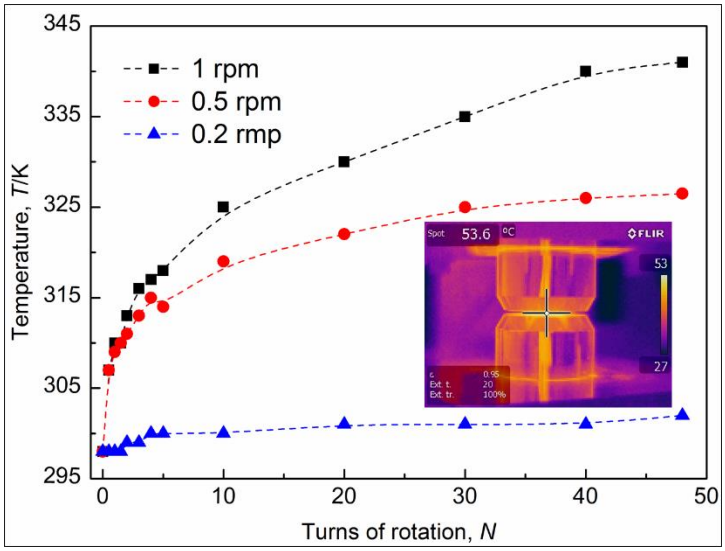

Fig. 4.26. The temperature of the sample as a function of rotations of rotation. The inset is an example from the infrared camera representing the sample deformed by 50 rotations of HPT at 0.5 rpm.

4.5 Summary

Severe plastic deformation by HPT induced drastic grain refinement and solid-state amorphization in Zr-40at%Cu-10at%Al alloy. After 100 turns of HPT, the sample was mostly amorphous with embedded nano-size particles of τ_5 phase. Compared to cast $Zr_{50}Cu_{40}Al_{10}$ metallic glass, this HPT-amorphized sample exhibited a homogeneous plastic flow during nanoindentation and a higher relaxation enthalpy and lower Vickers microhardness than that in MG. The observed difference in the mechanical and thermal properties could be attributed to the structural rejuvenation occurred concurrently with solid-state amorphization during HPT deformation.

High-pressure torsion was also performed on the same crystalline alloy to study the influence of rotation speed on solid-state amorphization (SSA). It was found that the volume fraction of the amorphous phase increased with the rotation speed. Discussed from the perspective of the generalized Lindemann melting criterion, it is inferred that the higher anvil speed led to the introduction of more crystalline defects in the sample as a whole and thus to the increased volume where the defect density reached critical value for defect-induced melting.

Chapter 5 Conclusions

This thesis studies the mechanically-induced structural rejuvenation in Zr-Cu-Al-based amorphous alloys with the main effort devoted to answering the following questions: 1) what kind of amorphous alloys are more susceptible to rejuvenation; and 2) are the amorphous phases made by solid-state amorphization and melt quenching different?

For the first part, $Zr_{55}Cu_{30}Ni_5Al_{10}$ (eutectic) and $Zr_{65}Cu_{18}Ni_7Al_{10}$ (hypoeutectic) metallic glasses (MGs) were subjected to various rotations of high-pressure torsion (HPT). It was found that the relaxation enthalpy increased with increasing rotation numbers, indicating pronounced structural rejuvenation. The rejuvenation was also accompanied by a reduction of the elastic modulus and nanohardness (*i.e.* strain softening), and a transition of the deformation mode to less localized plastic flow without any observable shear band around the nanoindentation indent. The thermal stability was also deteriorated especially for the hypoeutectic MG. Discussed from the perspectives of short-range order and liquid fragility, it was suggested that a more fragile liquid tends to experience a more drastic ordering process during the liquid-to-glass transition, which is possibly related to the larger increase of the relatively ordered SROs. These ordered SROs will be partially destroyed during HPT, resulting in a more disordered structure (*i.e*. rejuvenation). Therefore, an MG formed from a more fragile liquid could experience a more drastic disordering process during HPT, making it more susceptible to mechanically induced rejuvenation.

For the second part, a crystalline Zr-40at%Cu-10at%Al alloy was deformed by HPT, which induced significant grain-refinement following by solid-state amorphization (SSA). After 100 rotations of HPT, the end material has a composite structure, in which the τ_5 particles in the size of tens of nm were embedded in the amorphous matrix. Compared with the $Zr_{50}Cu_{40}Al_{10}$ MG made by melt quenching, the sample obtained from 100 rotations of HPT exhibited a much larger relaxation enthalpy, a lower nanoindentation hardness and elastic modulus, as well as homogenous plastic deformation without any discernible shear band around the indent. Furthermore, the hardness, elastic modulus and localized plastic deformation with obvious shear banding in the HPT-amorphized sample can be restored by sub or near T_g (T_g: glass transition temperature) annealing. These results indicate that the HPT-amorphized sample possesses extensively rejuvenated structure, indicating the amorphous phase obtained from solid-state amorphization could be more disordered than the one made by melt quenching.

Revisiting the potential energy landscape presented in Fig. 1.12, it seems clear that for the Zr-Cu-Al alloys, severe plastic deformation by HPT can drastically increase their energy levels regardless of the state of the starting material (whether it be amorphous or crystalline). Roughly speaking, both cases (schematically the black and red arrows in Fig. 1.12) can be regarded as rejuvenation as there is an unquestionable increase in the relaxation enthalpy, despite the very different underlying mechanisms. As a very recent study suggests [17], the decrease of shear modulus (a well-expected phenomenon after rejuvenation of an MG) can be mainly attributed to the increase of vibrational mean square displacement ($<\mu^2_{vib}>$ in chapter 4, termed as $<r^2>$ in ref. [17]). Whereas the SSA is primarily caused by the increase of the static mean square displacement. On the other hand, the end materials fabricated by different rejuvenation paths may not be essentially the same. With the limited reference available at hand [135], it can only be speculated that the short as well as the medium range orders of the amorphous phase made by solid-state amorphization are both more disordered than the ones of the melt-quenched amorphous phase. A better understanding of this issue may be facilitated by more experimental and simulation results of the solid-state amorphized sample without any residual crystals.

Reference

[1] P.G. Debenedetti, F.H. Stillinger, *Supercooled liquids and the glass transition*, Nature 410 (2001).

[2] T. Nagase, A. Sasaki, H.Y. Yasuda, H. Mori, T. Terai, T. Kakeshita, *Stability of B2 phase in Ti–Ni–Fe alloys against MeV electron-irradiation-induced solid-state amorphization and martensite transformation*, Intermetallics 19 (2011).

[3] Y.-L. Chen, C.-W. Tsai, C.-C. Juan, M.-H. Chuang, J.-W. Yeh, T.-S. Chin, S.-K. Chen, *Amorphization of equimolar alloys with HCP elements during mechanical alloying*, J. Alloys Compd. 506 (2010).

[4] H.W. Sheng, K. Lu, E. Ma, *Amorphization of Zr–Al solid solutions under mechanical alloying at different temperatures*, J. Appl. Phys. 85 (1999).

[5] J. Koike, D. Parkin, M. Nastasi, *Crystal-to-amorphous transformation of NiTi induced by cold rolling*, J. Mater. Res. 5 (1990).

[6] G.P. Dinda, H. Rösner, G. Wilde, *Cold-rolling induced amorphization in Cu–Zr, Cu–Ti–Zr and Cu–Ti–Zr–Ni multilayers*, J. Non-Cryst. Solids 353 (2007).

[7] F.Q. Meng, K. Tsuchiya, Y. Yokoyama, *Crystalline to amorphous transformation in Zr–Cu–Al alloys induced by high pressure torsion*, Intermetallics 37 (2013).

[8] Á. Révész, S. Hóbor, J.L. Lábár, A.P. Zhilyaev, Z. Kovács, *Partial amorphization of a Cu–Zr–Ti alloy by high pressure torsion*, J. Appl. Phys. 100 (2006).

[9] J. Huang, Y. Zhu, X. Liao, R. Valiev, *Amorphization of TiNi induced by high-pressure torsion*, Philos. Mag. Lett. 84 (2004).

[10] J. Qiang, D. Estevez, Y. Dong, Q. Man, C. Chang, X. Wang, R.-W. Li, *Giant magnetoimpedance effect enhanced by thermoplastic drawing*, J. Appl. Phys. 116 (2014).

[11] J. Qiang, D. Estevez, C. Chang, Q. Man, R.-W. Li, X. Wang, A. Inoue, *High strength CoFe-based glassy alloy with high thermal stability*, Mater. Lett. 114 (2014).

[12] A.L. Greer, Y.Q. Cheng, E. Ma, *Shear bands in metallic glasses*, Materials Science and Engineering: R: Reports 74 (2013).

[13] D. Turnbull, M.H. Cohen, *Free‐Volume Model of the Amorphous Phase: Glass Transition*, The Journal of Chemical Physics 34 (1961).

[14] Y. Cheng, E. Ma, *Atomic-level structure and structure–property relationship in metallic glasses*, Prog. Mater. Sci. 56 (2011).

[15] F. Spaepen, *A microscopic mechanism for steady state inhomogeneous flow in metallic glasses*, Acta metallurgica 25 (1977).

[16] Y.J. Huang, J. Shen, J.F. Sun, *Bulk metallic glasses: Smaller is softer*, Appl. Phys. Lett. 90 (2007).

[17] J. Ding, Y.-Q. Cheng, H. Sheng, M. Asta, R.O. Ritchie, E. Ma, *Universal structural parameter to quantitatively predict metallic glass properties*, Nat. Commun. 7 (2016).

[18] E. Ma, *Tuning order in disorder*, Nat. Mater. 14 (2015).

[19] Y.Q. Cheng, A.J. Cao, E. Ma, *Correlation between the elastic modulus and the intrinsic plastic behavior of metallic glasses: The roles of atomic configuration and alloy composition*, Acta Mater. 57 (2009).

[20] J. Ding, Y. Cheng, E. Ma, *Charge-transfer-enhanced prism-type local order in amorphous $Mg_{65}Cu_{25}Y_{10}$: Short-to-medium-range structural evolution underlying liquid fragility and heat capacity*, Acta Mater. 61 (2013).

[21] Y. Ritter, K. Albe, *Chemical and topological order in shear bands of $Cu_{64}Zr_{36}$ and $Cu_{36}Zr_{64}$ glasses*, J. Appl. Phys. 111 (2012).

[22] H.Z. Fang, X. Hui, G.L. Chen, Z.K. Liu, *Al-centered icosahedral ordering in $Cu_{46}Zr_{46}Al_8$ bulk metallic glass*, Appl. Phys. Lett. 94 (2009).

[23] Y. Fan, T. Iwashita, T. Egami, *Energy landscape-driven non-equilibrium evolution of inherent structure in disordered material*, Nat. Commun. 8 (2017).

[24] H.B. Yu, W.H. Wang, H.Y. Bai, Y. Wu, M.W. Chen, *Relating activation of shear transformation zones to β relaxations in metallic glasses*, Phys. Rev. B 81 (2010).

[25] H.S. Chen, E. Coleman, *Structure relaxation spectrum of metallic glasses*, Appl. Phys. Lett. 28 (1976).

[26] Q. Wang, S.T. Zhang, Y. Yang, Y.D. Dong, C.T. Liu, J. Lu, *Unusual fast secondary relaxation in metallic glass*, Nat. Commun. 6 (2015).

[27] Y. Liu, T. Fujita, D. Aji, M. Matsuura, M. Chen, *Structural origins of Johari-Goldstein relaxation in a metallic glass*, Nat. Commun. 5 (2014).

[28] H.B. Yu, K. Samwer, W.H. Wang, H.Y. Bai, *Chemical influence on β-relaxations and the formation of molecule-like metallic glasses*, Nat. Commun. 4 (2013).

[29] W.H. Wang, Y. Yang, T.G. Nieh, C.T. Liu, *On the source of plastic flow in metallic glasses: Concepts and models*, Intermetallics 67 (2015).

[30] A. Slipenyuk, J. Eckert, *Correlation between enthalpy change and free volume reduction during structural relaxation of $Zr_{55}Cu_{30}Al_{10}Ni_5$ metallic glass*, Scripta Mater. 50 (2004).

[31] M. Kohda, O. Haruyama, T. Ohkubo, T. Egami, *Kinetics of volume and enthalpy relaxation in $Pt_{60}Ni_{15}P_{25}$ bulk metallic glass*, Phys. Rev. B 81 (2010).

[32] A. Kahl, T. Koeppe, D. Bedorf, R. Richert, M.L. Lind, M.D. Demetriou, W.L. Johnson, W. Arnold, K. Samwer, *Dynamical and quasistatic structural relaxation paths in $Pd_{40}Ni_{40}P_{20}$ glass*, Appl. Phys. Lett. 95 (2009).

[33] J. Saida, R. Yamada, M. Wakeda, *Recovery of less relaxed state in Zr-Al-Ni-Cu bulk metallic glass annealed above glass transition temperature*, Appl. Phys. Lett. 103 (2013).

[34] M. Wakeda, J. Saida, J. Li, S. Ogata, *Controlled rejuvenation of amorphous metals with thermal processing*, Sci. Rep. 5 (2015).

[35] S.V. Ketov, Y.H. Sun, S. Nachum, Z. Lu, A. Checchi, A.R. Beraldin, H.Y. Bai, W.H. Wang, D.V. Louzguine-Luzgin, M.A. Carpenter, A.L. Greer, *Rejuvenation of metallic glasses by non-affine thermal strain*, Nature 524 (2015).

[36] A. Greer, Y. Sun, *Stored energy in metallic glasses due to strains within the elastic limit*, Philos. Mag. 96 (2016).

[37] F. Meng, K. Tsuchiya, S. II, Y. Yokoyama, *Reversible transition of deformation mode by structural rejuvenation and relaxation in bulk metallic glass*, Appl. Phys. Lett. 101 (2012).

[38] W. Dmowski, Y. Yokoyama, A. Chuang, Y. Ren, M. Umemoto, K. Tsuchiya, A. Inoue, T. Egami, *Structural rejuvenation in a bulk metallic glass induced by severe plastic deformation*, Acta Mater. 58 (2010).

[39] W. Klement, R.H. Willens, P.O.L. Duwez, *Non-crystalline Structure in Solidified Gold-Silicon Alloys*, Nature 187 (1960).

[40] A. Inoue, A. Takeuchi, *Recent development and application products of bulk glassy alloys*, Acta Mater. 59 (2011).

[41] T. Yamasaki, M. Yamada, T. Mori, T. Kikuchi, Y. Yoshihiko, A. Inoue, D.H. Kim, *Viscous Flow Behaviour of Supercooled Liquids and Mechanical Properties in Zr-Cu-Ni-Al Bulk Metallic Glasses*, Mater. Sci. Forum 654 (2010).

[42] Y. Yokoyama, H. Inoue, K. Fukaura, A. Inoue, *Relationship between the liquidus surface and structures of Zr-Cu-Al bulk amorphous alloys*, Mater. Trans. 43 (2002).

[43] A. Inoue, *Stabilization of metallic supercooled liquid and bulk amorphous alloys*, Acta Mater. 48 (2000).

[44] G. Firstov, J. Van Humbeeck, Y.N. Koval, *Peculiarities of the martensitic transformation in ZrCu intermetallic compound-potential high temperature SMA*, Le Journal de Physique IV 11 (2001).

[45] J.W. Seo, D. Schryvers, *TEM investigation of the microstructure and defects of CuZr martensite. Part I: Morphology and twin systems*, Acta Mater. 46 (1998).

[46] R.Z. Valiev, A.K. Mukherjee, *Nanostructures and unique properties in intermetallics, subjected to severe plastic*

deformation, Scripta Mater. 44 (2001).

[47] Y.F. Sun, T. Nakamura, Y. Todaka, M. Umemoto, N. Tsuji, *Fabrication of CuZr(Al) bulk metallic glasses by high pressure torsion*, Intermetallics 17 (2009).

[48] Y. Yokoyama, K. Fukaura, A. Inoue, *Cast structure and mechanical properties of Zr–Cu–Ni–Al bulk glassy alloys*, Intermetallics 10 (2002).

[49] P.W. Bridgman, *Effects of high shearing stress combined with high hydrostatic pressure*, Phys. Rev. 48 (1935).

[50] P.W. Bridgman, *On Torsion Combined with Compression*, J. Appl. Phys. 14 (1943).

[51] R. Valiev, O. Kuznetsov, R.S. Musalimov, N. Tsenev, *Low-temperature superplasticity of metallic materials*, SPhD 33 (1988).

[52] K. Edalati, Z. Horita, *A review on high-pressure torsion (HPT) from 1935 to 1988*, Mater. Sci. Eng., A 652 (2016).

[53] K.-J. Dunn, *The yield stress of opposed anvils*, J. Appl. Phys. 48 (1977).

[54] A. Zhilyaev, T. McNelley, T. Langdon, *Evolution of microstructure and microtexture in fcc metals during high-pressure torsion*, J. Mater. Sci. 42 (2007).

[55] A.P. Zhilyaev, G.V. Nurislamova, B.K. Kim, M.D. Baró, J.A. Szpunar, T.G. Langdon, *Experimental parameters influencing grain refinement and microstructural evolution during high-pressure torsion*, Acta Mater. 51 (2003).

[56] M.V. Degtyarev, T.I. Chashchukhina, L.M. Voronova, A.M. Patselov, V.P. Pilyugin, *Influence of the relaxation processes on the structure formation in pure metals and alloys under high-pressure torsion*, Acta Mater. 55 (2007).

[57] P.W. Bridgman, *The resistance of 72 elements, alloys and compounds to 100,000 Kg/Cm ²*, Proc. Am. Acad. Arts Sci. 81 (1952).

[58] V.G. Pushin, V.V. Stolyarov, R.Z. Valiev, T.C. Lowe, Y.T. Zhu, *Nanostructured TiNi-based shape memory alloys processed by severe plastic deformation*, Mater. Sci. Eng., A 410–411 (2005).

[59] A.V. Korznikov, O. Dimitrov, G.F. Korznikova, J.P. Dallas, A. Quivy, R.Z. Valiev, A. Mukherjee, *Nanocrystalline structure and phase transformation of the intermetallic compound TiAl processed by severe plastic deformation*, Nanostruct. Mater. 11 (1999).

[60] A.P. Zhilyaev, T.G. Langdon, *Using high-pressure torsion for metal processing: Fundamentals and applications*, Prog. Mater. Sci. 53 (2008).

[61] N. Boucharat, R. Hebert, H. Rösner, R. Valiev, G. Wilde, *Nanocrystallization of amorphous $Al_{88}Y_7Fe_5$ alloy induced by plastic deformation*, Scripta Mater. 53 (2005).

[62] Z. Kovács, P. Henits, A.P. Zhilyaev, Á. Révész, *Deformation induced primary crystallization in a thermally non-primary crystallizing amorphous $Al_{85}Ce_8Ni_5Co_2$ alloy*, Scripta Mater. 54 (2006).

[63] D.-H. Lee, I.-C. Choi, M.-Y. Seok, J. He, Z. Lu, J.-Y. Suh, M. Kawasaki, T.G. Langdon, J.-i. Jang, *Nanomechanical behavior and structural stability of a nanocrystalline CoCrFeNiMn high-entropy alloy processed by high-pressure torsion*, J. Mater. Res. 30 (2015).

[64] B. Schuh, F. Mendez-Martin, B. Völker, E.P. George, H. Clemens, R. Pippan, A. Hohenwarter, *Mechanical properties, microstructure and thermal stability of a nanocrystalline CoCrFeMnNi high-entropy alloy after severe plastic deformation*, Acta Mater. 96 (2015).

[65] Q.H. Tang, Y. Huang, Y.Y. Huang, X.Z. Liao, T.G. Langdon, P.Q. Dai, *Hardening of an $Al_{0.3}$CoCrFeNi high entropy alloy via high-pressure torsion and thermal annealing*, Mater. Lett. 151 (2015).

[66] H. Yuan, M.-H. Tsai, G. Sha, F. Liu, Z. Horita, Y. Zhu, J.T. Wang, *Atomic-scale homogenization in an fcc-based high-entropy alloy via severe plastic deformation*, J. Alloys Compd. 686 (2016).

[67] H. Shahmir, J. He, Z. Lu, M. Kawasaki, T.G. Langdon, *Effect of annealing on mechanical properties of a nanocrystalline CoCrFeNiMn high-entropy alloy processed by high-pressure torsion*, Mater. Sci. Eng., A 676 (2016).

[68] A.P. Zhilyaev, B.K. Kim, G.V. Nurislamova, M.D. Baró, J.A. Szpunar, T.G. Langdon, *Orientation imaging*

microscopy of ultrafine-grained nickel, Scripta Mater. 46 (2002).

[69] J. Dutkiewicz, J. Kuśnierz, W. Maziarz, M. Lejkowska, H. Garbacz, M. Lewandowska, A.V. Dobromyslov, K.J. Kurzydłowski, *Microstructure and mechanical properties of nanocrystalline titanium and Ti–Ta–Nb alloy manufactured using various deformation methods*, physica status solidi (a) 202 (2005).

[70] Y. Todaka, M. Umemoto, J. Yin, Z. Liu, K. Tsuchiya, *Role of strain gradient on grain refinement by severe plastic deformation*, Mater. Sci. Eng., A 462 (2007).

[71] Y. Harai, Y. Ito, Z. Horita, *High-pressure torsion using ring specimens*, Scripta Mater. 58 (2008).

[72] O. Ciuca, *Process of disordering and grain refinement in Ni_3Al by high-pressure torsion*, Toyohashi University of Technology Doctor of engineering (2010)

[73] E. Freire, *Differential scanning calorimetry*, Protein Stability and Folding: Theory and Practice (1995).

[74] G. Pharr, W. Oliver, F. Brotzen, *On the generality of the relationship among contact stiffness, contact area, and elastic modulus during indentation*, J. Mater. Res. 7 (1992).

[75] P. Yiu, J.S.C. Jang, S.Y. Chang, Y.C. Chen, J.P. Chu, C.H. Hsueh, *Plasticity enhancement of Zr-based bulk metallic glasses by direct current electropulsing*, J. Alloys Compd. 525 (2012).

[76] A.S. Argon, *Plastic deformation in metallic glasses*, Acta Metallurgica 27 (1979).

[77] M. Falk, J. Langer, *Dynamics of viscoplastic deformation in amorphous solids*, Physical Review E 57 (1998).

[78] Y. Sun, A. Concustell, A.L. Greer, *Thermomechanical processing of metallic glasses: extending the range of the glassy state*, Nat. Rev. Mater. (2016).

[79] D.V. Louzguine-Luzgin, V.Y. Zadorozhnyy, S.V. Ketov, Z. Wang, A.A. Tsarkov, A.L. Greer, *On room-temperature quasi-elastic mechanical behaviour of bulk metallic glasses*, Acta Mater. 129 (2017).

[80] J. Saida, R. Yamada, M. Wakeda, S. Ogata, *Thermal rejuvenation in metallic glasses*, Sci. Technol. Adv. Mater. 18 (2017).

[81] N. Adachi, Y. Todaka, Y. Yokoyama, M. Umemoto, *Improving the mechanical properties of Zr-based bulk metallic glass by controlling the activation energy for β-relaxation through plastic deformation*, Appl. Phys. Lett. 105 (2014).

[82] K.-W. Park, C.-M. Lee, M. Wakeda, Y. Shibutani, M.L. Falk, J.-C. Lee, *Elastostatically induced structural disordering in amorphous alloys*, Acta Mater. 56 (2008).

[83] O. Haruyama, K. Kisara, A. Yamashita, K. Kogure, Y. Yokoyama, K. Sugiyama, *Characterization of free volume in cold-rolled $Zr_{55}Cu_{30}Ni_5Al_{10}$ bulk metallic glasses*, Acta Mater. 61 (2013).

[84] Y.H. Sun, A. Concustell, M.A. Carpenter, J.C. Qiao, A.W. Rayment, A.L. Greer, *Flow-induced elastic anisotropy of metallic glasses*, Acta Mater. 112 (2016).

[85] V.A. Khonik, G.V. Afonin, A.Y. Vinogradov, A.N. Tsyplakov, S.V. Tyutin, *Crossover and normal structural relaxation in naturally aged glassy $Pd_{40}Cu_{30}Ni_{10}P_{20}$*, Intermetallics 74 (2016).

[86] Y. Wei, G. Xu, K. Zhang, Z. Yang, Y. Guo, C. Huang, B. Wei, *Anomalous shear band characteristics and extra-deep shock-affected zone in Zr-based bulk metallic glass treated with nanosecond laser peening*, Sci. Rep. 7 (2017).

[87] Y.M. Lu, J.F. Zeng, J.C. Huang, S.Y. Kuan, T.G. Nieh, W.H. Wang, M.X. Pan, C.T. Liu, Y. Yang, *In-situ atomic force microscopy observation revealing gel-like plasticity on a metallic glass surface*, J. Appl. Phys. 121 (2017).

[88] F. Meng, K. Tsuchiya, Y. Yokoyama, *Pronounced Structural Rejuvenation in $Zr_{50}Cu_{40}Al_{10}$ Metallic Glass Strained by Torsional Straining at Elevated Temperature*, Mater. Trans. 55 (2014).

[89] M.D. Ediger, *Spatially heterogeneous dynamics in supercooled liquids*, Annual Review of Physical Chemistry 51 (2000).

[90] X.D. Wang, Q.P. Cao, J.Z. Jiang, H. Franz, J. Schroers, R.Z. Valiev, Y. Ivanisenko, H. Gleiter, H.J. Fecht, *Atomic-level structural modifications induced by severe plastic shear deformation in bulk metallic glasses*, Scripta Mater. 64 (2011).

[91] Y. Masahiro, K. Ryo, Y. Tohru, A. Hiroki, T. Koichi, Y. Yoshihiko, *Nanocrystallization of Zr-Cu-Ni-Al-Au glassy alloys during severe plastic deformation*, IOP Conf. Ser.: Mater. Sci. Eng. 63 (2014).

[92] N. Mitrovic, S. Roth, J. Eckert, *Kinetics of the glass-transition and crystallization process of* $Fe_{72-x}Nb_xAl_5Ga_2P_{11}C_6B_4(x=0,2)$ *metallic glasses*, Appl. Phys. Lett. 78 (2001).

[93] Y.-L. Gao, J. Shen, J.-F. Sun, G. Wang, D.-W. Xing, H.-Z. Xian, B.-D. Zhou, *Crystallization behavior of ZrAlNiCu bulk metallic glass with wide supercooled liquid region*, Mater. Lett. 57 (2003).

[94] A. Takeuchi, A. Inoue, *Classification of bulk metallic glasses by atomic size difference, heat of mixing and period of constituent elements and its application to characterization of the main alloying element*, Mater. Trans. 46 (2005).

[95] M. Guerdane, H. Teichler, *Structure of the amorphous, massive-metallic-glass forming* $Ni_{25}Zr_{60}Al_{15}$ *alloy from molecular dynamics simulations*, Phys. Rev. B 65 (2001).

[96] Y.P. Mitrofanov, M. Peterlechner, I. Binkowski, M.Y. Zadorozhnyy, I.S. Golovin, S.V. Divinski, G. Wilde, *The impact of elastic and plastic strain on relaxation and crystallization of Pd–Ni–P-based bulk metallic glasses*, Acta Mater. 90 (2015).

[97] B. Yang, T.G. Nieh, *Effect of the nanoindentation rate on the shear band formation in an Au-based bulk metallic glass*, Acta Mater. 55 (2007).

[98] C.A. Schuh, T.G. Nieh, *A nanoindentation study of serrated flow in bulk metallic glasses*, Acta Mater. 51 (2003).

[99] H. Xie, Y. Li, D. Yang, P. Hodgson, C.e. Wen, *Plastic deformation in the annealed Zr41Ti14Cu12.5Ni10Be22.5 bulk metal glass under indenter*, J. Alloys Compd. 475 (2009).

[100] Y. Yokoyama, K. Fujita, A.R. Yavari, A. Inoue, *Malleable hypoeutectic Zr–Ni–Cu–Al bulk glassy alloys with tensile plastic elongation at room temperature*, Philos. Mag. Lett. 89 (2009).

[101] Y. Huang, Y.L. Chiu, J. Shen, Y. Sun, J.J.J. Chen, *Mechanical performance of metallic glasses during nanoscratch tests*, Intermetallics 18 (2010).

[102] Z.F. Zhang, J. Eckert, L. Schultz, *Difference in compressive and tensile fracture mechanisms of* $Zr_{59}Cu_{20}Al_{10}Ni_8Ti_3$ *bulk metallic glass*, Acta Mater. 51 (2003).

[103] F. Shimizu, S. Ogata, J. Li, *Yield point of metallic glass*, Acta Mater. 54 (2006).

[104] M. Wakeda, Y. Shibutani, S. Ogata, J. Park, *Relationship between local geometrical factors and mechanical properties for Cu–Zr amorphous alloys*, Intermetallics 15 (2007).

[105] F. Delogu, *Identification and characterization of potential shear transformation zones in metallic glasses*, Phys. Rev. Lett. 100 (2008).

[106] D. Srolovitz, V. Vitek, T. Egami, *An atomistic study of deformation of amorphous metals*, Acta Metallurgica 31 (1983).

[107] Y.B. Wang, D.D. Qu, X.H. Wang, Y. Cao, X.Z. Liao, M. Kawasaki, S.P. Ringer, Z.W. Shan, T.G. Langdon, J. Shen, *Introducing a strain-hardening capability to improve the ductility of bulk metallic glasses via severe plastic deformation*, Acta Mater. 60 (2012).

[108] Á. Révész, P. Henits, Z. Kovács, *Structural changes in Zr-based bulk metallic glasses deformed by high pressure torsion*, J. Alloys Compd. 495 (2010).

[109] Q. Qin, G.B. McKenna, *Correlation between dynamic fragility and glass transition temperature for different classes of glass forming liquids*, J. Non-Cryst. Solids 352 (2006).

[110] J. Ding, Y.-Q. Cheng, H. Sheng, E. Ma, *Short-range structural signature of excess specific heat and fragility of metallic-glass-forming supercooled liquids*, Phys. Rev. B 85 (2012).

[111] A.J. Cao, Y.Q. Cheng, E. Ma, *Structural processes that initiate shear localization in metallic glass*, Acta Mater. 57 (2009).

[112] Y.Q. Cheng, H.W. Sheng, E. Ma, *Relationship between structure, dynamics, and mechanical properties in metallic*

glass-forming alloys, Phys. Rev. B 78 (2008).

[113] Y.Q. Cheng, E. Ma, H.W. Sheng, *Atomic Level Structure in Multicomponent Bulk Metallic Glass*, Phys. Rev. Lett. 102 (2009).

[114] N.A. Mauro, M. Blodgett, M.L. Johnson, A.J. Vogt, K.F. Kelton, *A structural signature of liquid fragility*, Nat. Commun. 5 (2014).

[115] G. Adam, J.H. Gibbs, *On the Temperature Dependence of Cooperative Relaxation Properties in Glass‐Forming Liquids*, The Journal of Chemical Physics 43 (1965).

[116] O. Gross, B. Bochtler, M. Stolpe, S. Hechler, W. Hembree, R. Busch, I. Gallino, *The kinetic fragility of Pt-P- and Ni-P-based bulk glass-forming liquids and its thermodynamic and structural signature*, Acta Mater. 132 (2017).

[117] Q. Man, A. Inoue, Y. Dong, J. Qiang, C. Zhao, B. Shen, *A new CoFe-based bulk metallic glasses with high thermoplastic forming ability*, Scripta Mater. 69 (2013).

[118] S. Wei, M. Stolpe, O. Gross, W. Hembree, S. Hechler, J. Bednarcik, R. Busch, P. Lucas, *Structural evolution on medium-range-order during the fragile-strong transition in* $Ge_{15}Te_{85}$, Acta Mater. 129 (2017).

[119] W.H. Wang, *Correlations between elastic moduli and properties in bulk metallic glasses*, J. Appl. Phys. 99 (2006).

[120] J.W. Liu, Q.P. Cao, L.Y. Chen, X.D. Wang, J.Z. Jiang, *Shear band evolution and hardness change in cold-rolled bulk metallic glasses*, Acta Mater. 58 (2010).

[121] H.S. Chen, *Stored energy in a cold-rolled metallic glass*, Appl. Phys. Lett. 29 (1976).

[122] D.N. Perera, *Compilation of the fragility parameters for several glass-forming metallic alloys*, J. Phys.: Condens. Matter 11 (1999).

[123] H. Tanaka, *Relationship among glass-forming ability, fragility, and short-range bond ordering of liquids*, J. Non-Cryst. Solids 351 (2005).

[124] N. Jakse, A. Pasturel, *Local order and dynamic properties of liquid and undercooled* Cu_xZr_{1-x} *alloys by ab initio molecular dynamics*, Phys. Rev. B 78 (2008).

[125] R. Schwarz, W. Johnson, *Formation of an amorphous alloy by solid-state reaction of the pure polycrystalline metals*, Phys. Rev. Lett. 51 (1983).

[126] D.E. Luzzi, H. Mori, H. Fujita, M. Meshii, *A crystalline-amorphous transition in CuTi induced by high energy electron irradiation*, Scripta Metallurgica 18 (1984).

[127] P.R. Okamoto, N.Q. Lam, L.E. Rehn, *Physics of Crystal-to-Glass Transformations*, Solid State Phys. Volume 52 (1999).

[128] R.B. Schwarz, R.R. Petrich, C.K. Saw, *The synthesis of amorphous Ni-Ti alloy powders by mechanical alloying*, J. Non-Cryst. Solids 76 (1985).

[129] B.B. Straumal, A.R. Kilmametov, A.A. Mazilkin, S.G. Protasova, K.I. Kolesnikova, P.B. Straumal, B. Baretzky, *Amorphization of Nd–Fe–B alloy under the action of high-pressure torsion*, Mater. Lett. 145 (2015).

[130] R.V. Sundeev, A.M. Glezer, A.V. Shalimova, *Are the abilities of crystalline alloys to amorphization upon melt quenching and severe plastic deformation identical or different?*, Mater. Lett. 175 (2016).

[131] V.V. Stolyarov, D.V. Gunderov, A.G. Popov, V.S. Gaviko, A.S. Ermolenko, *Structure evolution and changes in magnetic properties of severe plastic deformed Nd(Pr)–Fe–B alloys during annealing*, J. Alloys Compd. 281 (1998).

[132] R.V. Sundeev, A.V. Shalimova, A.M. Glezer, E.A. Pechina, M.V. Gorshenkov, G.I. Nosova, *In situ observation of the "crystalline⇒amorphous state" phase transformation in* Ti_2NiCu *upon high-pressure torsion*, Mater. Sci. Eng., A 679 (2017).

[133] R.V. Sundeev, A.M. Glezer, A.V. Shalimova, *Crystalline to amorphous transition in solids upon high-pressure torsion*, J. Alloys Compd. 611 (2014).

[134] P.J. Hsieh, Y.P. Hung, J.C. Huang, *Transformation into nanocrystalline or amorphous materials in Zr–X binary*

systems using ARB route, Scripta Mater. 49 (2003).

[135] M.H. Yang, J.H. Li, B.X. Liu, *Proposed correlation of structure network inherited from producing techniques and deformation behavior for Ni-Ti-Mo metallic glasses via atomistic simulations*, Sci. Rep. 6 (2016).

[136] Y. Chen, M. Bibole, R. Le Hazif, G. Martin, *Ball-milling-induced amorphization in Ni_xZr_y compounds: A parametric study*, Phys. Rev. B 48 (1993).

[137] J.H. Han, N. Mattern, B. Schwarz, S. Gorantla, T. Gemming, J. Eckert, *Microstructure and magnetic properties of Gd–Hf–Co–Al phase separated metallic glasses*, Intermetallics 20 (2012).

[138] J.I. Lee, J.W. Kim, H.S. Oh, J.S. Park, E.S. Park, *Abnormal devitrification behavior and mechanical response of cold-rolled Mg-rich Mg-Cu-Gd metallic glasses*, Acta Mater. 116 (2016).

[139] X. Bian, G. Wang, K. Chan, J. Ren, Y. Gao, Q. Zhai, *Shear avalanches in metallic glasses under nanoindentation: Deformation units and rate dependent strain burst cut-off*, Appl. Phys. Lett. 103 (2013).

[140] H.J. Fecht, *Defect-induced melting and solid-state amorphization*, Nature 356 (1992).

[141] N. Adachi, Y. Todaka, Y. Yokoyama, M. Umemoto, *Cause of hardening and softening in the bulk glassy alloy $Zr_{50}Cu_{40}Al_{10}$ after high-pressure torsion*, Mater. Sci. Eng., A 627 (2015).

[142] K. Lu, W.D. Wei, J.T. Wang, *Grain growth kinetics and interfacial energies in nanocrystalline Ni‐P alloys*, J. Appl. Phys. 69 (1991).

[143] T. Hentschel, D. Isheim, R. Kirchheim, F. Müller, H. Kreye, *Nanocrystalline Ni–3.6 at.% P and its transformation sequence studied by atom-probe field-ion microscopy*, Acta Mater. 48 (2000).

[144] J.F. Löffler, W.L. Johnson, *Model for decomposition and nanocrystallization of deeply undercooled $Zr_{41.2}Ti_{13.8}Cu_{12.5}Ni_{10}Be_{22.5}$*, Appl. Phys. Lett. 76 (2000).

[145] Y.F. Sun, H. Fujii, T. Nakamura, N. Tsuji, D. Todaka, M. Umemoto, *Critical strain for mechanical alloying of Cu–Ag, Cu–Ni and Cu–Zr by high-pressure torsion*, Scripta Mater. 65 (2011).

[146] F.Q. Meng, K. Tsuchiya, Q. Mei, B. Jiang, Y. Yokoyama, *Anomalous Temperature Dependence of Crystalline-to-Amorphous Transformation Induced by High-Pressure Torsion in $Zr_{50}(Cu, Al)_{50}$*, Mater. Trans. 54 (2013).

[147] S.D. Prokoshkin, I.Y. Khmelevskaya, S.V. Dobatkin, I.B. Trubitsyna, E.V. Tatyanin, V.V. Stolyarov, E.A. Prokofiev, *Alloy composition, deformation temperature, pressure and post-deformation annealing effects in severely deformed Ti–Ni based shape memory alloys*, Acta Mater. 53 (2005).

[148] H.B. Yu, R. Richert, R. Maaß, K. Samwer, *Unified Criterion for Temperature-Induced and Strain-Driven Glass Transitions in Metallic Glass*, Phys. Rev. Lett. 115 (2015).

[149] F. Roters, D. Raabe, G. Gottstein, *Work hardening in heterogeneous alloys—a microstructural approach based on three internal state variables*, Acta Mater. 48 (2000).

[150] A.M. Cuitiño, M. Ortiz, *Ductile fracture by vacancy condensation in f.c.c. single crystals*, Acta Mater. 44 (1996).

[151] P.H.R. Pereira, R.B. Figueiredo, Y. Huang, P.R. Cetlin, T.G. Langdon, *Modeling the temperature rise in high-pressure torsion*, Mater. Sci. Eng., A 593 (2014).

[152] H. Shahmir, T.G. Langdon, *Characteristics of the allotropic phase transformation in titanium processed by high-pressure torsion using different rotation speeds*, Mater. Sci. Eng., A 667 (2016).

Acknowledgement

It seemed only yesterday that I just arrived in Japan and felt excited about everything. Now I am writing this note of thanks as the final touch of my thesis. It is amazing how time flies and it is already my turn to reflect on the old days.

First and foremost, my gratitude goes to my supervisor Professor Koichi Tsuchiya, without whom my research would be impossible. For the past three years, Professor Tsuchiya has guided me with wise counsel and patience. And his approachable personality has released a lot of pressure that came from the sometimes tedious research. Through it all, he has taught me the way to be a better researcher. And for this, I will always be grateful.

In addition, I would also like to extent my gratitude to every member of the examination board: Dr. Hisanori Tanimoto, Dr. Ikumu Watanabe and Dr. Masato Wakeda for their valuable instructions and advices.

A special thank you to Ms. Tomomi Utagawa. She always calls herself as our Japanese mother, indeed, she treats us students with nothing but kindness and thoughtfulness. With her help, I quickly adjusted myself to the new life.

Needless to say, I am indebted to every member of the former microstructure design group at NIMS, for teaching me how to use pieces of equipment and sharing their valuable experience. On top of that, I would also like to thank my friends in Tsukuba for their support and company, my life in Japan would be less interesting without them. This list goes on, and I couldn’t possibly thank those who have helped me enough.

Last but not least, I must thank my parents for their unwavering support and encouragement; they kept me going when no one else could.